

RADIATIVE TRANSFER AND PLANETARY MIGRATION IN  
PROTOPLANETARY DISKS

By

YASUHIRO HASEGAWA, B.Sc.

RADIATIVE TRANSFER AND PLANETARY  
MIGRATION IN PROTOPLANETARY DISKS

By

YASUHIRO HASEGAWA, B.Sc.

A Thesis

Submitted to the School of Graduate Studies

in Partial Fulfilment of the Requirements

for the Degree

Master of Science

McMaster University

©Copyright by Yasuhiro Hasegawa, September 2008

MASTER OF SCIENCE (2008)  
(Department of Physics and Astronomy)

McMaster University  
Hamilton, Ontario

TITLE: RADIATIVE TRANSFER AND PLANETARY MIGRATION IN  
PROTOPLANETARY DISKS

AUTHOR: Yasuhiro Hasegawa, B.Sc.

SUPERVISOR: Dr. Ralph E. Pudritz

NUMBER OF PAGES: xiv, 111

# Abstract

Planetary migration has become one of the most important processes in planet formation since the first discovery of an exoplanet around 51Peg. A decade after the discovery, the total number of exoplanets has increased to about three hundred. Theoretical work has shown that the disk configuration in which planets are formed strongly affects the subsequent migration of planets within them. Disks evolve and their shape transits from flared to flat. This is thought to arise because of dust settling. We take this effect into account in our models of planet migration in protoplanetary disks that are heated by the radiation of their central stars. In particular we solve the radiative transfer equation for disks by means of the Monte Carlo method, and then consider planetary migration. We focus on planets around very low mass stars (VLMSs).

Our calculations reproduce the disk configurations of Chiang & Goldreich (1997). As dust settles, the superheated and inner layer declines toward the mid-plane. At the same time, dust settling causes the temperature of the upper layer to increase and that of the inner layer to decrease. In order to calculate the migration time accurately, we include the gravity of planets, which causes the density around them to be compressed. This results in shadowing (in front of the planet) and illumination (behind the planet) regions. We included disk evolution by taking into account the effect of dust settling. We found that dust settling itself (without planetary gravity) can reduce the migration time by a factor of 8. When we included the gravity of planets, the effect of dust settling is somewhat washed out. This is because the effect of dust settling on

migration acts in a similar way to that of planetary gravity. Thus, when the migration time without dust settling is compared to the case of dust settling (including planetary gravity), dust settling can reduce the migration time by a factor of 2.

We also found that the migration time of massive planets ( $> 5M_{\oplus}$ ) in such low mass disks, for both cases, is comparable to the disk life time ( $\sim 10^7$  years). This suggests that planets around VLMS do not plunge into the star within a disk lifetime. This finding is consistent with the discovery of the super-Earth ( $\sim 5.5M_{\oplus}$ ) at 2.6 AU around M dwarf (Beaulieu et al., 2006). For lower mass planets, the migration time is about two orders of magnitude longer than the disk life time. Thus, the long planetary migration around VLMS does not cause any serious time mismatch problem as in the case of classical T Tauri star system.

# Acknowledgements

I would like to thank many people who have spent time with me and inspired me in various things. First, I would like to thank my supervisor, Dr. Ralph E Pudritz. His enthusiasm and passion for science have encouraged me to study harder, and inspired me to find and understand physics which is behind complicated problems. Without his help and advice, I could not have written this thesis. From his energetic, but patient attitude for science, I have learned something about being a good scientist.

I would also like to thank my committee members. Dr. Christine D. Wilson gave me some advice from different point of views. Dr. James Wadsley gave me some advice about the detail. Their advice has encouraged me to consider my thoughts again carefully and to study more.

I would like to thank Dr. Cornelis P Dullemond. He gave us his code called RADMC, and help me to understand it. Also discussion with him encouraged me to consider problems more physically. Also I would like to thank hospitality of the ITA of Heidelberg University where some of this research was completed.

I would also like to thank fellow graduate students and our department staff. I have enjoyed talking to them and appreciated their help. Special thanks go to Philippe Boisvert, Juan Madrid, Rob Cockcroft, Lindsay Oaster, Marc-Antoni Goulet, Dennis Duffin, and Dave Kirsh.

I would like to thank all member of the Japanese community. I could not imagine my life here without them. Special thanks go to Dr. Yukihiisa Nogami, Sumiko Nogami, Masamichi Ichikawa, Yoko Ichikawa, Issei Nakamura, Asako Nakamura, Tomoko Aharen, Hisako Omori, and Naohiro Yamanaka.

I would also like to thank my family for their constant support; My father, Kazuo Hasegawa, my mother, Kyoko Hasegawa, my father-in-law, Ikuo Hayashi, and my

mother-in-law, Tomoko Hayashi. Without their understanding and support, I could not live here and continue to study.

I would like to thank my undergrad supervisor, Dr. Akira Suzuki, who has introduced me to McMsater University. He has always given me good guidelines for my life.

Finally, I would like to express my eternal love to my wife, Kimiko, and my son, Yuya. Without you, I could not imagine my life. My every effort comes from my love to you.

*To my wife and son*

# Table of Contents

<b>Abstract</b>	iii
<b>Acknowledgements</b>	v
<b>List of Figures</b>	x
<b>List of Tables</b>	xiv
<b>Chapter 1 Introduction</b>	<b>1</b>
<b>Chapter 2 Planetary migration in gaseous disks</b>	<b>9</b>
2.1 Planetary migration . . . . .	10
2.1.1 Basic physics: Lindblad and corotation resonances & three types of migration . . . . .	10
2.1.2 Extension from 2D to 3D & numerical simulations . . .	24
2.1.3 Magnetic effects: MRI turbulence, Dead zones, & new resonances . . . . .	34
2.1.4 Summary of the tidal torque . . . . .	44
2.2 Protoplanetary disks and their evolution . . . . .	46
2.2.1 Disk structure: flared disks . . . . .	47
2.2.2 Disk & dust evolution: dust settling . . . . .	53
2.2.3 The effect of radiative disks on migration . . . . .	60
<b>Chapter 3 Computational techniques</b>	<b>64</b>
3.1 Radiative transfer : Monte Carlo method . . . . .	65
3.2 Coordinate systems in RADMC . . . . .	71
3.2.1 Spherical coordinates . . . . .	71
3.2.2 Cylindrical coordinates . . . . .	74

3.3	Convergence tests for RADMC . . . . .	77
3.3.1	Benchmark tests for RT codes . . . . .	77
3.3.2	Results of our benchmark tests for modified RADMC .	88
3.3.3	Results of our convergence tests of dust size distribution & disk temperature . . . . .	91
3.4	Results of our convergence tests for the Lindblad torque calcu- lation . . . . .	100
3.4.1	Results of test: the reduction of disk size . . . . .	102
3.4.2	Methodology & Disk model . . . . .	104
3.4.3	Torque calculations . . . . .	106
3.4.4	Results of tests of the torque at Lindblad resonances .	107
<b>Chapter 4 Results: The effect of the dust settling on planetary mi- gration</b>		<b>115</b>
4.1	Models of dust settling & disk parameters . . . . .	115
4.2	Results . . . . .	116
4.3	Discussion . . . . .	131
<b>Chapter 5 Conclusions</b>		<b>134</b>

# List of Figures

1.1	Plot of the number of exoplanets as a function of planetary semi-major axis . . . . .	2
1.2	Schematic figure of transit method . . . . .	5
1.3	The observed light curve of the OGLE-2005-BLG-390 due to gravitational microlensing event . . . . .	6
2.1	The positions of Lindblad resonances around a planet with orbital radius, $a$ . . . . .	12
2.2	The normalized torque density as a function of distance from the planet in the unit of the disk scale height . . . . .	15
2.3	The horseshoe orbit and the streamline in the vicinity of a planet	17
2.4	The density evolution with time in the massive planet . . . . .	23
2.5	The migration rate, accretion rate and growth rate as a function of $q = M_p/M_*$ . . . . .	31
2.6	The mid-plane density contours and torque per unit mass exerted on the planet for $M_p = 10M_\oplus$ . . . . .	35
2.7	The time evolution of the disk and planetary orbital radius for $M_p = 10M_\oplus$ . . . . .	37
2.8	The time evolution of the disk and planetary orbital radius for $M_p = 1M_J$ . . . . .	38
2.9	The distance of the outer turning points and magnetic resonances for $\beta = 10$ . . . . .	40
2.10	The total torque as a function of $m$ for unmagnetized disk ( $B = 0$ ) and magnetized disk ( $\langle B^2 \rangle \propto r^{-3}$ ) . . . . .	41

2.11	The disk surface density at $t = 5$ and $t = 10$ . . . . .	42
2.12	The picture of HH30 with time evolution . . . . .	47
2.13	The resultant SED produced by flared disk model heated by mainly radiation of the central star and viscosity . . . . .	51
2.14	The dust-to-gas ratio in a 1D vertical slice calculation at 10 AU .	57
2.15	The SED and shape of the $\tau = 1$ surface as a function of time for dust settling. . . . .	60
3.1	Temperature correction frequency distribution . . . . .	70
3.2	Projection of a path of a photon into cylindrical and Cartesian coordinate system . . . . .	72
3.3	Difference of temperature and SED for the most optical thin case ( $\tau_v = 0.1$ ) . . . . .	83
3.4	Radial temperature and its difference for the most optical thick case ( $\tau_v = 100$ ) . . . . .	84
3.5	Vertical temperature and its difference for the most optical thick case ( $\tau_v = 100$ ) . . . . .	86
3.6	Percentage of difference in the SED between codes for optical depth ( $\tau_v = 0.1$ ) . . . . .	87
3.7	Percentage of difference in the SED between codes for optical depth ( $\tau_v = 100$ ) . . . . .	88
3.8	Two dimensional temperature distribution for the most optical thin case ( $\tau_v = 0.1$ ) . . . . .	89
3.9	Radial temperature and its difference and vertical temperature and its difference for the most optical thin case ( $\tau_v = 0.1$ ) . . . . .	90

3.10	The density and temperature plots of the disk around VLMS . . .	95
3.11	Radial temperature and its difference and vertical temperature and its difference for the disk around VLMS . . . . .	97
3.12	The density and temperature plot of the disk around CTTS . . .	98
3.13	Radial temperature and its difference and vertical temperature and its difference for the disk around CTTS . . . . .	100
3.14	The density and temperature plot of the small disk around VLMS	102
3.15	Radial temperature and its difference and vertical temperature and its difference for the disk around VLMS . . . . .	103
3.16	The Migration time of a $1 M_{\oplus}$ planet in the disk around VLMS .	109
3.17	The scale height and its difference for a $1 M_{\oplus}$ planet at various orbital radii . . . . .	110
3.18	The density and temperature structure of VLMS disk with a $1M_{\oplus}$ planet at 4.1 AU . . . . .	111
3.19	The density and temperature structure of VLMS disk with $1M_{\oplus}$ planet at 4.1 AU . . . . .	112
3.20	The Migration time of $1 M_{\oplus}$ planets in the disk around VLMS . .	113
4.1	The density and temperature structure of VLMS disk with $0.1M_{\oplus}$ at 2.1 AU . . . . .	117
4.2	The density and temperature structure of VLMS disk with $1M_{\oplus}$ at 2.1 AU . . . . .	118
4.3	The density and temperature structure of VLMS disk with $5M_{\oplus}$ at 2.1 AU . . . . .	119

4.4	The density and temperature structure of VLMS disk with $10M_{\oplus}$ at 2.1 AU . . . . .	120
4.5	The density and temperature structure of VLMS disk with $0.1M_{\oplus}$ at 2.1 AU . . . . .	121
4.6	The density and temperature structure of VLMS disk with $1M_{\oplus}$ at 2.1 AU . . . . .	122
4.7	The density and temperature structure of VLMS disk with $5M_{\oplus}$ at 2.1 AU . . . . .	123
4.8	The density and temperature structure of VLMS disk with $10M_{\oplus}$ at 2.1 AU . . . . .	124
4.9	The vertical structure of normalized torque, torque, density, and temperature of VLMS disk with $0.1M_{\oplus}$ at 2.1 AU . . . . .	125
4.10	The vertical structure of normalized torque, torque, density, and temperature of VLMS disk with $1M_{\oplus}$ at 2.1 AU . . . . .	126
4.11	The vertical structure of normalized torque, torque, density, and temperature of VLMS disk with $5M_{\oplus}$ at 2.1 AU . . . . .	127
4.12	The vertical structure of normalized torque, torque, density, and temperature of VLMS disk with $10M_{\oplus}$ at 2.1 AU . . . . .	128
4.13	The migration time as a function of the planetary position . . . . .	130
4.14	The migration time as a function of the planetary mass . . . . .	131

# List of Tables

1.1	Summary of low-mass exoplanets . . . . .	4
3.1	Summary of parameters used in the benchmark tests . . . . .	80
3.2	Summary of resolution and the number of photons used by each code	80
3.3	The dust composition and abundance in our model . . . . .	93
3.4	Summary of grain sizes and mass ratio of dust used in VLMS and CTTS . . . . .	94
3.5	Summary of parameters used in VLMS and CTTS . . . . .	96
4.1	Summary of the ratio of migration time between with and without dust settling . . . . .	131

# Chapter 1

## Introduction

1995 was an important year for Astronomy and Astrophysics as the first extra solar planet was discovered by Mayor & Queloz (1995). This great discovery makes the meaning of the existence of life on this beautifully blue planet a more general scientific question. This first detected planet around 51 Peg is a gas giant like Jupiter, but with a surprisingly small orbital radius, about 8 million km ( $\sim 0.05$  AU), while Jupiter is at 5 AU from Sun. This unexpected discovery is supported by many similar findings. Fig. 1.1 shows the total number of the exoplanets as a function of the semi-major axis and that the peak value is 0.018 AU. These exoplanets are called hot Jupiters if planetary mass is larger than  $1M_J$ . The number of known exoplanets has increased to about 300 in a decade.

One of the most successful observational planetary discovery techniques is the radial velocity method, or Doppler method, which was used by Mayor & Queloz (1995). Almost all planets have been detected by this method. If a star has planets, it orbits about the system's common center of mass. This motion causes a Doppler shift of stellar spectral line, the so-called wobble, that is, it is red-shifted when a star moves away from us, and it is blue-shifted when a star moves toward from us. Thus, we must detect the shift due to planets over

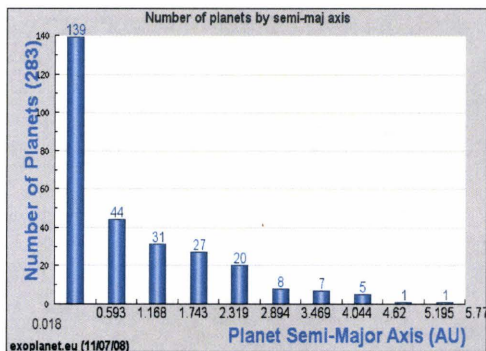


Figure 1.1: Plot of the number of exoplanets as a function of planetary semi-major axis. Its peak value is 0.018 AU. Adapted from <http://exoplanet.eu>.

at least whole one period. We can discover planets more easily as their mass increases and the distance between the star and planets is shorter as both of these conditions make their wobble bigger.

This productive spectroscopic method provides the properties of exoplanets in a statistical sense. The major finding is the variety of their orbital properties. Orbital radii range from about 0.02 AU to several AU, and the outer range increases as the observational limit is increased. Their eccentricity is widely spread from 0 to 1. For comparison, the eccentricity of the solar system is almost 0. The main trend of exoplanets is that their number increases as the mass decreases and as their distance from the host star is increased. It's still difficult to detect small-mass planets like Earth and planets with large orbital radii ( $\geq 5$  AU).

More particularly, the radial velocity method finds that, (1) there is no planet more than  $2.25M_{Jup}$  with an orbital period smaller than  $\sim 100$  days around single star, (2) the mass of planets increases as the distance from

the star increases, (3) the most massive planets with small orbital radii are members of companions of multiple star systems, and interestingly, their eccentricity is less than 0.05 when their orbital period is less than 4 days, and finally (4) their median eccentricity is 0.29 when the orbital period of exoplanets is more than 6 days, otherwise, their orbit seems to be circularized (e.g. Udry et al., 2007b).

A decade after the first discovery of an exoplanet, many improvements and developments of observational instruments have achieved an accuracy of  $1m/s$  for radial velocity measurements over months to years. This enables us to detect Neptune-mass planets around a few AU. Even when such high resolution instruments are used, one must still be very careful since stellar properties such as their oscillation and jitter wash out the change of radial velocity due to planets. Thus, we have to choose a slowly rotating, non-evolved, and low-activity star in order to detect small mass planets like Neptune and Earth. We summarize the recent discovery of low mass planets in Table 1.1.

Another important role of radial velocity surveys is to follow up on transiting planets, reviewed below. When combined with the transit method, we are able to derive accurate masses and radii of exoplanets, which makes it possible to estimate the mean density of planets. It's important to estimate the density of planets since this tells us the history of planetary formation.

The transit method, mentioned above, uses planetary eclipses. In other words, planets that orbit their stars with zero inclination allow one to estimate their mass from the Doppler method. When an exoplanet passes in front of its host star, its stellar brightness is decreased as shown in Fig 1.2. The measurement of this reduction of stellar luminosity with time enables us to

Table 1.1: Summary of low-mass exoplanets

Year	Planet	$M_p \sin i [M_\oplus]$	Period[days]	Reference
2005	Gl 581 b	15.6	5.3683	Udry et al. (2007a)
2005	Gliese 876 d	5.72	1.93776	Rivera et al. (2005)
2007	GJ 674 b	11.8	4.6983	Bonfils et al. (2007)
2007	Gl 581 c	5.02	12.932	Udry et al. (2007a)
2007	Gl 581 d	7.73	83.6	Udry et al. (2007a)
2007	HD 219828 b	19.1	3.8335	Melo et al. (2007)
2007	HD 285968 b	24.1	10.2366	Endl et al. (2008)
2008	HD 181433 b	7.57	9.37	*
2008	HD 40307 b	4.2	4.31	*
2008	HD 40307 c	6.87	9.62	*
2008	HD 40307 d	9.16	20.45	*
2008	HD 47186 b	4.08	22.8	*

asterisk represents these data is cited from <http://exoplanet.eu>

estimate the radius of the exoplanet. The derived planetary density is widely spread from 0.3 to 1.3  $g/cm^3$  while the density of Jovian planets in the solar system is 0.7 to 1.6  $g/cm^3$ , and density of terrestrial planets is 3.9 to 5.5  $g/cm^3$  (Udry et al., 2007b). Exoplanets discovered so far appear to be Jovian planets, but the difference of density suggests a greater variety of planet formation.

This photometric method also plays another important role in determining the atmospheres and interiors of planets. As an exoplanet starts to obstruct the star, the stellar luminosity probes the planetary atmosphere. The difference between the original stellar spectrum and the one modified by the planetary passage provides the composition of planetary atmosphere. The compositions detected so far are  $TiO$ ,  $VO$ ,  $H_2O$ ,  $CO$ ,  $Na$ ,  $K$ ,  $CH_4$  (e.g. Demory et al., 2007; Fortney, 2008). Once the composition of the atmosphere is given, the evolu-

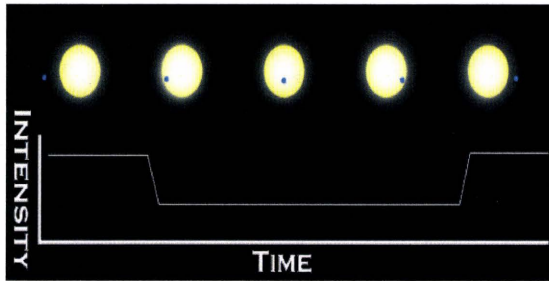


Figure 1.2: Schematic figure of transit method. Yellow big dot denotes the primary and blue small dot denotes a planet. This schematic figure shows that intensity of the primary is reduced as a planet pass in front of the hosting star. Adapted from <http://www.psi.edu/esp/process.html>.

tion of the atmosphere and structure of its interior can be investigated and compared with the knowledge of solar Jovian planets.

These planetary detection methods are powerful tools, but there is a detection limit, that is, only exoplanets within 1 kpc ( $\approx 2 \times 10^5$  AU) can be detected. The gravitational microlensing method is useful for exoplanets much farther from us such as planets in M31, the Galactic Bulge, Halo and Galactic disk ( $\sim$  several kpc). This method uses the effect of general relativity, in which light is bent by a gravitational field. When a star passes between us and the background star, luminosity from the background star is bent by the gravity of passing star, which produces a characteristic broad light curve. In addition, if this passing star has planets, brief spikes are formed in the broad light curve due to the gravity of planets, as shown in Fig. 1.3. Interestingly, the first low-mass planet ( $\sim 5.5M_{\oplus}$ ) was discovered by this method (Beaulieu et al., 2006). This super Earth is orbiting around the M dwarf, OGLE-2005-BLG-390L at

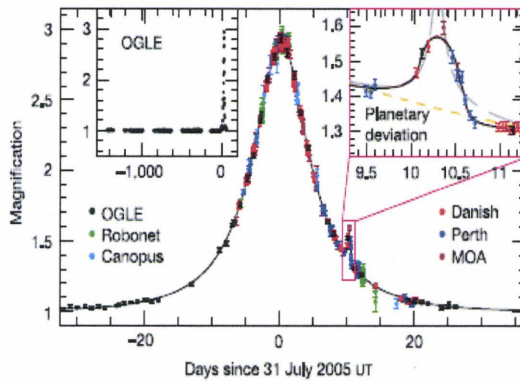


Figure 1.3: The observed light curve of the OGLE-2005-BLG-390 due to gravitational microlensing event. Small spiky curve in the large Gaussian-like curve is produced by a planet. Adapted from Beaulieu et al. (2006).

about 2.6 AU. Recently, Bennett et al. (2008) have discovered a  $3.3M_{\oplus}$  around the low-mass star.

Interestingly, more than half of the exoplanets detected by the gravitational microlensing method are low-mass planets although this method is about 20 times more sensitive to gas giants than to Super Earths at a few orbital radii. This implies that low-mass planets like Earth and Neptune are more common than gas giants like Jupiter. This method is suitable for taking the statistics of exoplanets in other Galaxies far from us because of its advantage of distance.

Also another interesting search is planned by looking at nearby planets where the radial velocity and transit methods can be used to make follow-up measurements (Di Stefano & Night, 2008). When we observe a gravitational microlensing event which is caused by a dwarf star with a planets within 1 kpc, the probability that we can detect a brief spike within broad light curve is the

highest when a planet orbits around the dwarf star at about 0.13 AU -which corresponds to the Einstein radius. Interestingly, the orbital radius of the habitable zone (HZ) around the dwarf star also lies at about 0.13 AU. This lucky coincidence allows us to search for life bearing worlds in the universe efficiently.

Thus, discoveries of exoplanets by various observational methods provide many interesting questions that one must answer. In this thesis, we address the question of the existence of hot Jupiters. The discoveries of these gas giants with very small orbital radii motivate the proposal of planetary migration, which arises from the tidal interaction with protoplanetary disk, and which is reviewed in Chapter 2. Although many intensive works about planetary migration analytically and numerically have been done, they have assumed disks to be isothermal in the vertical direction. As reviewed in Chapter 2, disks are heated by a star, and their shape is determined by the balance between heating and cooling. Thus, the isothermal assumption is far from the real disks. Therefore, we consider the effect of the stellar radiation on planetary migration. The temperature structure in disks is very important because the tidal interaction between a planet and the gas is very sensitive to the temperature structure of disks. Furthermore, dust, which is the dominant absorber of the stellar radiation, settles into the mid-plane with the grain growth. Thus, the temperature in disks evolves with time due to dust settling. This obviously changes the migration time. Moreover, we focus on planets around a very low mass star such as M dwarf. As mentioned above, a super-Earth has been discovered around a M dwarf. This discovery is very interesting for various scientific questions such as the origin of life.

We use the Monte Carlo technique in order to determine the disk temperature. The Monte Carlo method is very useful to determine the temperature structure in various dust configurations, which is discussed in Chapter 3. Our aim is to estimate the migration time by calculating the Lindblad tidal torque. Thus, we can calculate the temperature structure in disks, which enables us to estimate the resonances associated with these torques accurately. In Chapter 4, we show our results, and discuss the effect of dust settling on planetary migration. We found that dust settling strongly affects the migration. This is because the density and temperature structure are changed. In order for our calculations to be completely self-consistent, we take into account the effect of gravitational force of planets on density structure. We found that this effect works in a similar way to dust settling. Also we found the migration time for M dwarf system is longer than or comparable to the disk lifetime, which is a ten to hundred million years. This implies that planets around a M dwarf are saved from plunging into the central star without the need to invoke any special disk properties such as dead zones. It remains true, however, that planets around classical T Tauri star need some mechanisms to prevent them from plunging into the star.

## Chapter 2

# Planetary migration in gaseous disks

The discovery of extra solar planets provides some interesting challenges. One of most intriguing is the small orbital radii of the gas giants. Planetary migration has been proposed to explain this. Planets are not formed in-situ in this picture, but are formed far from the host star and then migrate inward due to tidal interaction with the surrounding gaseous protoplanetary disk (e.g. Ward, 1997).

Protoplanetary disks are the birthplace of planets and also play an important role in their orbital evolution. Disks are heated by their central stars. At the same time, dust in disks, which is the dominant absorber, re-emits the energy absorbed from the stars. This thermal balance causes the shape of disk to be concave, or "flared" (e.g. D'Alessio et al., 1998). Another important aspect of disks is their evolution. The size of dust grains grows with time, which causes dust settling (e.g. Chiang et al., 2001). Consequently, the disk's shape changes from a flared to a flat disk.

In this chapter, we provide an extensive review of the theory of planetary migration in § 2.1, and review disk structure and evolution in § 2.2.

## 2.1 Planetary migration

Planetary migration has been studied extensively after the first discovery of exoplanets, but the idea of migration was suggested in 1980 by Goldreich & Tremaine (1980), hereafter GT80. Work done by Goldreich & Tremaine (1979), hereafter GT79, and GT80 showed that the external potential in a gaseous disk exerts a tidal torque on the surrounding disk only at Lindblad and corotation resonances. The Lindblad torque excites density waves in a gas disk, which propagate away from these resonances. Consequently, the external potential loses angular momentum, and the disk gains angular momentum. The corotation torque does not excite density waves so that it's finally saturated unless there are removal mechanisms of accumulated angular momentum around corotation resonances, such as viscosity. If we apply this idea to a planet-disk system, wherein the external potential is considered as a planet, then we can explain planetary migration. We review the basic mechanism of planetary migration and three types of migration in the detail in § 2.1.1, extension from 2D to 3D and numerical simulations in § 2.1.2, and magnetic effects on tidal torque in § 2.1.3. In § 2.1.4, we provide summary of the tidal torque.

### 2.1.1 Basic physics: Lindblad and corotation resonances & three types of migration

First, we review the Lindblad resonances, and then corotation resonances. Finally, we review the three types of migration, which is a classification due to the planetary mass and dominant torques, either Lindblad torques or corotation torques.

The analytical formula of the tidal torque at Lindblad resonances was first derived by GT79. They considered an external potential in 2-D gaseous disk, in which the disk is assumed to be very thin. They treated the external potential as a perturber and solved the linearized Euler equation. Lindblad resonances are resonances where the orbital frequency of the gas,  $\Omega$  in the co-moving frame with a planet called the Doppler shifted forcing frequency, is equal to the epicyclic frequency,  $\kappa$ :

$$D = \kappa^2 - m^2(\Omega - \Omega_p)^2 (= 0), \quad (2.1)$$

where  $\Omega_p$  is the planetary frequency and  $m$  is the wave number. In order to solve the linearized Euler equation easily, the linearized differential Euler equation is Fourier-transformed so that the  $m$ th order Fourier component of the potential of the planet becomes

$$\phi_m = -\frac{GM_p}{r_p} b_{1/2}^m(\alpha_r), \quad (2.2)$$

where

$$b_{1/2}^m(\alpha_r) = \frac{2}{\pi} \int_0^\pi \frac{\cos m\theta d\theta}{\sqrt{1 - 2\alpha_r \cos \theta + \alpha_r^2}} \quad (2.3)$$

is the Laplace coefficient with argument  $\alpha_r = r/r_p$  and any quantities with  $p$  are evaluated at the planetary orbital radius. The forcing function due to the Fourier-transformed planetary potential is

$$\Psi_m = r \frac{d\phi_m}{dr} + 2mf\phi_m, \quad (2.4)$$

where  $f = m(\Omega - \Omega_p)/\Omega$ . Finally, their torque formula is

$$T_m^L = -\frac{\pi^2 m \sigma \Psi_m^2}{r dD/dr}, \quad (2.5)$$

where  $\sigma$  is surface density of the disk.

This analytical formula is confirmed by the numerical study done by Korycansky & Pollack (1993), hereafter KP93. They solved the linearized Euler equation derived by GT79 numerically in order to verify the approximation used by GT79. They found that the agreement is excellent.

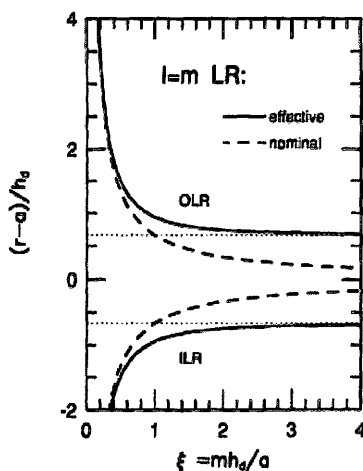


Figure 2.1: The positions of Lindblad resonances around a planet with orbital radius,  $a$ . The nominal positions (dashed line) are derived without gas pressure, and the effective positions (solid line) are derived with gas pressure. The dotted lines are at  $r = a \pm 2h/3$ , where  $h$  is the scale height. Adapted from Artymowicz (1993b).

As  $m$  is increased, the resonant positions move toward the planet, which implies that the torque increases infinitely, since  $rdD/dr$  is in the denominator of torque formula. Thus, the relationship between  $m$  and the positions of resonances is important, but the total torque is determined by the sum of all of  $m$ , which causes a problem since the tidal torque becomes infinite. GT80 avoid this problem by employing a so-called torque cut-off wherein the torque

is cut off to make it finite. This problem was finally solved by Artymowicz (1993b). He derived a generalized torque formula containing azimuthal gas pressure which was neglected by GT80. This gas pressure effect provides the natural explanation for a torque cut-off since resonant positions are pushed outward from the planet due to gas pressure as  $m$  is increased. Fig. 2.1 shows the positions of Lindblad resonances without this gas pressure effect, which are called nominal positions (dashed line) and with the gas pressure effect, called effective positions (solid line). Thus, the resonant positions converge to positions located at  $2h/3$  from the planets, where  $h$  is the scale height of the disk. This causes the total torque to be zero around a planet (also see Fig. 2.2) and to become finite without adding an artificial torque cut-off. The generalized resonant conditions and torque formula are below (e.g. Ward, 1997);

$$D_* = D - (mc/r)^2 = \kappa^2 - m^2(\Omega - \Omega_p)^2 - (mc/r)^2 (= 0), \quad (2.6)$$

where  $c$  is the sound speed, and the orbital frequency in co-moving frame with a planet is reduced due to gas pressure by  $(mc/r)^2$ , and

$$T_m^L = -\frac{\pi^2 m \sigma \Psi_m^2}{r dD_*/dr} \quad (2.7)$$

$$\Psi_m = \frac{rd\phi_m/dr + 2mf\phi_m}{\sqrt{1 + 4\xi^2}}, \quad (2.8)$$

where  $\xi = mc/r\kappa$ . Interestingly, the forcing function of the planet is also weakened by gas pressure because gas pressure counteracts the gravitational force of the planet.

We have considered the torque as a function of  $m$  so far. On the other hand, we can consider torque density which is a function of radius because

torque for relatively large  $m$  is the dominant contribution to the total torque and because the distance between resonant positions is small as  $m$  is increased (See Fig. 2.1). Thus, torque can be considered as a continuous function of distance from a planet and torque density is a practical way to calculate the total torque since it avoids the problem of finding the resonant positions for each  $m$ . The torque density can be defined (e.g. GT80; Ward, 1997);

$$\frac{dT^L}{dr} = T_m^L \left| \frac{dm}{dr} \right| \quad (2.9)$$

From Eq. (2.6), we find

$$\frac{dm}{dr} = -\frac{\partial D_*/\partial r}{\partial D_*/\partial m} = \frac{m}{2\kappa^2} \frac{dD_*}{dr}. \quad (2.10)$$

Finally, the torque density is

$$\frac{dT^L(r)}{dr} = \text{sgn}(r - r_p) \frac{2\mu^2 \sigma r_p^4 \Omega_p^4}{r(1 + 4\xi^2)\kappa^2} m^4 \psi^2, \quad (2.11)$$

where the modified forcing function  $\psi$  is

$$\psi = \frac{\pi}{2} \left[ \frac{1}{m} \left| \frac{db_{1/2}^m(\alpha_r)}{d\alpha_r} \right| + 2\sqrt{1 + \xi^2 b_{1/2}^m(\alpha_r)} \right], \quad (2.12)$$

and  $m$  becomes a continuous function of  $r$  below;

$$m(r) = \sqrt{\frac{\kappa^2}{(\Omega - \Omega_p)^2 - c^2/r^2}}. \quad (2.13)$$

Fig. 2.2 shows the torque density as a function of the distance from the planet. As mentioned above, the torque around the planet is zero due to the gas pressure, and it takes the maximum value around  $2h/3$  from the planet.

The direction of migration due to the Lindblad torque is determined by the balance between the inner torque which adds angular momentum to the planet

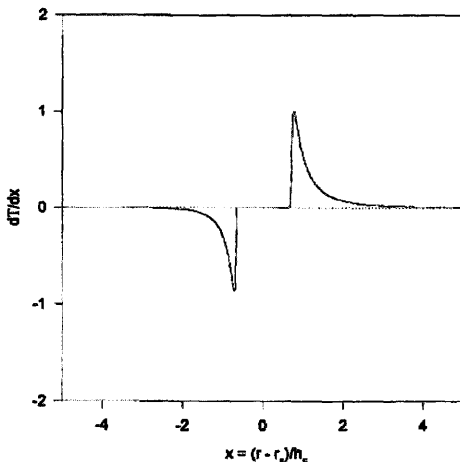


Figure 2.2: The normalized torque density as a function of distance from the planet in the unit of the disk scale height. Torque density around the planet is zero due to gas pressure. Adapted from Ward (1997).

and the outer torque which takes angular momentum from the planet. In addition, these angular momentum transfers excite density waves at the Lindblad resonances, and these waves propagate accumulated angular momentum away from these resonant points. Ward (1997) pointed out that gas pressure and surface density gradients conspire so that the outer torque is larger due to the following things: (1)  $rD_*/dr$  is always smaller for outer resonances, (2) outer resonances are closer to the planet than inner ones, and (3) the forcing function in outer resonances is larger than that of the inner ones even if these resonances are symmetrically located.

The analytical formula for corotation torque was also first derived by GT79 by using the linearized Euler equation in which the external potential was treated as a perturber. The corotation resonances are resonances that arises

when the orbital frequency of the gas  $\Omega$  is identical to the orbital frequency of the planet  $\Omega_p$ . They found that the corotation torque was controlled by the radial gradient of vorticity per unit surface density called vortensity. In other words, the direction of planetary migration is determined by the sign of the radial gradient of vortensity. Their torque formula is

$$T_m^C = \frac{m\pi^2}{2} \left[ \left( \frac{d\Omega}{dr} \right)^{-1} \frac{d}{dr} \left( \frac{\sigma}{B} \right) \phi_m^2 \right], \quad (2.14)$$

where

$$B = \frac{1}{2r} \frac{d}{dr} (r^2 \Omega) \quad (2.15)$$

is the Oort constant and called vorticity since this definition is the same as that of vorticity  $\vec{\omega} = \nabla \times \vec{v}$ ,  $\sigma$  is the surface density and  $\phi_m$  is the same as Eq. (2.2). Unlike the torque at Lindblad resonances, the corotation torque does not excite a density wave which can propagate the angular momentum accumulated at resonant positions. Thus, saturation occurs when the radial gradient of vortensity is zero.

This analytical formula was compared with the numerical one by KP93 in which the same linearized Euler equation as GT80 was solved numerically to make sure that the assumption GT80 used was valid. They found that the analytical torque at corotation resonances is larger than the numerical one. This discrepancy was solved by Tanaka et al. (2002), hereafter TTW02. They succeeded in reproducing the results of KP93 by replacing  $\phi_m^2$  with  $|\eta_m + \phi_m|^2$  in Eq. (2.14), where  $\eta_m$  is the  $m$ th Fourier component of the enthalpy perturbation. The agreement of corotation torque calculated by TTW02 with that of KP93 is excellent. Since the enthalpy is the pressure divided by density,

their work implies that gas pressure or temperature around the planet is crucial for a proper prescription of the corotation torque.

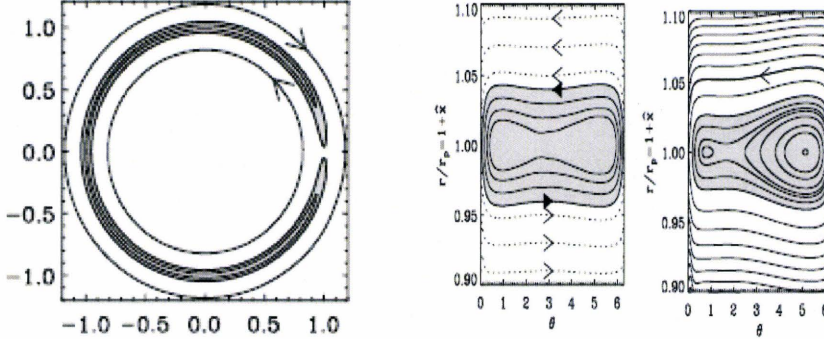


Figure 2.3: The horseshoe orbit and the streamline in the vicinity of a planet without viscosity (the central panel) and with viscosity (the right panel). In the left panel shows, the shaded area represents the horseshoe orbital region. For the central and right panel, the planet is at  $(r/r_p, \theta) = (1, 0)$ . The basic feature for the central and right panels is the same. There are three regions; the horseshoe region (shaded area), the circulating region (white region), and separatrix between the horseshoe and the circulating region is denoted by the solid line. Adapted from Masset (2001).

Although this pioneering work done by GT79 and GT80 was great, the relation between the angular momentum transfer between planets and disk and the gradient of the vortensity was not clear. Ward (1991) gave a clearer physical explanation for the corotation torque by considering the interaction with the fluid element near-by co-orbiting the planet in a horseshoe orbit. In the left panel of Fig. 2.3, the shaded area denotes the horseshoe orbit.

The fluid element in a horseshoe orbit interacts with the planet gravitationally and exerts a cumulative torque on the planet. The fluid element in a smaller orbital radius than that of the planet moves faster than the planet in the Keplerian disk. In the co-moving frame with the planet, it approaches

the planet from behind. Because of the gravity of the planet, it is shifted from smaller to larger orbital radius at the behind of the planet. During this interaction, the fluid element gains angular momentum from the planet since the specific angular momentum is proportional to  $\sqrt{r}$  if the disk is Keplerian. The fluid element moved from inner to outer orbit continues its circular motion due to adiabatic invariance. At the same time, the fluid element in an outer orbit compared with the planet is caught up by the planet, and its orbital radius is made smaller by the planet at the hair-pin curve in the horseshoe orbit, which is the closet point to the planet (See the left panel of Fig. 2.3). This fluid element loses angular momentum to the planet for the same reason as before. Thus, the planet gains angular momentum from the outer fluid element in the horseshoe orbit while the planet loses angular momentum from the inner fluid element in the horseshoe orbit.

The net torque arising from this interaction is determined by the imbalance of the mass mapping from outer orbit to inner orbit and vice versa. Ward (1991) showed that the radial gradient of vortensity is associated with the mapping between unequal differential areas. This imbalance is also associated with the surface density profile. Thus, the net torque is non-zero since the effect of the surface density profile ensures that the mass distribution in the inner region is not the same as that of the outer region. In addition, the area mapping shows that the area occupied by inner fluid element is smaller than that of outer fluid, which is characterized by the gradient of vortensity. Interestingly, the corotation torque is zero when the surface density is proportional to  $r^{3/2}$  and the disk is the Keplerian because the gradient of the vortensity cancels out.

Unlike the Lindblad resonances, a density wave is not excited due to angular momentum transfer since adiabatic invariance forces the fluid element to continue circular motion. Therefore, the angular momentum transferred by corotation torques becomes zero when the fluid element moves back to the original point. This motion is called libration. In other words, libration removes the gradient of vortensity after a timescale of the order of the turnover of the outermost horseshoe orbit (whose contribution to corotation torque is dominant since the distance from the co-orbital radius is maximum). In order to avoid saturation, viscosity is required. If the diffusion timescale over the horseshoe region is shorter than the turnover timescale, the removal of the vortensity gradient due to libration is prevented so that saturation does not occur.

Masset (2001) investigated the effect of viscosity on the horseshoe orbit for the case of a steady flow by focusing on the streamline topology, in which the disk is considered as 2D and the planet is in a fixed circular orbit. The central and right panel of Fig. 2.3 shows the streamline without and with viscosity, respectively. There are three regions; the horseshoe region (shaded area), the circulating region (white region), and separatrix between the horseshoe and the circulating region is denoted by the solid line. The streamlines in the horseshoe region are closed so that there is no exchange of angular momentum if the gradient of vortensity is zero. The streamlines in the circulating region are curved at the position of the planet which causes the waves to be excited, and corresponds to Lindblad resonances. Although there is a small difference between the case with and without viscosity in the horseshoe region due to the viscous torque as mentioned below, the basic picture is the same, which

results in the conclusion that the same mechanism of the angular momentum transfer works for the case with viscosity.

Masset found that viscosity plays two roles in corotation torque. One role is to prevent saturation, as we mentioned earlier. The other role is to exchange another torque with the planet because the fluid element in the horseshoe region moves inward due to viscous torque, which causes the difference of the streamline between the cases with and without viscosity (See the central and right panel of Fig. 2.3). During this drift, the fluid element in outer orbit of the planet gives the planet its angular momentum due to viscous torque so that it moves inward. Thus, the width of the horseshoe region, which is important for corotation torque, is controlled by viscosity as well as the planetary mass. If the disk is inviscid, this region is characterized only by the mass of the planet.

The corotation torque he derived is maximized when the diffusion timescale due to viscosity is much shorter than the turnover timescale of the horseshoe orbit (high viscosity) and it becomes zero when the diffusion timescale is much longer than turnover timescale (low viscosity).

Masset (2002) expanded this study from steady state to time dependent numerical calculations. He found that the corotation torque is saturated for low viscosity, and it is unsaturated for high viscosity. By varying the strength of viscosity, the corotation torque can be distinguished from the Lindblad torque. Also, he verified that the corotation torque is an increasing function of the planetary mass since the horseshoe region is increased with the planetary mass.

There are three types of migration, type I, II and III, which are controlled by the planetary mass, and their mass determines whether the Lindblad torque or the corotation torque is dominant.

Type I migration works for low-mass planets that can't open up gaps around planets (e.g. Ward, 1997). This type of migration occurs mainly due to Lindblad resonances because the corotation torque is saturated or very small compared with the Lindblad torque (although KP93 showed that the corotation torque is also effective in the net torque). The Lindblad torques for low mass planets are so weak that the density perturbation due to the torques can be treated by linear theory. The migration time is about three to four orders of magnitude smaller for several Earth mass planets than the disk life time, which is about ten million years.

As the planetary mass is increased to about ten Earth masses, the Lindblad torque becomes so strong that the density perturbation becomes non-linear. Ward (1997) tackled this problem by considering the steady state solution of the Navier-Stokes equation (or Euler equation if disk viscosity is zero) analytically. He found the critical planetary mass which is dependent on the disk viscosity. A larger planetary mass than this critical mass could not continue steady state migration because the Lindblad torque is too large to be treated by linear theory. For inviscid disks, the critical mass is about  $5M_{\oplus}$ . Migration for larger mass planets than this critical mass is called type II migration. The Lindblad torque caused by massive planets is so large that the density wave is damped just in the vicinity of the planets. This causes gap formation, that is, gas orbiting just inside the planet moves inward since gas just inside the planet loses angular momentum from the planet. For gas orbiting just outside

the planet, the situation is the opposite. In this type of migration, planets are locked to the gas and migrate due to disk viscosity which transfers the angular momentum. This type of migration is two to three order of magnitude slower than type I migration. However, this migration time is still two to three order of magnitude shorter than the disk life time.

This analytical estimate is confirmed by the numerical study done by Nelson et al. (2000). They considered type II migration by using three independently developed 2D Hydrodynamical (HD) codes. They found (1) the migration time of the Jovian planets placed at about 5 AU is about  $10^5$  years, which agrees with the analytical estimate, (2) the final mass of the planet is  $2.7 \leq M_p/M_J \leq 4.87$ , where  $M_J$  is the mass of Jupiter, (3) accretion does not affect the migration time very much, and (4) all the results produced by three codes are consistent. Fig. 2.4 shows the time evolution of the surface density. Two spiral density waves are launched from the massive planet, which corresponds to the waves excited at the Lindblad resonances. As time goes on, the gap is formed.

Masset & Papaloizou (2003) proposed Type III migration, which is still under the debate. This type of migration is believed to occur for medium-size mass planets like Neptune. Although Lindblad torques distinguish type I with type II migration, corotation torques are a discriminator of this type of migration. They considered this possibility both analytically and numerically. In the analytical approach, they derived the analytical corotation torque in steady state migration by taking a similar approach to Ward (1991). Thus, angular momentum is transferred at the U-turn of the horseshoe of gas. At this point, inner material moves outward compared with the planet so that

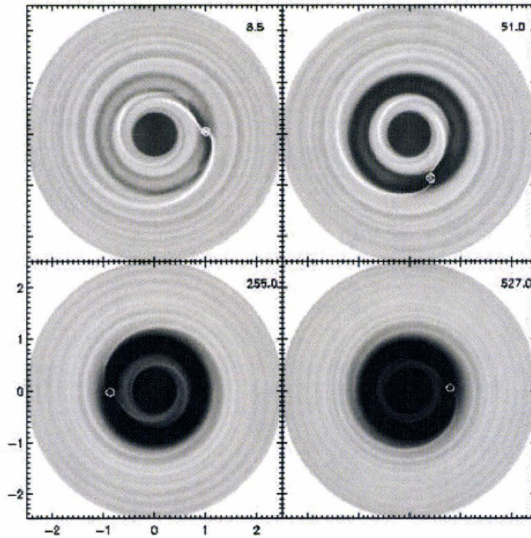


Figure 2.4: The density evolution with time in the massive planet. The density is represented by the gray scale; The whiter color is, the higher density is. The white circle denotes the position of the planet. The time is shown at the upper right corner in each plot. The gap is formed deeply with time. Adapted from Nelson et al. (2000).

inner material gains the angular momentum. In other words, the planet loses angular momentum from inner material. For outer material, the situation is the opposite, and the planet gains angular momentum from outer material.

In order to consider non-steady migration, they assumed that the total torque in the steady migration case is expanded by the migration rate,  $\dot{a}$ , and consequently they derived the first order differential equation for  $\dot{a}$ ;

$$\ddot{a} = -K\dot{a}, \quad (2.16)$$

where  $K$  is constant, and its sign is determined by the difference between the planetary mass and co-orbital mass deficit which is determined by the net

flow across the horseshoe region. They found that, when the planetary mass is larger than the mass deficit,  $K$  is a positive constant. Thus, the rate of change of migration rate is damped for very small or large planetary masses. On the other hand, when the planetary mass is smaller than the mass deficit,  $K$  is a negative constant. Thus, the rate of change of the migration rate increases exponentially. This is type III migration. One might be skeptical about analytical runaway migration since the Taylor-expansion in terms of  $\dot{a}$  is not valid when the planetary mass is smaller than the mass deficit.

They also conducted numerical simulations and confirmed analytical considerations although the size of grid they used is poor to get convergent results. Therefore, type III migration is still under debate although it's a very interesting idea. This type of migration time is short as well.

### 2.1.2 Extension from 2D to 3D & numerical simulations

In § 2.1.1, we reviewed the physical mechanism of planetary migration and its three types. The previous analyses still suffer from the low dimensionality and the assumed linear regime or other simplified treatments. As we review in § 2.1.2 and 2.2, protoplanetary disks are three dimensional objects and non-linear effects on the torque are very important to estimate the migration timescale more accurately. We review this in § 2.1.2. At first, the analytical extension from 2D to 3D is discussed, and then advanced numerical simulations are summarized.

The first extensions of the dimensionality from 2D to 3D for Lindblad torques were proposed by Ward (1988) and Artymowicz (1993a). The approach is to consider the disk to consist of many infinitesimally thin layers so that

the total torque is calculated by adding all of mass-averaged torque for each thin layer. Thus, this method is basically the same as that of 2D, except that the external potential was diluted by the vertical height. In other words, the vertical modes which are a purely 3D effect are not considered. The vertical modes or three dimensional modes are modes arising from the Hermite transform of the 3D Euler equations with respect to the distance  $z$  from the mid-plane. Density waves excited at resonances propagate in the direction of  $z$  due to these modes. On the other hand, the modes reviewed so far, or two dimensional modes, are modes arising from the Fourier transform with respect to  $r$ , and these propagate in the mid-plane.

This simple approach to a 3D disk is not so bad because of work done by Lubow & Ogilvie (1998). They considered the excitation and propagation of density waves at Lindblad resonances in a disk that has finite thickness and is thermally stratified, and modeled as a polytrope. They showed that the 2D modes, called  $f$ -modes in their paper, carry more than 95% of the torque and that truly three dimensional modes or vertical modes are not so important. Thus, the approach proposed by Ward (1988) and Artymowicz (1993a) is useful to take into account the 3D effect simply.

The full 3D analytical calculation was done by TTW02 by considering an isothermal, gaseous, three dimensional disk. They show that the tidal torque is reduced by a factor of 2 or 3 in 3D disk. The main difference between 2D and 3D is that there are vertical modes that couple with one another, which makes it difficult for the equation to be solved. They found that the total differential Lindblad torque is nonzero due to the following four asymmetries; (1) the term  $c/r\Omega$  associated with the curvature in cylindrical coordinates,

which is the same term pointed out by Artymowicz (1993b), (2) the surface density gradient, (3) the pressure gradient, and (4) the scale height, which is a purely 3D effect. The corotation torque is also non-zero due to these four asymmetries, although 2D modes arising from pressure gradient and scale height variations are zero, causing a large difference between 2D and 3D torque.

(1) Asymmetry arising from the curvature term, ie, gas pressure effect, is reduced in 3D which results in making the tidal torque weaker. This is because the gravitational force of the planet is averaged over the vertical direction. This causes the total differential Lindblad torque and the corotation torque in 3D to be about 60% and 50% of that of 2D, respectively when the disk has uniform surface density and constant scale height.

(2) The effect of the gradient of surface density on Lindblad torque is relatively small and the total torque in 3D is slightly smaller than that in 2D. For corotation, the torque arising from this effect is equal to  $-2/3$  of the torque due to curvature effect.

(3) The effect of the pressure gradient is the dominant term for differential Lindblad torques. Although they consider an isothermal disk, they treat pressure independently by using the fact that the pressure is determined by  $P = \sigma h c_s^2$  under the thin disk approximation, where  $\sigma$  is the surface density,  $h$  is the scale height, and  $c_s$  is the sound speed. They found that the total Lindblad torque in 3D is as small as 24% of that in 2D. This is because the forcing term is averaged for the vertical direction as well as the curvature term. This contribution to the corotation torque is not so large since the 2D modes of torque are zero.

(4) The purely 3D effect of scale height also plays a role in reducing the Lindblad torque. The increase of scale height with radius causes averaging of the forcing term in the outer torque to be more efficient. Consequently, the total torque is weaker. This effect on the corotation torque is negligible since the contribution of 2D modes of torque are zero.

Thus, the total differential Lindblad torque in 3D is weaker than that of 2D because of averaging of the gravity of the planet associated with the curvature term, surface density, and the pressure term and of radial variation of scale height, which is a purely 3D effect. The corotation torque is also affected by these four asymmetries and 3D effects.

Finally, TTW02 derived an analytical formula for the sum of the Lindblad and corotation torque in 3D and 2D isothermal disks;

$$\Gamma_{3D} = (1.364 + 0.541\alpha) \left( \frac{M_p r_p \Omega_p}{M_* c} \right)^2 \sigma_p r_p^4 \Omega_p^2, \quad (2.17)$$

$$\Gamma_{2D} = (1.160 + 2.828\alpha) \left( \frac{M_p r_p \Omega_p}{M_* c} \right)^2 \sigma_p r_p^4 \Omega_p^2, \quad (2.18)$$

where  $-\alpha$  is the power of the surface density with radius,  $M_*$  is the stellar mass, and the scale height is assumed to be proportional to  $r^{3/2}$ . Thus, the tidal torque is usually positive since  $\alpha$  is positive for protoplanetary disks. This causes the planets to migrate inward. When  $\alpha = 0$ , that is, the surface density is uniform, the torque in 3D is larger than that of 2D because the effect of the pressure gradient (that makes torque larger) is emphasized due to the scale height variation. The  $\alpha$ -dependence of torque in 3D is weaker than that of 2D because of the vertical average of the pressure and gravitational force in 3D.

Now we are in a position to review the numerical simulations. It is worth mentioning that 2D and 3D HD numerical simulations are highly time consuming computationally so that only a few hundred or thousand orbital timescales can be performed so far. Thus, the current computational facilities could not allow us to perform the full time evolution of the migration when the full HD equations are solved.

Miyoshi et al. (1999) performed local two and three dimensional simulations to ascertain the importance of non-linear effects on the tidal torque. They assumed the disk to be isothermal and adopted the shearing sheet approximation. They calculated the one-sided torque because they could not calculate the imbalance between the outer and inner torque since every quantity is symmetric with respect to the planet due to their approximation. They found that the behavior of tidal torque in 3D is similar to that in 2D. The reason is that the velocity field in  $y - z$  plane is mainly horizontal except for the shock front and that the streamlines at the shock front in 3D are very similar to that of 2D. They also found that the agreement for low mass planets is excellent while the numerical one deviates from the analytical one for massive planets for both a 2D and 3D disk. The 3D torque itself is weaker than that in 2D by a factor of 0.43 due to the vertical averaging of the gravitational force. Unlike the 2D case, non-linear effects in 3D disks strengthen the torque of each mode as well as weaken it, which results in the small deviation in 3D disks compared with that in 2D. Thus, analytical calculations of torque are good approximations for the low mass planets whose Hill radii are smaller than the disk scale height.

Kley et al. (2001) conducted global three dimensional numerical simulations. They considered isothermal disks in which the Jovian-type planets were placed. They investigated gap formation and calculated the accretion rate and torque, and compared them with 2D calculations. The agreement of these quantities in 3D with those in 2D is excellent. The gap formed in 3D is identical with that of 2D and the accretion rate and torque in 3D is almost the same as those of 2D. The resultant migration time for  $1M_J$  is about  $10^5$  years, which corresponds to the linearized analytical estimate. Thus, 2D calculations are adequate when the Hill radius or Roche lobe of the planet is similar to or larger than the disk scale height.

To summarize our discussion so far, we know that the analytical theory is an adequate approximation for low mass planets in steady state, and that two dimensional numerical simulations are valid for the case of high mass planets. In these studies, however, time-dependence for low mass planets is neglected and the detailed accretion process for low and high mass planets is beyond consideration due to the coarse grid although they are very important. It's very difficult to consider these effects numerically, especially for low mass planets, because the perturbation produced by low mass planets is so small that very high resolution is required. In addition, the calculation time with high resolution becomes longer, which can be beyond the current computational capability without some additional technical refinements.

This barrier was overcome by D'Angelo et al. (2002), who conducted 2D numerical simulations in isothermal gas disks with low to high mass planets by using nested-grid techniques. A nested-grid is very useful when certain local regions need to be very high resolved. The basic idea is to place a local finer

sub-grid on the global coarse grid. The equation to be solved is integrated independently on every grid level, and at the interface between the different grid levels, the information is exchanged to conserve the quantities. This technique is very useful when considering disk-planet interactions, especially for small planetary masses that cannot form gaps.

D'Angelo et al. (2002) confirmed the formation of circumplanetary disks for any planetary mass, and calculated the torque, that is the position  $\times$  the force acting on the planet excluding some region defined by  $|r - r_p| \leq \beta$ , where  $r_p$  is the planetary position and  $\beta$  is free parameter. When the planet is treated as non-point mass, angular momentum transfer through the circumplanetary disk excites spin of the planet. On the other hand, in their simulations, the planet was treated as the point mass so that they could not take into account this effect correctly. That's why they excluded the mass within  $|r - r_p| \leq \beta$  which excites planetary spin. We discuss briefly the effect of  $\beta$  on the migration time later.

As we reviewed, linearized analytical theory states that the torque exerted on the planet by the outer disk is negative while torque exerted on the planet by the inner disk is positive. As a result, the planet loses its angular momentum and migrates inward. However, this situation can be reversed when the disk material very close to the planet is considered. They found that torque arising from circumplanetary disk is complicated and has the opposite trend compared with the analytical consideration. Moreover, this effect is increased when  $\beta$  is reduced since the region of circumplanetary disks, which is taken into account, is increased. Consequently, the direction of migration is reversed as  $\beta$  is smaller.

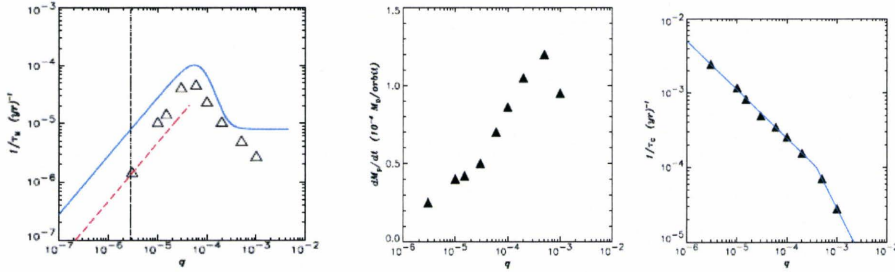


Figure 2.5: The migration rate, accretion rate and growth rate as a function of  $q = M_p/M_*$  in the left, central, and right panel, respectively. The triangle denotes the numerical calculations for every plot. In the left panel, the solid line is for Ward (1997), and the dashed line is for TTW02 in 2D disk. The vertical dot-dashed line represents the critical  $q$  that type I migration is always faster than type II. The solid line in the right panel is written in the text. Adapted from D’Angelo et al. (2002).

The left panel of Fig. 2.5 shows the migration rate as a function of  $q = M_p/M_*$ , where  $M_*$  is stellar mass. The triangles are the results of D’Angelo et al. (2002). The solid line denotes the migration rate calculated by Ward (1997), and the dashed line is the results of TTW02 for 2D disk. The vertical dot-dashed line represents the critical  $q$  for which type I migration is always faster than type II. Thus, type I migration to the right of this vertical line is always faster than type II. The left panel of Fig. 2.5 shows that the numerical simulation is always smaller than the solution of Ward (1997) because the Ward (1997)’s solution includes only the Lindblad torques. On the other hand, the agreement with the solution of TTW02 is better, especially for the lowest  $q$ , because the analytical formula includes corotation torques and it corresponds to linear regime. As  $q$  is increased, the agreement breaks down. This is because

of the non-linear effect and inviscid approximation in TTW02. In other words, the linear theory is a very good approximation for very small values of  $q$ .

Finally, they calculated the accretion rate (see the central panel of Fig. 2.5). For  $M_p \leq 0.2M_J$ , the growth timescale scales as  $M_p^{2/3}$ , while for more massive planets, it is approximated by  $M_p^{4/3}$  as shown in the right panel of Fig. 2.5. Thus, as the planetary mass is increased, the formation time is increased. This may imply that massive planets are rare.

D'Angelo et al. (2003) extended work done by D'Angelo et al. (2002) to 3D in isothermal gas disks. The main difference in the torque between 2D and 3D is that the contribution from the region very close to the planet is not so large that the sign of the torque could not be reversed. The main reasons are the vertical average of the gravitational force and the vertical resonances which are not taken into account in 2D. For more massive planets (type II migration), the numerical migration time is two times shorter than that of Ward (1997) because the solution of Ward (1997) considers only Lindblad torque. For small planetary masses (type I migration), the numerical result agrees with that of TTW02 except for the region between  $M_p = 7 - 15M_\oplus$ . This reason is not obvious, but possibly due to the non-linear effect. By comparing the 3D torque with the 2D one, they also found that for low mass planet in the regime of type I migration, the migration rate in 3D is lower than that of 2D. This is because of the averaging of the pressure and gravitational forces over the vertical direction. On the other hand, for massive planets undergoing type II migration, 3D migration rate is faster than that of 2D because the gap in 3D is not so deep compared with that of 2D due to the weak gravitational force.

D'Angelo et al. (2003) shows that the agreement of the accretion rate in 3D with that of 2D is very good for the planetary mass from  $20M_{\oplus}$  to  $1M_J$ . For lower mass planets, the accretion rate in 3D is lower than that in 2D, which is more reasonable. The accretion rate in 2D may be larger due to the lack of the spread of the density for vertical direction and the deep gaps.

Bate et al. (2003) also conducted 3D numerical simulations in isothermal disks. They used a very fine uniform grid in the vicinity of the planets to resolve these regions, otherwise a logarithmic grid is used. They confirmed the findings of D'Angelo et al. (2003); (1) the shock fronts are closer to the planets as the mass of the planets is increased, (2) the spiral shock in 3D is weaker than that in 2D, and (3) the migration time they calculated is the same as that of D'Angelo et al. (2003), that is, for the type I migration, the agreement with TTW02 is excellent while for the type II migration, it's faster than Ward (1997), and (4) the accretion rate of Bate et al. (2003) is qualitatively the same as that of D'Angelo et al. (2003), that is, its peak is around  $0.2M_J$  (See the central panel of Fig. 2.5), which is the critical mass to open a gap.

Bate et al. (2003) also found that a bowshock shape is dominant for massive planets while a (vertical) plane shock is more appropriate for low mass planets. For the accretion process in 3D, the mass flow above and below the planets (which is purely 3D effect) is more important than that of the horseshoe orbit. Unlike D'Angelo et al. (2003), they found the large contribution to the torque from the vicinity of the planet, which leads to outward migration. This may be because their resolution was not enough since they could not resolve the circumplanetary disk for the planetary mass below  $0.1M_J$ .

### 2.1.3 Magnetic effects: MRI turbulence, Dead zones, & new resonances

Magnetic fields play many important roles in Astrophysics. In star forming regions, it associated with the process of collapse and the formation of outflows. In disk evolution, they are considered as the source of disk viscosity (MRI; Magneto-Rotational Instability), although it is still under debate. In § 2.1.3, we review its role in planetary migration, which significantly changes the physical picture mentioned above.

As commented above, the origin of the disk viscosity has been one of the biggest problems because the usual viscosity such as molecular viscosity is too weak to explain the observed accretion rate. Balbus & Hawley (1991a) and subsequent work Balbus & Hawley (1991b) proposed a promising candidate for the origin of the viscosity -the MRI. They showed that a weakly magnetized disk still supports the MRI, so that significant angular momentum can be transferred. They also showed that this MRI results in magnetohydrodynamic (MHD) turbulence in disks.

Nelson & Papaloizou (2004) performed global 2D MHD simulations and local shearing box simulations of MHD disks. From the global simulations, they found that low mass planets less than  $10M_{\oplus}$ , conduct random walks in the disk. In the non-magnetized disk, the planets perturbs the disk so that angular momentum is transferred from the inner disk to the planets and from the planets to the outer disk (See Fig 2.4). In the magnetized disk, however, this picture is completely different. This is because the perturbation produced by the low mass planets is smaller than the fluctuations produced by the MHD turbulence. As a result, migration is controlled by the density fluctuations that

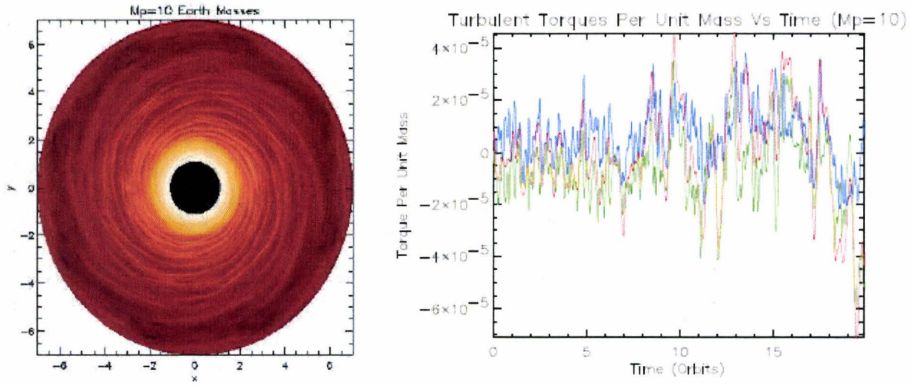


Figure 2.6: The mid-plane density contours and torque per unit mass exerted on the planet for  $M_p = 10M_\oplus$  on the left and right panel, respectively. In the left panel, the planet is at  $(x, y) = (-3, 0)$ . As shown in the right panel, it is very difficult to distinguish with the inner and outer torque, and their sign is changed very rapidly. This causes the planet to be in random walk. Adapted from Nelson & Papaloizou (2004).

result from the MRI. The left panel of Fig. 2.6 shows the mid-plane density contours for  $10M_\oplus$ . Compared with Fig. 2.4, the behavior of the density with MHD turbulence is disturbed by the resultant density fluctuation so that two spirals produced by the planets are not seen. This causes the torque exerted on the planet to strongly fluctuate (See The right panel of Fig. 2.6). It is very difficult to distinguish the inner and outer torques, and their sign is changed very rapidly. This torque behavior results in stochastic migration. The authors could not obtain convergent results for the torque because of the strong fluctuations.

As the planetary mass is increased, the migration becomes closer to that found in non-magnetized disks, which is also confirmed by Nelson & Papaloizou (2003). This is because the perturbation of the planet dominates the MHD

turbulent fluctuation so that density behavior is similar to that of a non-magnetized disk. Finally, sufficiently massive planets can open up gaps and then undergo type II migration. They also performed the shearing box simulation to examine the non-linear regime. They confirmed the same trend that low mass planets conduct random walks while for massive planets, the effect of fluctuations produced by MHD turbulence is less important (although the fluctuations they showed are smaller than the global simulations). In the local simulations, they had convergent results, and found that for low mass planets, the averaged torque is consistent with the linear analysis regime, and that as the planetary mass is increased, the non-linear effect becomes more important.

Stochastic migration is the outcome of the MRI. This MRI arises because the disk is magnetized due to gas ionized by cosmic rays or X-ray from the central star. Thus, the magnetization of disks is controlled by the ionization of gas that arises from the penetration of high energy particles from the outside of the disk. This implies that gas in the mid-plane is difficult to ionize since the probability that high energy particles reach the mid-plane is the lowest. In fact, a magnetically decoupled region is formed around the mid-plane, (called a dead zone (DZ), Gammie, 1996).

Oishi et al. (2007) took into account the effect of the DZ on turbulent torque by conducting a shearing box simulations in 3D disks. They found that DZ can reduce the turbulent torque by at least two order of magnitude relative to the fully ionized disk, and that the planets in DZ perform usual type I migration. Moreover, they implied that if the protoplanets are formed far from the DZ, they are captured in the DZ. Before that, they conduct random walk in the disk due to turbulent torque.

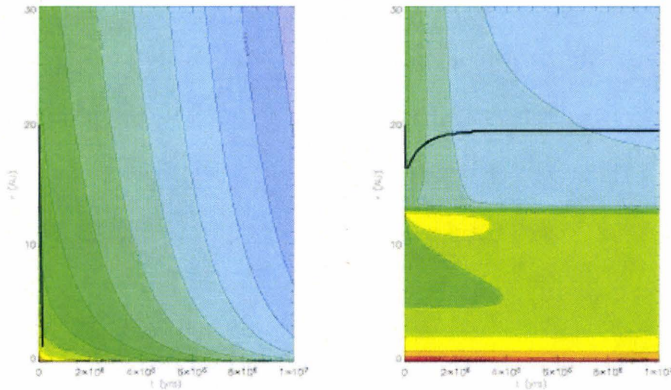


Figure 2.7: The time evolution of the disk and planetary orbital radius for  $M_p = 10M_\oplus$  without and with DZ at the left and right panel, respectively. Adapted from Matsumura et al. (2007).

Other effects of the DZ on the planetary migration were considered by Matsumura, Pudritz, & Thommes (2007). They conducted 1D numerical simulations in which a 1D hydro code for gas motion and N-body symplectic integrator to follow planetary orbits are combined. This hybrid code enables one to calculate the full time evolution of planetary migration, unlike any other HD or MHD simulations. They found that the DZs play two important roles in the usual planetary migration scheme. One is to reduce the critical mass to open up a gap, due to low viscosity in DZs, and the other is to slow down type II migration that arises from the disk viscosity. They also found that the viscosity jump arising at the boundary of the DZ causes a density jump. Fig. 2.7 shows the migration for a  $10M_\oplus$ . The planet's direction of migration is reversed by this density jump if there is a DZ in the disk (the right panel). The planet quickly migrates into the central star if there is no DZ in the disk

(the left panel). Fig. 2.8 shows the two role of the DZ. Without the DZ, the planet cannot open up a gap and plunges into the star (the left panel). On the other hand, with the DZ, it can form the gap within the DZ and its migration switches from type I to type II (the right panel). Moreover, this type II migration in DZ is slower than that outside of the DZ. Thus, Matsumura, Pudritz, & Thommes (2007) showed that DZs can save the planets from plunging into the central star.

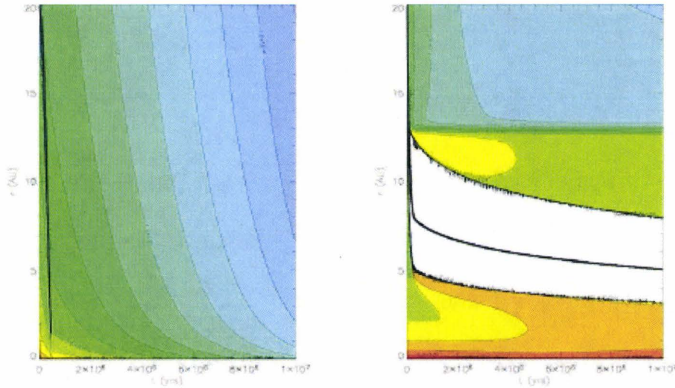


Figure 2.8: The time evolution of the disk and planetary orbital radius for  $M_p = 1M_J$  without and with DZ at the left and right panel, respectively. Adapted from Matsumura et al. (2007).

Another effect of magnetic fields on planetary migration was investigated by Terquem (2003), hereafter T03. She studied the effect of a toroidal magnetic field by solving the linearized ideal MHD equation in thin disks. She found new resonances, called magnetic resonances, in which the Doppler shifted fre-

quencies are equal to those of a slow MHD wave propagation along the field line

$$m^2(\Omega - \Omega_p)^2 = \frac{m^2 c^2 v_A^2}{r^2(v_A^2 + c^2)}, \quad (2.19)$$

where  $v_A = \sqrt{\langle B^2 \rangle / \mu_0 \sigma}$  is the Alfvén speed and  $\mu_0$  is the permeability of vacuum. If the right-hand side is replaced with epicyclic frequencies, it results in Eq. (2.1), that is, the Lindblad resonance conditions. These resonances correspond to the corotation resonances for unmagnetized disk because magnetic resonant positions,  $r_M$  are represented as;

$$|r_M - r_p| = \frac{2h}{3\sqrt{1 + \beta}}, \quad (2.20)$$

where  $r_p$  is the planetary orbital radius,  $h$  is the disk scale height, and  $\beta = c^2/v_A^2$ . When we consider the magnetic field to be infinitesimally weak ( $\beta \rightarrow \infty$ ), then  $r_M \rightarrow r_p$ . In other words, there is no corotation resonance for a toroidally magnetized disk and magnetic resonances are located between the Lindblad and corotation resonances. The torque at the outer magnetic resonances gains angular momentum from the planet as well as the Lindblad torques, and vice versa.

As for the Lindblad resonances, there are torque cut-off regions for magnetized disk whose boundaries are called turning points. The turning points are very important since the maximum contribution to the torque arises at these positions. For an unmagnetized disk, these points are located at  $2h/3$  from the planets (Artymowicz, 1993b), and the torque at these points are the largest (See Fig. 2.2). For a magnetized disk, there are three turning points (see Fig. 2.9). (1) The outermost turning points R1 is identical with the nominal Lindblad resonances for small  $m$ . For larger  $m$ , its distance from the co-orbital

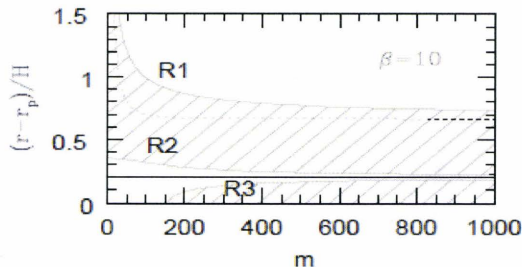


Figure 2.9: The distance of the outer turning points and magnetic resonances for  $\beta = 10$  is represented by the thin and thick solid line, respectively. The shaded areas denote the region where the waves are evanescent, and the dotted line is for the positions of effective Lindblad resonances in unmagnetized disk. Adapted from Terquem (2003).

radius is  $2h/3$  for  $\beta \geq 1$ , that is unmagnetized disks, and it is  $2h/3\sqrt{\beta}$  for  $\beta \leq 1$ , (2) the intermediate turning point R2 is located at  $2h/3\sqrt{\beta}$  for  $\beta \geq 1$ , and  $2h/3$  for  $\beta \leq 1$ , and (3) the innermost turning point R3 appears only for  $m$  which is above the critical value  $m_{crit} \simeq 1.5\sqrt{\beta}r/h$ . For  $m \rightarrow \infty$ , the distance from the co-orbital radius is  $2h/3\sqrt{\beta+1}$ . For either  $\beta \leq 1$  or  $\beta \geq 1$ , R2 and R3 coincides with each other at larger  $m$ . The main difference with the Lindblad resonances is that there is a region between R2 and R3. Moreover, as  $\beta$  increases, this region shifts inward and shrinks, and ends up disappearing when  $\beta \rightarrow \infty$ . The shaded areas in Fig. 2.9 represent the regions in which the waves are evanescent. Since the waves outside of the R1 propagates, the wave excited at the magnetic resonances containing between R2 and R3 may propagate by the singular slow modes although this mechanism is still not clear.

T03 also conducted numerical calculations of the torque because the global contribution is important for torques arising from magnetic resonances (un-

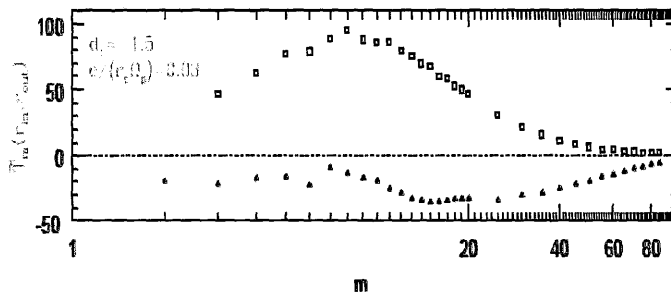


Figure 2.10: The total torque as a function of  $m$  for unmagnetized disk ( $B = 0$ ) and magnetized disk ( $\langle B^2 \rangle \propto r^{-3}$ ) is represented by the open squares and the filled triangles, respectively. Adapted from Terquem (2003).

like the Lindblad torque which is a point-like torque). Fig. 2.10 shows the normalized torque as a function of wavenumber  $m$ . The open squares are for an unmagnetized disk, while the filled triangles are for a magnetized disk with  $\langle B^2 \rangle \propto r^{-3}$ . The torque for an unmagnetized disk is always positive which causes the planet to migrate inward. On the other hand, the torque for a magnetized disk is negative which causes the planets to migrate outward. Thus, she found that the planetary migration can be slowed down or reversed when the toroidal magnetic field is a decreasing function of radius. This is because the torque in magnetic resonances increases with the strength of the magnetic field so that a magnetic field decreasing with the radius makes the inner torque stronger, and vice versa. Furthermore, the magnetic resonant positions are closer to the planet than those of Lindblad resonances so that magnetic torque dominates over the Lindblad torque. Thus, this study implies that when the planets migrate from an unmagnetized to a magnetized region, they can be stopped by the magnetic resonances.

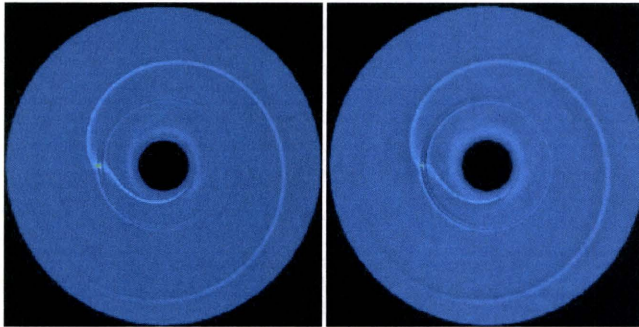


Figure 2.11: The disk surface density at  $t = 5$  and  $t = 10$  is shown in the left and right panel, respectively. The density is perturbed by the fast magnetosonic waves excited at the Lindblad resonances and the slow MHD waves excited at the magnetic resonances. Adapted from Fromang et al. (2005).

This toroidal magnetic effect on migration was confirmed by Fromang et al. (2005). They performed the 2D MHD numerical simulations and found that the migration for low mass planets is slowed down or reversed when the toroidal magnetic field is decreased with the radius. As Fig. 2.11 shows the surface density at  $t = 5$  for the left panel and at  $t = 10$  for the right panel in which non-dimensional time is used, the magnetosonic waves are launched at the Lindblad resonances (R1 in T03). These waves correspond to the waves excited at the Lindblad resonances when the disk is unmagnetized. The density perturbation due to these modes is similar to that of HD simulations (See Fig. 2.4). At the same time, slow MHD waves are excited in the vicinity of the planet. These waves propagate azimuthally, along the magnetic field line, and do not propagate radially very much because they are very tightly wrapped. Thus, the linear analytical treatment agrees with the non-linear treatment.

Another interesting point they found is that the re-adjustment time of the magnetic resonances is not so fast relative to the migration timescale. Thus, when the planets migrate inward, they approach the inner magnetic resonances that causes the inner torque to be stronger than the outer one, and vice versa. This causes the outward or inward migration so that the migration is slowed down.

As T03 implied, they also concluded that the mechanism of angular momentum transfer due to slow MHD waves is still not clear and implied that there are modes that tunnel through the regions between the launch locations of the fast magnetosonic waves and the slow MHD waves (the region between R2 and R3 in T03).

The effect of poloidal magnetic fields was investigated by Muto et al. (2008). They solved the linearized ideal MHD equations by assuming the local shearing-sheet approximation in 3D disk, and conducted numerical simulations with a nested grid method. They found two additional turning points as well as the three turning points T03 found. These two turning points arise from a three dimensional effect, which corresponds to a vertical mode, and Alfvén waves that propagate along the field line in the vertical direction.

For two dimensional modes, they found that the magnetic field acts only to increment of the sound speed. In other words, in the presence of the magnetic field  $c$  is replaced with  $c + v_A$ , where  $v_A$  is Alfvén speed. In these modes, the variation for vertical direction is prohibited so that any resonance except for Lindblad resonances does not work. Thus, the torque is weakened by the poloidal magnetic field since the torque cutoff region is extended due to the increase of the sound speed. This finding is important since the decreasing

of two dimensional modes, which are dominant relative to three dimensional modes, results in the reduction of the migration rate, whereas the inner torque dominates the outer one, as for the Lindblad torque.

#### 2.1.4 Summary of the tidal torque

The tidal torque arises from the resonant interaction with a surrounding gas disk at the Lindblad and corotation resonances. At the Lindblad resonances, angular momentum transfer excites density waves and is propagated by these waves. On the other hand, there is no transport mechanism of angular momentum at the corotation resonances. Thus, saturation occurs if disks are inviscid. At the corotation resonances, angular momentum is transferred due to the interaction with the fluid element near the planet. Unlike the Lindblad torque, the corotation torque is controlled by disk viscosity.

There are three types of migration. The type I migration arises for lower mass planets than about  $10M_{\oplus}$ . In this type of migration, the Lindblad torque dominates the corotation torque. The migration time of this type is three to four order of magnitude shorter than the disk lifetime. Type II migration arises for more massive planets. When the Lindblad torque exceeds the linear regime, type I migration switches to type II migration. In this type of migration, angular momentum is transferred by disk viscosity. The migration time of this type is two to three order of magnitude shorter than the disk lifetime. Type III migration arises for medium size planets. In this migration, the corotation torque dominates the Lindblad torque, and the former torque causes rapid migration (although it's still being debate). The migration time is the same order as that of type I.

Type II migration is well described by 2D calculations analytically as well as numerically. This type of migration in 3D disks is slightly faster than that in 2D. This is because the effect of vertical distance becomes almost negligible due to gap formation which plays a very important role in the type II migration. Because of gap, massive planets always perform type II migration although gap formation depends on planetary mass and disk viscosity. Although we discuss the effect of MHD turbulence and purely magnetic fields, as mentioned below, these magnetic effects do not play a role in type II migration.

For type I migration, the migration time in 3D calculations is longer than that in 2D by a factor of 2. This is conformed by analytically and numerically. The 3D torque is more accurate than that in 2D. For lower mass planets than a few Earth masses, 3D analytical approaches excellently agree with numerical ones. For more massive planets, we have to rely on the computation because the non-linear effects become not negligible.

We assumed disks to be unmagnetized so far. If disks are magnetized, other features become important. If disks are in MHD turbulence, the migration is stochastic due to the density fluctuation. Since MHD turbulence is controlled by the ionization rate of gas in disks, the stochastic migration is close to the usual one when disks have dead zones. For massive planets, which perform type II migration, the MHD density fluctuations are dominated by the tidal torque. These planets conduct the usual type II migration, as mentioned above. Thus, this effect is important for low mass planets. If there is a dead zone in disks, type I and II migration can be stopped or slowed down.

Now we summarize their effect on purely type I migration since type II is not affected. If the toroidal magnetic field acts in disks, the corotation res-

onances disappear. Instead, the magnetic resonances appear. This magnetic torque is dominant over the Lindblad resonances, and it is strengthened with stronger field. This implies that the migration can be stopped with decreasing magnetic field with radius. If disks are threaded by a magnetic field, there are two additional resonances. The torque is weakened by this poloidal magnetic field so that the migration can be slowed down.

## 2.2 Protoplanetary disks and their evolution

Protoplanetary disks have been studied extensively (see e.g. review Dullemond et al., 2007). The existence of disks is indicated by the excess of infrared (IR) emission of young stellar objects (YSOs). This is consistent with the idea that planets are formed from in such disks.

Today, we have many advanced observational instruments which allow us to observe disks by direct imaging with high resolution and resolved spectroscopy. Fig. 2.12 shows images taken by Hubble Space Telescope (HST) at different times. They show that the disk has a flared shape, and the jets are emitted from the inner part of the disk. These figures allow us to investigate the disk geometry by direct imaging. The observational method to study spatially unresolved disks, uses their spectral energy distribution (SED). One of the basic approaches in studying disks and their structure is performed indirectly through the comparisons of observed SEDs with ones that are produced by models of the density distributions and heating mechanisms of disks, reviewed in § 2.2.1. Intensive studies of SEDs provide us clues about disk evolution which is associated with the dust evolution, reviewed in § 2.2.2. Finally, we review the effect of radiative disks on the planetary migration in § 2.2.3.

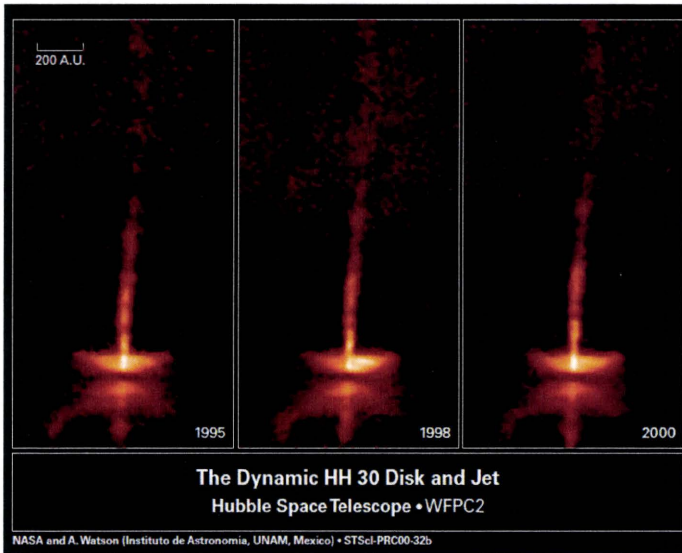


Figure 2.12: The picture of HH30 with time evolution. The disk shows the concave shape and the jets are emitted from the inner part of the disk. The year when the picture was taken is denoted at the bottom of the right hand side. Adapted from [http://hubblesite.org/gallery/album/entire\\_collection/pr2000032c/](http://hubblesite.org/gallery/album/entire_collection/pr2000032c/).

### 2.2.1 Disk structure: flared disks

When SEDs of YSOs are observed, an IR excess is common. This indicates that YSOs have material around the central illuminating protostars, which produces the IR emission. Otherwise, the SEDs would be well represented by the black body radiation of the protostars. The observational evidence raises the question of disk formation. This occurs because molecular cloud cores, which contract gravitationally and form protostars, usually have angular momentum and consequently cannot collapse directly into protostars. As a result, molecular clouds form circumstellar disks as well as protostars.

On the other hand, interesting questions remain about how disks emit in the IR and what disk structure succeeds in reproducing observed SEDs. These questions are answered by solving the radiative transfer equations (See Eq. (3.41) and (3.42)) under the assumption of vertical hydrostatic equilibrium, which is reviewed in detail in § 3.3.1. However, the radiative transfer equations, which depend on the frequency and local density structure, cannot be solved analytically without further assumptions, although they can be solved numerically by means of the-state-of-art computations. In analytical approaches, frequency integrated radiative transfer equations are solved. In other words, energy balance is considered under some assumptions. In computational approaches, the full radiative transfer equations are solved in 2D or 3D disk geometry by using various numerical schemes.

Analytical approaches started by specifying the emission mechanisms. Two models were devised for the heating mechanism of disks. Lynden-Bell & Pringle (1974) proposed viscous heating of disk in thin, flat disks. When disks are dissipated by viscosity and accreted by the central star, shearing stress produced by viscosity heats up the disks. They considered this as the primary heating mechanism. Another heating mechanism was proposed by Adams et al. (1987) in thin flat disks. They considered the illumination by the central star as the primary heating source. Interestingly, SEDs derived by Adams et al. (1987) are identical to those derived by Lynden-Bell & Pringle (1974) although their SEDs can not reproduce relatively flat observed SEDs.

This discrepancy was resolved by Kenyon & Hartmann (1987), who considered the disk shape. They expanded work done by Adams et al. (1987) by considering flared, not flat disks. This flaring is a consequence of the il-

lumination of disks by their central stars. Under the assumption of vertical hydrostatic equilibrium, the disk scale height is increased as the stellar intensity is absorbed. This is because the gas pressure, which is the counteractive force against the gravitational force of the star, is increased by the stellar energy absorbed by the disk. Thus, once disks are illuminated, the disk scale height is increased until the gas pressure is balanced with the stellar gravity. Moreover, once disks are flared, the outer part of flared disks can absorb more stellar energy than that of flat disks since the possibility that photons emitted from the star can be absorbed by the flared disks becomes higher than that of flat disks. As a result, the SEDs produced by flared disks are relatively flat, which corresponds to observations.

Another improvement of flared disk models whose heating mechanism is mainly stellar radiation, was done by Chiang & Goldreich (1997), hereafter CG97 and the subsequent Chiang & Goldreich (1999). They assumed that flared disks to consist of two layers, one of which is the upper layer that is heated directly by the stellar luminosity, so-called superheated layer, the other of which is the lower layer covered by the superheated layer. The lower layer is heated up by half of the energy emitted by the superheated layer. (The remaining half energy is emitted upward.) Thus, the disk temperature at each disk radius is represented by two characteristic temperatures. This model succeeded in reproducing the SEDs observed.

Thus, the emission from flared disks, which are heated by the stellar luminosity, can explain the IR excess in SEDs of YSOs although the detailed vertical structure was still unknown. Also, the effect of viscous heating, which may be a minor effect on SEDs, was not investigated. D'Alessio et al. (1998)

and subsequent work, D'Alessio et al. (1999) examined this. They assume disks to be flared. The heating sources they used are radiation from the central star, viscous heating, cosmic rays, and radioactive decay. They also consider the detailed vertical structure by taking into account the vertical energy transport mechanisms: turbulent flux, radiation, and convection. Thus, they solved energy transport equations with appropriate boundary conditions under the assumption of vertical hydrostatic equilibrium. They found that the main heating sources are direct radiation from the star and viscous heating. The former dominates the latter for  $r \geq 2$  AU whereas the latter surpasses the former for  $r \leq 2$  AU. Compared with disks that are purely heated by the viscous heating, a temperature inversion arises, that is, the surface temperature is higher than that of mid-plane since the surface layer is directly radiated by the stars. For the heat transport mechanisms in disks, the main contributor is radiative transport while the turbulent conduction is effective for small distances from the mid-plane. The effect of convection is negligible in this case.

The resultant SED of D'Alessio et al. (1998) is shown in Fig. 2.13, where the solid line represents the total SED of a star and a disk, the dotted line is for the star, and the dashed line is for the disk. In order to compare the model with observations, the observed SED of AA Tau is plotted with the squares and with error bars. This shows that their model succeeds in reproducing the observed SED. In addition, the SED produced by disks heated only viscously is also plotted (with the dot-dashed line) to show the effect of illumination of the central star. This obviously shows that the stellar radiation is more important than viscous heating to reproduce the observed SED. Thus, disk structure is

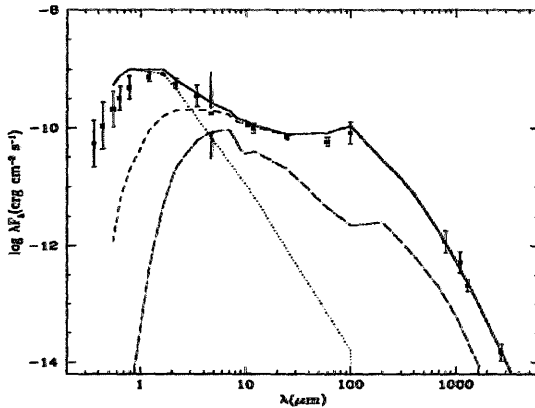


Figure 2.13: The resultant SED produced by flared disk model heated by mainly radiation of the central star and viscosity. The solid line denotes the total SED of a star and a disk, the dotted line is for the star, and the dashed line is for the disk. For comparison purpose, the observed SED of AA Tau is plotted by the squares with error bars, and SED produced by viscous heated disks and the star is denoted by the dot-dashed line.

regulated by the heating from the star and viscous heating although the former dominates the latter beyond about 2 AU.

While we have reviewed the analytical approaches so far, numerical approaches are also important because any analytical model requires some assumptions. There are two methods to compute SEDs numerically: Monte Carlo methods and ray-tracing methods. We briefly review these two methods because the detail of these methods, especially Monte Carlo methods, is reviewed in § 3.1.

Monte Carlo methods are easy to understand because they are very physical, as reviewed in § 3.1. In this scheme, the path of a photon packet is followed, where what happens is determined by the probability (e.g. Whitney

& Hartmann, 1992; Wood et al., 2002; Dullemond & Dominik, 2004b; Niccolini & Alcolea, 2006).

Ray-tracing methods are relatively abstract. In these schemes, the radiative transfer equations are directly integrated by using various numerical methods in order to get the specific intensity convergent; the Accelerated Lambda Iteration (ALI) method (e.g. Van Noort et al., 2002; Steinacker et al., 2003), the Complete Linearization (CL) method (e.g. Auer & Mihalas, 1969; Hubeny & Lanz, 1992), and the Variable Eddington Tensor (VET) method (e.g. Stone et al., 1992; Dullemond et al., 2002).

(1) the ALI method is to perform iterative calculations efficiently. The formal solutions to the radiative transfer equations state that the resultant intensity is determined by the disk temperature although disk temperature is determined by the absorption of the resultant intensity and the re-emission. Thus, the final intensity is described after iterations. The ALI method is devised to conduct this calculation efficiently.

(2) the CL method is another approach to solve radiative transfer equations. In this scheme, a set of physical quantities is considered, which is treated by linear algebra. This set of equations corresponds to the usual radiative transfer equations. Thus, by using the CL method, the integration of differential equations is replaced with matrix calculations.

(3) VET method is to modify the Eddington approximation. In the Eddington approximation, the second moment, which is  $\frac{1}{2} \int_{-1}^1 I_\nu(\mu) \mu^2 d\mu$ , where  $I_\nu$  is the specific intensity at frequency  $\nu$  and  $\mu = \cos \theta$ , is assumed to be proportional to  $I_\nu$ . This coefficient is determined by a reasonable guess. In VET method, this coefficient is adjusted so that full radiative transfer equations

are satisfied. Thus, VET method is more accurate version of the Eddington approximation.

### 2.2.2 Disk & dust evolution: dust settling

Disk evolution is strongly coupled to dust evolution because dust is the dominant absorber of the stellar radiation. In § 2.2.1, dust was assumed to be well mixed with gas, which corresponds to the early phase of disk evolution. As reviewed in this subsection, this coupling breaks as time goes on. This arises because the grain size of dust grows with time, resulting in the situation that gas pressure cannot support dust above the mid-plane. Consequently dust settles into the mid-plane.

At first, we review the size distribution of dust and its composition, and then we discuss dust settling, and its effect on disk heating and the SEDs.

In order to determine the size distribution of dust and its composition, we must at first consider models for them with some parameters, where optical quantities of each composition such as absorption cross sections, etc are calculated based on available laboratory and astronomical data, and then adjusted so that  $\chi^2$  is minimized, where

$$\chi^2 = \sum_i (C_{pred,i} - C_{obs,i})^2 / (\sigma_i C_{obs,i})^2, \quad (2.21)$$

where  $C_{obs,i}$  is observed quantity,  $C_{pred,i}$ , which is calculated by model used, is the counterpart of  $C_{obs,i}$ , and  $\sigma_i$  is a relative error associated with the observed quantities. Thus, the size distribution and dust composition are determined by comparing with the observed quantities.

The most famous and often used size distribution of dust was found by Mathis et al. (1977), so-called MRN distribution. They assumed the compositions of dust to consist of three of uncoated graphite, enstatite, olivine, silicate, carbide, iron, and magnetite, and assumed the size distribution to be power law

$$n(a) \propto a^p. \quad (2.22)$$

They found that when  $p$  is equal to -3.5 and graphite is included in the dust composition, the best fit to the observed extinction of interstellar medium (ISM) is achieved.

For the composition of dust, one of the most famous, but older (although still used) models was investigated by Draine & Lee (1984). They constructed dielectric functions for graphite and astronomical silicate based on available laboratory and astronomical data. These functions allow one to evaluate various cross sections such as the electric, magnetic dipole, and absorption cross sections. They also calculated the extinction curve based on MRN size distribution and found that their model reproduces the observed extinction curve.

Pollack et al. (1994) proposed another often used model, in which the following grain species are included; olivine, orthopyroxene, volatile and refractory organics, water ice, troilite, and metallic iron. By using available laboratory and astronomical data, theory, and the chemical composition of the primitive bodies in the solar system, they derived the real and imaginary indices of refraction of these species, and by using these indices they calculated various opacities such as the Rosseland mean and monochromatic opacities. The main difference of models by Draine & Lee (1984) is that carbonaceous species are included as organics, not as graphite.

Recently, another carbonaceous species, polycyclic aromatic hydrocarbons (PAHs) has been investigated. Li & Draine (2001) considered models to consist of amorphous silicate and carbonaceous grains, including PAHs. They succeed in reproducing the near-IR to submillimeter emission spectrum of the diffuse ISM, and also in reproducing the total IR emission of COBE/DIRBE observations. Moreover, the subsequent work, Draine & Li (2007), could reproduce the average Milky Way extinction curve as observed by Spitzer Space Telescope. Thus, PAHs seem to play an important role in dust composition although since PAHs are very large molecules, their formation mechanisms remain to be investigated.

Dust settling arises from decoupling with gas as the grains grow. In other words, the coupling or collision rate between dust and gas is crucial for dust settling. The reason why collisions between them are important arises from the difference of their motion (Weidenschilling, 1977). If there is no gas in disks, dust is in Keplerian motion. On the other hand, gas is affected by its pressure so that it's in slightly sub-Keplerian motion. Thus, friction (originating from gas-dust collisions) allows dust to stay suspended above the mid-plane. In the Epstein regime, which is applicable over the whole disk, the friction timescale is

$$\tau_f = \frac{\rho_s a}{\rho_g c_s}, \quad (2.23)$$

where  $\rho_s$  is the material bulk density,  $\rho_g$  is the gas density,  $a$  is the radius of a dust grain, and  $c_s$  is the sound speed. In other words, the size  $a$  of a dust grain is in the Epstein regime if  $\tau_f/\Omega_{Kep}^{-1} < 1$ . If the size  $a$  of dust grains increases, the friction timescale is increased. In other words, the collision rate is decreased, which results in dust settling.

As mentioned in § 2.2.3, disks undergo MHD turbulence arising from MRI. Dubrulle et al. (1995) treated this turbulent motion of gas as a counteracting effect against dust settling. They assumed that turbulence has a diffusive effect of dust in disks. They assumed that turbulence is described by  $\alpha$ -prescription by Shakura & Sunyaev (1973) and that the energy spectrum of turbulence is represented by the Kolmogorov type, that is,

$$E(k) \propto \left( \frac{k}{k_0} \right)^{-\gamma}, \quad (2.24)$$

where  $k_0$  is the wavenumber of the largest eddy, and  $\gamma$  is dependent on the nature of the turbulence. Under these assumptions, they determined the diffusion coefficient, and then solved the advection diffusion equation numerically. They found that large grains of dust settle downward to reach their equilibrium distribution in a turbulent diffusive timescale. Small grains are well-mixed and stay aloft. They also derived an analytical formula of the disk scale height of dust, which represents the degree of the dust settling and confirmed that the agreement of analytical formula with numerical solutions is excellent. Thus, the reduced scale height of dust  $h_d$  due to the dust settling is

$$\frac{h_d}{h} = \bar{H} / \sqrt{1 + \bar{H}^2}, \quad (2.25)$$

where the abundance ratio of scale height,  $\bar{H}$  is

$$\bar{H} = \left( \frac{1}{1 + \gamma} \right)^{1/4} \sqrt{\frac{\alpha}{\Omega_{Kep} \tau_f}}. \quad (2.26)$$

As mentioned above, for larger grains of dust,  $\bar{H}$  becomes smaller (See Eq. 2.23). This results in dust settling, that is,  $h_d \sim \bar{H}h$  ( $\bar{H} < 1$ ). On the other hand, for smaller grains,  $\bar{H}$  becomes larger. Consequently, dust does not settle;  $h_d \sim h$  ( $\bar{H} > 1$ ).

Schräpler & Henning (2004) also derived the diffusion coefficient by means of the mean field theory (MFT) in HD in order to consider dust settling. They used two different turbulent models;  $\alpha$ - and shear-induced turbulence. By solving the advection diffusion equation, they found that the roles of two different types of turbulence are opposite with each other although dust settling occurs for both models in the typical parameters of protoplanetary disks. Global  $\alpha$ -induced turbulence works as to prevent dust settling, as mentioned above, whereas local shear-induced turbulence does not counteract settling.

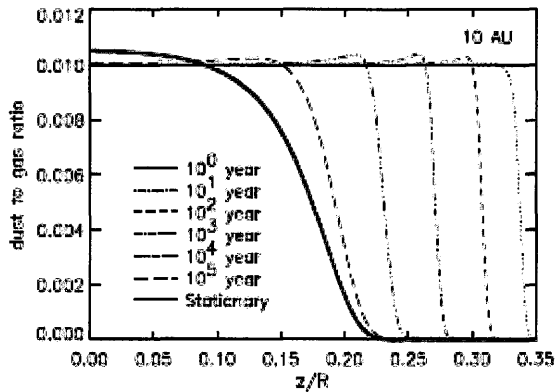


Figure 2.14: The dust-to-gas ratio in a 1D vertical slice calculation at 10 AU. At  $t = 0$ , dust-to-gas ratio is 0.01, ie, dust is well-mixed with gas. As time goes on, its ratio at the upper layer from the mid-plane is reduced. At  $t = 3 \times 10^5 \text{ yr}$ , its ratio reaches the stationary solution. Adapted from Dullemond & Dominik (2004a).

Dullemond & Dominik (2004a), hereafter DD, investigated dust settling by following Schräpler & Henning (2004) using  $\alpha$  turbulence, although they did not use the diffusion coefficient derived from MFT. Instead, they parameterized the diffusion coefficient which characterizes the decoupling between gas

and dust. The more dust is decoupled, the smaller is the diffusion coefficient used. As an example, Fig. 2.14 shows the dust-to-gas ratio as a function of vertical distance from the mid-plane at 10 AU from the star. At  $t = 0$ , dust-to-gas ratio is 0.01, that is, dust is well-mixed with gas. As time goes on, its ratio in the upper layer is reduced. As the distance from the mid-plane is increased, the settling velocity is increased. Thus, the dust density is reduced from the top layer in the disk, and it can catch up with dust just below the layer, resulting in a piled-up density layer and a clear boundary. Finally, its ratio reaches the stationary solution at  $t = 3 \times 10^5 \text{yr}$ .

In considering the turbulence, the  $\alpha$ -prescription was used so far, which is useful since the turbulence is treated without the detailed consideration of its origin. Furthermore, this  $\alpha$  turbulence enables us to assume dust settling to be described by the advection diffusion equation. This assumption must be verified by the MHD numerical calculations. Fromang & Papaloizou (2006) considered dust settling by performing numerical simulations using two different MHD codes. They assumed local shearing box simulations to be valid. They found that the agreement with two different codes is very good. Also, they confirmed that dust settling is accurately modeled by the advection diffusion equation with the diffusion coefficient which is calculated by the turbulence in disks.

The effect of dust settling on SEDs is obviously important. As the grains grow, dust settles into the mid-plane, implying that dust scale height is reduced. In other words, the disk shape transits from flared to flat since dust is the dominant absorber of the stellar radiation. This effect was investigated by Chiang et al. (2001). In order to take into account this effect, they artificially

reduced the disk scale height of dust by means of the improved models of CG97. Due to this reduction, the emission around at  $\lambda = 100\mu m$  is weakened, as expected. This is because the emission at these wavelength arises from the relatively outer part of disks, which can be directly radiated by the star if disks are flared, otherwise, it can be indirectly radiated. Thus, as the disk scale height of dust is reduced, the disk shape is changed from flared to flat so that the energy intercepted at the outer part of disks is reduced. Therefore, the emission around  $\lambda = 100\mu m$  is weakened.

D'Alessio et al. (2006) took a similar approach as Chiang et al. (2001) by means of techniques developed by a series of D'Alessio et al in order to estimate the effect of dust settling on SEDs. They considered two populations of dust, one of which consists of small grains, the other large grains. The former scale height is the same as that of gas, whereas the latter is reduced by 10%. They confirmed the same results as Chiang et al. (2001), that is, dust settling reduces the emission around  $\lambda = 100\mu m$ .

DD took into account the effect of dust settling by using disk models in which the dust distribution is calculated by the advection diffusion equation mentioned above. Their results are consistent with those of Chiang et al. (2001) and D'Alessio et al. (2006), as shown in Fig. 2.15. As time goes on, the emission around  $\lambda = 100\mu m$  is reduced for the same reason above. The transition of the disk shape is confirmed by the right panel of Fig. 2.15. The optical depth  $\tau$  is measured radially from the stellar surface outward at  $0.55\mu m$ . As dust settles to mid-plane,  $z_{\tau=1}$  is decreased. In other words, disks are changed from flared to flat for shapes. Note that in these calculations, the

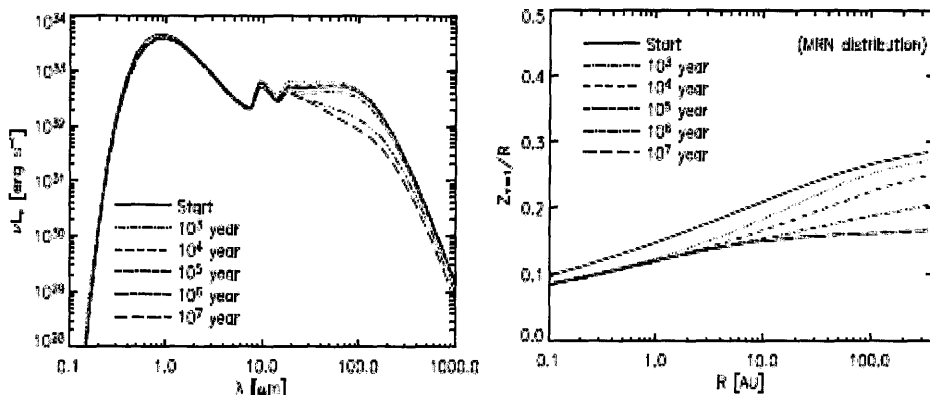


Figure 2.15: The SED and shape of the  $\tau = 1$  surface as a function of time for dust settling. The optical depth  $\tau$  is measured radially from the stellar surface outward at  $0.55\mu\text{m}$ . In these calculations, the MRN distribution is used (Mathis et al., 1977). Adapted from Dullemond & Dominik (2004a)

MRN distribution (Mathis et al., 1977) is used so that different grain sizes of dust have different scale heights as time goes on.

### 2.2.3 The effect of radiative disks on migration

As reviewed in § 2.1, considerations of planetary migration often assume disks to be isothermal in order for the calculations to be simplified. On the other hand, disks are irradiated by the stellar luminosity and heated by viscosity and their structure is determined by hydrostatic equilibrium, as reviewed in § 2.2.1. Furthermore, the structure of disk evolves with time (§ 2.2.2). Thus, the effect of radiative heatings on planetary migration is very important because the temperature of disks, which is determined mainly by the

stellar radiation, affects the resonant positions which control the torque. We review this in this subsection.

Menou & Goodman (2004) investigated the type I migration rate for low-mass protoplanets in steady state T Tauri accretion disks in which  $\alpha$ -prescription is used. In order to estimate accurately the background disk quantities, they found the steady state solutions to the radial equation for the conservation of mass, angular momentum and energy. The energy equation they used is similar to and simplified that of D'Alessio et al. (1998) because they assumed disks to consist of one-layer. In order to mimic three dimensional effects on the Lindblad torque, the gravitational potential of a protoplanet in 1D disk is expressed as

$$\Phi_p = -\frac{GM_p}{\sqrt{|r - r_p|^2 + h^2}}. \quad (2.27)$$

This results in the replacement of the Laplace coefficient, compared with Eq. (2.3),

$$b_{1/2}^m(\alpha_r) = \frac{2}{\pi} \int_0^\pi \frac{\cos m\theta d\theta}{\sqrt{1 - 2\alpha_r \cos \theta + \alpha_r^2 + (h/r)^2}}. \quad (2.28)$$

Technically this replacement of the Laplace coefficient makes the migration time increase relative to the 2D treatment. They found that the migration time with the stellar radiation is increased because disk parameters such as the optical thickness, temperature, and surface density are changed. They also found that the migration time is drastically changed at the opacity transition. This is because at this transition, disk parameters are changed rapidly, resulting in a large and sudden difference between the inner and outer torques.

Jang-Condell & Sasselov (2005), hereafter JS05 extended work of Menou & Goodman (2004) by considering the vertical thickness of disks. They also

treated the gravitational potential of planets self-consistently so that the density around a planet is compressed. This produces shadowing and illumination regions for the stellar radiation since disks are flared. In subsequent work, Jang-Condell & Sasselov (2003) and Jang-Condell & Sasselov (2004), hereafter JS03 and JS04, showed that the maximum temperature variation due to the presence of a protoplanet is 30% for planets whose mass is gap-opening threshold mass ( $\sim 35M_{\oplus}$ ). In their disk models, which are simplified models of D'Alessio et al. (1998), the heating source is the stellar radiation as well as viscous heating. In the torque calculations, they adapted the approach proposed by Ward (1988) and Artymowicz (1993a), rather than using a truly 3D torque. They found that the migration rate is reduced by up to a factor of two due to the temperature variation. This reduction is increased when larger planets with large orbital radii are considered. This is because the density distribution is more perturbed by more massive planets, resulting in the larger temperature variation. If planets with large orbital radii are considered, the effect of viscous heating becomes smaller. This causes the temperature variation to be refrained from washing out.

Numerical studies were undertaken by Klahr & Kley (2006) by using the 3D-radiation hydro code in which a flux-limited diffusion approximation is used for the radiation. They found that mean torque and migration rate is not significantly different from those of numerical simulations with isothermal disks for Jupiter mass planets. On the other hand, their fluctuations for short time intervals are larger, especially for high resolution results. This causes the sign of the torque to be reversed. Another interesting finding is that planets form pressure supported envelopes rather than an accretion circumplanetary

disk. The scale height of this envelop is about  $0.5R$ , which is beyond the approximation for the thin Keplerian disks.

Finally, Paardekooper & Mellema (2006) investigated radiatively heated disks for low mass planets ( $\sim 5M_{\oplus}$ ) by using a 3D radiation HD code. Flux-limited diffusion approximation is used for the radiation and viscous heating is neglected. They found for the case of high opacity, the migration is reversed. This arises from the large positive corotation torque, whereas the Lindblad torque is still negative. This is because the density behind the planet is reduced in order that the pressure equilibrium is maintained. For the case of low opacity, the results are similar to the one for isothermal disks.

## Chapter 3

### Computational techniques

Radiative transfer (RT) techniques are important for studying disks. As we reviewed in Chapter 2, it's impossible to fully solve the RT equation, which is dependent on frequency and the local structure of the disk. We used a 2D RT code called RADMC (Dullemond & Dominik, 2004b) which is based on the Monte Carlo (MC) method. MC methods are good for this study because they are independent of geometry although calculation time tends to be long to reach convergence, especially for high optical depth. We discuss the methods used in RADMC § 3.1.

Many radiative transfer codes as well as RADMC use a spherical coordinate system because it's efficient. The inner region, which is crucial for RT calculation, is highly resolved while the outer region which is less important is less resolved. On the other hand, a cylindrical coordinate system is preferred for dynamics in a disk because one uses the thin disk approximation to make the problem tractable. We are interested in the effect of the thermal structure of the disk on planetary migration so that we converted from spherical to cylindrical coordinates, which is not trivial since the path of a photon is curved by projection effects. We discuss this in § 3.2 and show our tests to

check the consistency of our coordinate transformation and convergence in § 3.3.

As we have seen, the tidal torque, which is the driving force of migration, is very sensitive to disk structure around planets, such as density and temperature. We therefore conducted intensive convergence tests for the calculation of tidal torque because grid size is quite important to adequately resolve these structures. We show our tests in § 3.4.

### 3.1 Radiative transfer : Monte Carlo method

RADMC is a versatile and highly reliable 2D RT code based on the MC technique in which the full RT is solved. The basic principle of the MC method is very simple. A photon is emitted from the source, and moves some distance. It's then either scattered or absorbed and emitted again into a new direction. The important thing is what happens in each step, which is determined by a probability called the cumulative distribution function. This cumulative distribution function,  $\psi(x)$  is determined by the fundamental principle:

$$\xi = \int_{x_i}^x P(x')dx' = \psi(x), \quad (3.1)$$

where  $x$  is a quantity we are interested in,  $P(x)$  is the probability function for  $x$ ,  $x_i$  is the lowest value, and  $\xi$  is a random number which covers the range from 0 to 1. Thus, the cumulative probability function must be normalized. Now we consider a few examples of the cumulative probability function.

1) Emission probability for isotropic radiation from a point source. The spherical coordinate system is used so that the direction of emission is characterized by  $\phi$  and  $\mu = \cos \theta$ . The cumulative probability function for  $\phi$  is

$$\xi = \frac{1}{2\pi} \int_0^\phi d\phi = \frac{\phi}{2\pi}, \quad (3.2)$$

where  $P(\psi)$  is 1 since radiation is isotropic and the normalization constant is  $2\pi$  since  $\phi$  is changed from 0 to  $2\pi$ . The cumulative probability function for  $\mu$  is

$$\xi = \frac{1}{2} \int_{-1}^\mu d\mu' = \frac{\mu - 1}{2}, \quad (3.3)$$

where  $P(\mu)$  is 1 again for the same reason given above, and the normalization constant is 2 in this case.

2) Emission probability of a point source toward a slab. Again we use a spherical coordinate system. The cumulative probability function for  $\phi$  is the same. The cumulative probability function for  $\mu$  is

$$\xi = 2 \int_0^\mu \mu' d\mu' = \mu^2, \quad (3.4)$$

where  $P(\mu) = \mu$  and the normalization constant is  $1/2$  since we just account for emission in the upper direction.

3) The optical depth a photon can move through at each step. When a photon moves through an optical depth  $\tau$ , the resultant intensity is reduced by  $e^{-\tau}$ . In other words, the probability that a photon can move an optical depth  $\tau$  without scattering or being absorbed is  $e^{-\tau}$ . Thus, the cumulative probability function for the optical depth a photon can move at each step is

$$\xi = \int_0^\tau e^{-\tau'} d\tau' = 1 - e^{-\tau}, \quad (3.5)$$

where the normalization constant is 1 since possible integration range is from 0 to  $\infty$ .

Thus, a photon is emitted from the central star, as determined by Eq. (3.2) and (3.3), and moves through the disk until the optical depth the photon takes reaches the value given by Eq. (3.5). Once the photon finishes moving through the optical depth determined by the cumulative probability function, it's either absorbed or scattered. Its fate is then determined by comparing a random number with the albedo at this point in which the albedo is calculated by the ratio of the scattering coefficient to the extinction coefficient. If the random number is bigger than the albedo, then this photon is absorbed. If not, it's scattered into a direction that is also determined by the cumulative probability function. Thus, a photon conducts a random walk in the disk until it escapes or is absorbed.

Absorption processes are crucial for determining the thermal structure of the disk. One approach is to treat the emission from the central star and from the disk separately. In other words, the disk emits at first where we guess the disk temperature should be (although the disk temperature must be in fact zero at first). Obviously, the emission from the disk is determined by the disk temperature which is determined by the total number of photons emitted from the star which are absorbed in the disk. Thus this approach needs iteration, which is a time consuming calculation. Furthermore, the total energy of the star and disk is not conserved until temperature converges since the disk possibly emits by itself without stellar luminosity. The other approach is not to distinguish the emission of the disk with the stellar emission as proposed by Lucy (1999). In this approach, a photon absorbed in the disk is forced to

re-emit immediately, based on a frequency distribution set which is determined beforehand. The frequency distribution set used by Lucy (1999) is not correct until the disk temperature converges. The stellar luminosity assumes local radiative equilibrium. Bjorkman & Wood (2001) modified the approach of Lucy (1999) to treat the frequency distribution set more accurately. In other words, this set is adjusted every time a photon is absorbed at this cell. We describe their method in more detail below because RADMC uses this method.

Bjorkman & Wood (2001) enforce local thermodynamic equilibrium (LTE) so that an absorbed energy is immediately re-emitted. In other words, the total energy of the star and disk is implicitly conserved. The temperature of a cell where a photon is absorbed is calculated by the balance between absorption and reemission. For the luminosity of the central star of  $L$ , and a total number of photons in frequency  $\nu$  of  $N_\nu$ , each photon emitted over a time interval  $\Delta t$  has energy

$$E_\nu = \frac{L\Delta t}{N_\nu}. \quad (3.6)$$

When the  $i$ th cell absorbs  $N_i$  photons in frequency  $\nu$ , the total energy absorbed is

$$E_i^{abs} = N_i E_\nu = \frac{N_i}{N_\nu} L \Delta t. \quad (3.7)$$

On the other hand, this absorbed energy  $E_i^{abs}$  must be re-emitted under the LTE assumption. The emitted energy over the same time interval  $\Delta t$  from  $i$ th cell is

$$E_i^{em} = 4\pi\Delta t \int d\nu \rho \kappa_\nu B_\nu(T) dV_i, \quad (3.8)$$

where  $\rho$  is density,  $\kappa_\nu$  is opacity at frequency  $\nu$ ,  $B_\nu(T)$  is the Planck function at temperature  $T$  since the thermal emissivity is  $j_\nu = \kappa_\nu \rho B_\nu(T)$ . By defining the Planck mean opacity  $\kappa_P = \int \kappa_\nu B_\nu / B d\nu$  and  $B = \sigma T^4 / \pi$ , the re-emitted energy is

$$E_i^{em} = 4\pi \Delta t \kappa_P(T_i) B(T_i) m_i, \quad (3.9)$$

where  $m_i = \rho dV_i$  is mass in  $i$ th cell. Thus temperature in this cell is determined by Eq. (3.7) and (3.9);

$$\sigma T_i^4 = \frac{N_i L}{4N_\nu \kappa_P(T_i) m_i}. \quad (3.10)$$

Note that  $\kappa_P$  in Eq. (3.10) is dependent on  $T_i$ , so we need to iterate to solve Eq. (3.10). In order to do so efficiently,  $\kappa_P$  is pre-tabulated over wide range of temperature and interpolated.

Thus, once a photon is absorbed in a cell, this energy is re-emitted immediately by LTE by following Lucy (1999). Although this approach is sound since the total energy is conserved, the emission from the disk is incorrect if disk temperature is increased when another photon is absorbed. This is because the thermal emissivity before absorbing another photon is  $j'_\nu = \kappa_\nu B_\nu(T - \Delta T)$ , where  $\Delta T$  is increment of temperature due to absorption. On the other hand, the emissivity after absorption is  $j_\nu = \kappa_\nu B_\nu(T)$ . Thus, the difference of emissivity due to absorption is

$$\Delta j_\nu = j_\nu - j'_\nu = \kappa_\nu [B_\nu(T_i) - B_\nu(T_i - \Delta T)], \quad (3.11)$$

which is the shaded region shown in Fig 3.1

When we take a large enough number of photons,  $\Delta T$  is considered to be relatively small, so

$$\Delta j_\nu = \kappa_\nu \Delta T \frac{dB_\nu}{dT}. \quad (3.12)$$

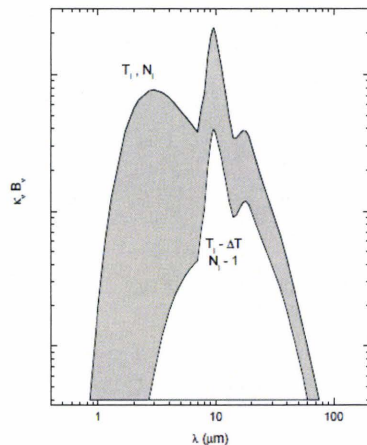


Figure 3.1: Temperature correction frequency distribution. Adapted from Bjorkman & Wood (2001)

In order to correct the disk temperature, all we have to do is to emit a photon determined by Eq. (3.12) because  $\Delta T$  and  $dB_\nu/dT$  are always positive since  $B_\nu$  is a monotonically increasing function. In other words, we emit photons which are determined by the following probability function in order to correct the disk temperature;

$$\frac{dP_i}{d\nu} = \frac{\kappa_\nu}{K} \left( \frac{dB_\nu}{dT} \right)_{T=T_i}, \quad (3.13)$$

where  $K = \int_0^\infty \kappa_\nu (dB_\nu/dT) d\nu$  is the normalization constant.

Thus, in the approach of Lucy (1999) and modified by Bjorkman & Wood (2001), stellar luminosity is implicitly conserved since the absorbed photons are reradiated immediately due to the LTE assumption. An iteration is not needed since the temperature of the disk is always corrected as prescribed by the probability function Eq. (3.13). RADMC uses this method to speed up calculations and avoid the iteration process.

## 3.2 Coordinate systems in RADMC

RADMC is a 2D RT code written in spherical coordinates. MC simulations in 2D will obviously need far less time to run than in 3D because fewer photons are needed. On the other hand, a 2D treatment provides us with another complexity - the path of a photon. A photon moves on a straight line in medium of constant refractive index in 3D, while it's curved in the same medium in 2D due to the projection effect. Fig 3.2 shows the projection of a path of a photon, which is a straight line in three dimensional coordinate system, into the cylindrical and Cartesian coordinate system on the left and right panel, respectively. The path of a photon is curved in the cylindrical system  $(r, z, \Phi)$  whereas it is still straight in the Cartesian system  $(x, y, z)$ . We want to consider the dynamical aspect of planets in which a cylindrical coordinate system is preferred. Thus, we must do a coordinate transformation in RADMC from a spherical to a cylindrical coordinate system. This requires that we modify almost all parts of RADMC, except for the part that calculates disk temperature. First of all, we review the path of a photon in spherical coordinates, and then review our implementation in cylindrical coordinates.

### 3.2.1 Spherical coordinates

We refer to the standard spherical coordinate system  $(R, \Theta, \Phi)$ . Since we assume axisymmetry, any dependency on  $\Phi$  is neglected. In order to describe the path of a photon, we need to set up a local coordinate system. We need two angles to characterize the direction of the photon;  $\theta$  and  $\phi$ . The north pole in this local system is chosen so that it corresponds to radial direction  $R$ .  $\theta$  is measured from this north pole toward mid-plane of this local system. Thus  $\theta$

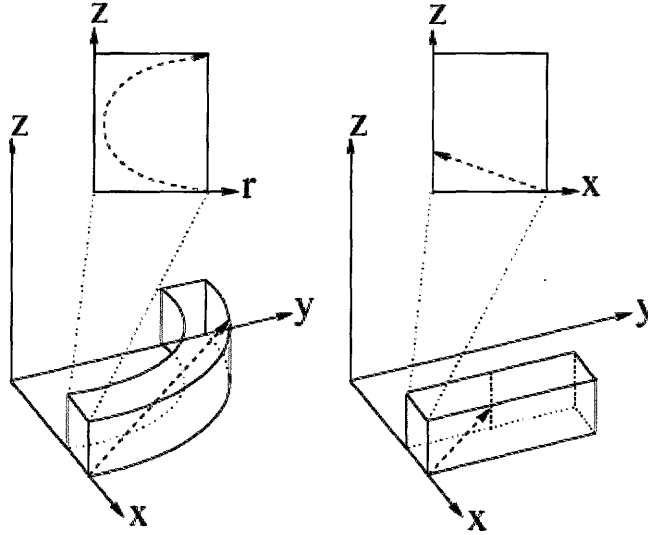


Figure 3.2: Projection of a path of a photon into cylindrical and Cartesian coordinate system on the left and right panel, respectively. Adapted from Van Noort et al. (2002).

follows a photon as it moves toward the north pole or the opposite direction.  $\phi$  is measured from a parallel line to the mid-plane of the global system. Thus the direction of a photon at  $P = (R, \Theta)$  is determined by local system  $(\theta, \phi)$ .

The RT equation in the 2D spherical coordinate system is

$$\frac{dI_\nu}{ds} = \mu \frac{\partial I_\nu}{\partial R} - \frac{\sqrt{1-\mu^2}}{R} \sin \phi \frac{\partial I_\nu}{\partial \Theta} + \frac{1-\mu^2}{R} \frac{\partial I_\nu}{\partial \nu} - \frac{\cos \phi}{\tan \Theta} \frac{\sqrt{1-\mu^2}}{R} \frac{\partial I_\nu}{\partial \phi} = \alpha_\nu (S_\nu - I_\nu), \quad (3.14)$$

where  $I_\nu$  is the specific intensity at frequency  $\nu$ ,  $ds$  is the displacement of the path of the photon, and  $\mu = \cos \theta$  (Dullemond & Turolla, 2000). Thus, the variation of  $R$ ,  $\Theta$ ,  $\mu$  and  $\phi$  along the path of the photon are

$$\frac{dR}{ds} = \mu \quad (3.15)$$

$$\frac{d\Theta}{ds} = -\frac{\sqrt{1-\mu^2}}{R} \sin \phi \quad (3.16)$$

$$\frac{d\mu}{ds} = \frac{1-\mu^2}{R} \quad (3.17)$$

$$\frac{d\phi}{ds} = -\frac{\sqrt{1-\mu^2}}{R} \frac{\cos \phi}{\tan \Theta}. \quad (3.18)$$

The solutions of these equations above are

$$R^2 = b^2 + s^2 \quad (3.19)$$

$$\cos \Theta = \frac{z_0 + s \cos \Theta_\infty}{\sqrt{b^2 + s^2}} \quad (3.20)$$

$$\mu = \frac{s}{\sqrt{b^2 + s^2}} \quad (3.21)$$

$$\sin \phi = \frac{b^2 \cos \Theta_\infty - z_0 s}{b \sqrt{b^2 + s^2 - (z_0 + s \cos \Theta_\infty)^2}}, \quad (3.22)$$

where  $b$  is the impact parameter of the ray with respect to the origin,  $z_0$  is the height from the mid-plane of the closest point to the north pole of global system, and  $\Theta_\infty$  is the inclination at infinity.

The solutions above are used to follow the path of photon in MC simulations (Dullemond & Turolla, 2000). Once the photon reaches  $P = (R_k, \Theta_l)$  and the direction of photon is determined by the random number as  $(\mu, \phi) = (\mu_i, \phi_j)$ , the constants are

$$b^2 = R_k(1 - \mu_i^2) \quad (3.23)$$

$$\cos \Theta_\infty = \mu_i \cos \Theta_l + \sqrt{1 - \mu_i^2} \sin \Theta_l \sin \Theta_j \quad (3.24)$$

$$z_0 = R_k \left[ (1 - \mu_i^2) \cos \Theta_l - \mu_i \sqrt{1 - \mu_i^2} \sin \Theta_l \sin \phi_j \right]. \quad (3.25)$$

Combining these constants with the solutions, we can describe the path of the photon. RADMC is a non grid-based code, but all physical quantities such as the density and temperature are defined on the grid, so the next point

it will reach is determined by the intersection between grid points and these solutions. Eq. (3.19) and (3.20) gives us two possible values for  $s$ , and possible grid points the photon can take are  $R_{k-1}$ ,  $R_k$ , and  $R_{k+1}$  ( $R_{k-1} < R_k < R_{k+1}$ ), and  $\Theta_{l-1}$ ,  $\Theta_l$ , and  $\Theta_{l+1}$  ( $\Theta_{l-1} < \Theta_l < \Theta_{l+1}$ ). Thus, the total number of possible values of  $s$  is 12 and are given by

$$s_n = \pm \sqrt{R_K^2 - b^2} \quad (3.26)$$

$$s_m = \frac{1}{\cos^2 \Theta_\infty - \cos^2 \Theta_L} \left[ -z_0 \cos \Theta_\infty \pm \cos \Theta_L \sqrt{b^2 (\cos^2 \Theta_\infty - \cos^2 \Theta_L) + z_0^2} \right], \quad (3.27)$$

where  $K = \{k-1, k, k+1\}$ ,  $n = 1, 2, \dots, 6$ ,  $L = \{l-1, l, l+1\}$ , and  $m = 7, 8, \dots, 12$ .

Finally, we can determine the actual path the photon takes by choosing the minimum of the absolute value of  $s$ , but not  $s_P$  since  $s_P$  means the photon stays at the same position as  $P = (R_k, \Theta_l)$ . Thus, once a photon is emitted from the star or disk, it moves in the disk following Eq. (3.26) and (3.27) until the distance reaches the optical depth determined by a random number beforehand, as we reviewed § 3.1.

### 3.2.2 Cylindrical coordinates

We're now in a position to review our transformation of the coordinate system. We refer to the standard cylindrical system  $(r, z, \Phi)$ . Again, we assume axisymmetry so that any dependence on  $\Phi$  is dropped out. In order to describe the path of a photon, we use the local system  $\theta$  and  $\phi$ . The main differences are the following. The north pole is aligned with z-axis of global system. Consequently,  $\theta$  is measured from this axis toward mid-plane and follows the photon

as it moves upward or downward compared with the mid-plane.  $\phi$  is measured from the local x-axis which is parallel to the global x-axis. The  $\phi$  coordinate tracks the photon as it moves forward or backward compared with the local coordinate system. Thus, the roles of  $\theta$  and  $\phi$  in cylindrical coordinates are exchanged compared with those in spherical coordinates ( $\theta$  in sphericals determines its propagating forward, and  $\phi$  determines its propagating upward). Then, we repeat this procedure once we find the solutions of the RT equation.

The RT equation in the cylindrical system is

$$\frac{dI_\nu}{ds} = \sqrt{1 - \mu^2} \sin \phi \frac{\partial I_\nu}{\partial r} + \mu \frac{\partial I_\nu}{\partial z} + \frac{\sqrt{1 - \mu^2} \cos \phi}{r} \frac{\partial I_\nu}{\partial \phi}, \quad (3.28)$$

where the definitions of each variable are the same as before (Liu et al., 2006).

Thus, the variation of  $r$ ,  $z$ ,  $\mu = \cos \theta$ , and  $\phi$  along the path of the photon are

$$\frac{dr}{ds} = \sqrt{1 - \mu^2} \sin \phi \quad (3.29)$$

$$\frac{dz}{ds} = \mu \quad (3.30)$$

$$\frac{d\mu}{ds} = 0 \quad (3.31)$$

$$\frac{d\phi}{ds} = \frac{\sqrt{1 - \mu^2} \cos \phi}{r} \quad (3.32)$$

The solutions of these equations above are

$$r^2 = (1 - \mu^2)s^2 + b^2 \quad (3.33)$$

$$z = \mu_0 s + z_0 \quad (3.34)$$

$$\mu_0 = \mu \quad (3.35)$$

$$\sin \phi = \frac{\sqrt{1 - \mu^2}}{r} s, \quad (3.36)$$

where  $b$  is the impact parameter of the ray with respect to the origin,  $z_0$  is the height from the mid-plane of the closest point to the north pole of global system.

We use these solutions to follow the path of the photon. When the photon is located at  $P = (r_k, z_l)$  and its new direction is determined as  $(\mu, \phi) = (\mu_i, \phi_j)$ , these constants are

$$b^2 = r_k^2 \cos^2 \phi_j \quad (3.37)$$

$$z_0 = z_l - \frac{\mu_0}{\sqrt{1 - \mu_0^2}} r_k \sin \phi_j. \quad (3.38)$$

Again, the possible paths  $s$  that the photon takes are given by Eq. (3.33) and (3.34). In this case, the number of possible solutions of Eq. (3.33) is two and that of Eq. (3.34) is only one. Taking into account grid points  $(r, z) = (r_K, z_L)$  where  $K = \{k - 1, k, k + 1\}$  and  $L = \{l - 1, l, l + 1\}$ , the total possible paths are 9 and given by

$$s_n = \pm \sqrt{\frac{r_K^2 - b^2}{1 - \mu^2}} \quad (3.39)$$

$$s_m = \frac{z_L - z_0}{\mu_0}, \quad (3.40)$$

where  $n = 1, 2, \dots, 6$  and  $m = 7, 8, 9$ . The actual path it takes is determined so that the absolute value of  $s$  is a minimum and not the same as  $s_P$  which is the path evaluated at  $P = (r_k, z_l)$ .

Thus, the motion of a photon is determined by Eq. (3.39) and (3.40) once the optical depth it traverses is determined. Thus the motion of photons in the disk is now prescribed as we reviewed § 3.1.

### 3.3 Convergence tests for RADMC

Numerical simulation is one of the most important tools to study subjects that are not analytically tractable. There are two ways to test codes; comparison with analytical solutions, and comparison with already tested and reliable codes. Although there are many benchmark tests for hydrodynamic simulations, those for RT are rare. First of all, we couldn't take an analytical approach to multi-dimensional RT problem although analytical solutions can be derived for simple geometries and under the assumption of gray opacity, which are far from realistic astronomical objects. Secondly, variables in RT such as position, density, and opacity which depend on frequency are numerous. These variables in the multi-dimensional case are increased by the power of  $n$ , where  $n$  is the degree of dimension. Thus, it's very difficult to define the benchmark tests for the RT problem. The only practical way to test codes is to compare solutions of well-defined problems produced by several independently developed codes. Pascucci et al. (2004) defines the benchmark test for RT codes following this approach. In § 3.3.1, we review the benchmark tests for original RADMC. Then we check our modification by using the same benchmark test in § 3.3.2. Finally, we discuss the dust size distribution and disk temperature in § 3.3.3.

#### 3.3.1 Benchmark tests for RT codes

We define the benchmark test by following Pascucci et al. (2004). Before going into detail on the disk setup, we summarize the RT problem for the benchmark test. The aim of the RT problem is to specify the specific intensity,

$I_\nu(\vec{x}, \vec{n})$  by solving RT equation, where  $\nu$  is frequency,  $\vec{x}$  is the position of  $I_\nu$ , and  $\vec{n}$  is the direction of  $I_\nu$ . The RT equation is

$$\begin{aligned}
\vec{n} \cdot \nabla_{\vec{x}} I_\nu(\vec{x}, \vec{n}) &= - [\kappa^{abs}(\nu, \vec{x}) + \kappa^{sca}(\nu, \vec{x})] I_\nu(\vec{x}, \vec{n}) \\
&+ \kappa^{abs}(\nu, \vec{x}) B_\nu(T(\vec{x})) \\
&+ \frac{\kappa^{sca}(\nu, \vec{x})}{4\pi} \int_{\Omega} d\Omega' p(\nu, \vec{n}, \vec{n}') I_\nu(\vec{x}, \vec{n}') \\
&+ E_\nu(\vec{x}, \vec{n}), \tag{3.41}
\end{aligned}$$

where  $\kappa^{abs}(\nu, \vec{x})$  and  $\kappa^{sca}(\nu, \vec{x})$  are the absorption and scattering coefficients of the position at  $\vec{x}$ , respectively;  $B_\nu$  is the Planck function and  $T$  is the temperature;  $p(\nu, \vec{n}, \vec{n}')$  represents the probability that radiation is scattered from the direction  $\vec{n}'$  to  $\vec{n}$ , and  $\Omega$  is the solid angle; and  $E_\nu$  denotes all internal radiation sources arising from viscous heating or cosmic rays. Eq. (3.41) states that the rate of change of the specific intensity is determined by the loss of intensity due to extinction of dust, the gain due to thermal emission of dust, the gain due to scattered intensity, and the gain due to local emission. For simplicity, one dust component of a specific size is considered.

One of the difficulties in solving Eq. (3.41) is that the coupling between the radiation field and the dust temperature requires us to consider the balance between absorption and reradiation simultaneously

$$\int_0^\infty d\nu Q_\nu^{abs} B_\nu(T(\vec{x})) = \int_0^\infty Q_\nu^{abs} \frac{1}{4\pi} \int_{\Omega} d\Omega' I_\nu(\vec{x}, \vec{n}'), \tag{3.42}$$

where  $Q_\nu^{abs}$  is the absorption efficiency factor. Thus, in order to calculate the specific intensity and temperature self-consistently, Eq. (3.41) and (3.42) must be solved simultaneously, which is quite difficult.

We are now in a position to define the disk configuration for our benchmark test. We consider a circumstellar disk with an inner cavity free of dust that

is illuminated by a central star. The star is assumed to be a point-like source and its radiation is treated as black body radiation. This test disk consists of spherical silicate grains whose radius is  $0.12\mu m$  and density is  $3.6g/cm^3$ . The size of the disk is from 1 AU to 1000 AU. The density structure is similar to that of CG97;

$$\rho(r, z) = \rho_0 \times f_1(r) \times f_2(z/h(r)) \quad (3.43)$$

$$f_1(r) = (r/r_d)^{-1.0} \quad (3.44)$$

$$f_2(z, r) = \exp \left[ -\frac{\pi}{4} \left( \frac{z}{h(r)} \right)^2 \right] \quad (3.45)$$

$$h(r) = z_d \left( \frac{r}{r_d} \right)^{1.125}, \quad (3.46)$$

where  $r = \sqrt{x^2 + y^2}$ ,  $z$  is the distance from the mid-plane,  $r_d$  is half of the disk outer radius, ie,  $r_d = R_{out}/2$ , and  $z_d$  is one fourth of  $r_d$ , ie,  $z_d = r_d/4 = R_{out}/8$ . We consider four values of visual ( $\lambda = 550nm$ ) optical depth, that is,  $\tau_\nu = 0.1, 1, 10, 100$ . The optical depth is measured along the mid-plane. We change the total mass of disk from  $1.1 \times 10^{-7}M_\odot$  to  $1.1 \times 10^{-4}M_\odot$  so that we can consider four different optical depths from 0.1 to 100. In other words,  $\rho_0$  is changed by varying the total mass of disk. Table 3.1 shows the parameters used in the benchmark tests and Table 3.2 summarizes the resolution and the number of photons used in each code.

Pascucci et al. (2004) compare the results produced by five different independently developed codes including RADMC to check the validity of each codes. We briefly summarize these codes except for RADMC.

MC3D is a 3D continuum RT code based on the MC method developed by Wolf et al. (1998). It solves the RT problem self-consistently. It can sim-

Table 3.1: Summary of parameters used in the benchmark tests

Symbol	Meaning	Value
$M_*$	Stellar mass	$1M_\odot$
$R_*$	Stellar radius	$1R_\odot$
$T_*$	Stellar effective temperature	$5800K$
$R_{out}$	Outer disk radius	1000 AU
$R_{in}$	Inner disk radius	1 AU
$r_d$	Characteristic disk radius	500 AU
$z_d$	Disk height	125 AU
$a$	Grain radius	$0.12\mu m$
$\rho_g$	Grain density	$3.6g/cm^3$
$\tau_\nu$	Optical depth at $550nm$	0.1, 1, 10, 100
$\beta$	the power of total disk mass <sup>1</sup>	7, 6, 5, 4

<sup>1</sup> The total disk mass is defined as  $1.1 \times 10^{-\beta} M_\odot$ 

Table 3.2: Summary of resolution and the number of photons used by each code

Code name	$\#r$	$\Delta r$ [AU]	$\#\theta$	$\Delta\theta$ [°]	$\# Phot[\times 10^6]$	Optical depth
MC3D	55	0.03-141	121	1.5	244	0.1,1,10
	$10^3$	0.07-4.1	121	1.5	244	100
MCTRANSF	48	0.17-125	40	4.5	1000	0.1
	48	0.17-125	40	4.5	800	1
	46	0.18-130	46	2.8-5.3	1000	10
	46	0.18-130	46	2.8-5.3	500	100
RADICAL	60	0.03-116	62	1.6-8.3		0.1-100
RADMC	60	0.03-116	62	1.6-8.3	10	0.1-100
STEINRAY	61	0.12-109	61	1.3		0.1-100

ulate dust temperature in arbitrary dust and electron configurations and produce observational quantiles such as spectral energy distribution, wavelength-dependent images and polarization map.

MCTRANSF is a multidimensional continuum RT code by using the MC method developed by Lopez et al. (1995). Currently, only spherical symmetric (1D) and axisymmetric (2D) modes are developed, but the extension to 3D is possible and straightforward.

RADICAL is a grid-based 2D RT code developed by Dullemond & Turolla (2000) that solves the RT equation directly instead of following a photon. Thus, it uses special methods, called the Lambda Iteration and the Variable Eddington Tensor to make results converge faster. RADICAL has these two modes and puts the right modes in the right place.

STEINRAY is also a grid-based full 3D continuum RT code developed by Steinacker et al. (1996). The temperature distribution is calculated using an improved version of the Lambda Iteration, called the Accelerated Lambda Iteration between the RT equation and the local balance equation.

We are now in a position to compare results produced by these five different codes for the four optical depth cases, 0.1, 1, 10, 100. Although it's very difficult to solve RT equation analytically, we can solve RT equation under some reasonable assumption for the completely optical thin case, ie  $\tau_\nu = 0.1$ .

In this case, we can neglect re-emission from dust since dust mass is too small to absorb the stellar luminosity. Thus, the scattering effect dominates the extinction. We assume that the internal radiation  $E_\nu = 0$  and the scattering is isotropic. So Eq. (3.41) becomes

$$\vec{n} \cdot \nabla_{\vec{x}} I_\nu(\vec{x}, \vec{n}) = - [\kappa^{abs}(\nu, \vec{x}) + \kappa^{sca}(\nu, \vec{x})] I_\nu(\vec{x}, \vec{n}) \quad (3.47)$$

and its solution is (stellar radiation is treated as black body radiation),

$$I_\nu(R, \theta) = \left(\frac{R_*}{R}\right)^2 B_\nu(T_*) \exp\left[-\pi a^2(Q_\nu^{abs} + Q_\nu^{sca}) \int_0^R dR' \rho(R', \theta)\right] \equiv B_\nu^e(T_*, R, \theta), \quad (3.48)$$

where  $\vec{n}$  is dropped since isotropic scattering and  $\vec{x} = (R, \theta)$  in spherical system, where  $\theta$  is measured from the mid-plane, not the north pole. Thus, the solution of Eq. (3.41) shows that  $I_\nu$  is reduced by  $(R_*/R)^2$  with the distance from the star and by an exponential term due to extinction. Combining with Eq. (3.42), the disk temperature is given by

$$\int_{\nu_{min}}^{\nu_{max}} d\nu B_\nu [T_d(R, \theta)] Q_\nu^{abs} = \frac{1}{4} \int_{\nu_{min}}^{\nu_{max}} d\nu B_\nu^e(T_*, R, \theta) Q_\nu^{abs}, \quad (3.49)$$

where  $T_d$  is the disk temperature. Eq. (3.49) shows that the disk temperature structure is spherical (as expected) in the completely optical thin limit since the dependence of  $\theta$  in this limit is negligible.

In order to calculate the flux density  $F_\nu$  at a distance equal to stellar radius, all we have to do is to integrate the power emitted by each grain over the whole disk. The power emitted by one grain is given by

$$P_\nu^g(R, \theta) = 4\pi a^2 Q_\nu^{abs} B_\nu [T_d(R, \theta)], \quad (3.50)$$

and the flux density is given by

$$F_\nu = \frac{2\pi}{4\pi R_*^2} \int_{R_{in}}^{R_{out}} dR' \int_0^\pi d\theta' P_\nu^g(R', \theta') \rho(R', \theta') R'^2 \cos \theta', \quad (3.51)$$

where  $2\pi$  comes from the integration for azimuthal angle.

We now summarize the temperature distributions found for four different optical depth cases. All codes succeed in reproducing the temperature structure correctly. For the most optical thin case ( $\tau_\nu = 0.1$ ), the difference between

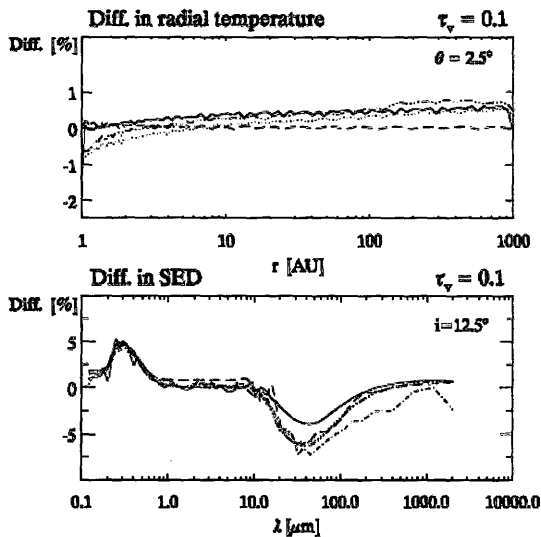


Figure 3.3: Difference of temperature and SED for the most optical thin case ( $\tau_v = 0.1$ ). The upper panel shows that the temperature difference between all codes and analytical calculation at  $\theta = 2.5^\circ$ . The lower panel shows that the SED difference at the inclination  $i = 12.5^\circ$ . For both panels, the solid line denotes the difference of MC3D, the dot-dashed line is that of MCTRANSF, the dash-dot-dot-dotted line is that of RADCIAL, the dotted line is that of RADMC, and the dashed line is that of STEINRAY. Analytical solution is chosen as the reference. Adapted by Pascucci et al. (2004).

computational results and analytical results is less than 1% at  $\theta = 2.5^\circ$ , where the effect of scattering is important (See Fig 3.3). From here, the difference is calculated below

$$diff = \frac{a - b}{b} \times 100[\%], \quad (3.52)$$

where  $a$  is the quantity in interest, and  $b$  is the reference solution. In this case, analytical solution is taken as the reference solution.

For optical depth  $\tau_v = 1$  and  $\tau_v = 10$ , temperature difference is less than 10%. For the most optically thick case, the RT calculation becomes difficult

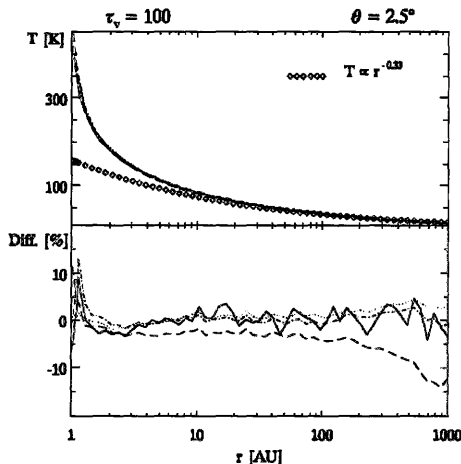


Figure 3.4: Radial temperature and its difference for the most optical thick case ( $\tau_v = 100$ ). The upper panel shows that the radial temperature at  $\theta = 2.5^\circ$ . The diamonds denotes semi-analytical solution for the optically thin regime at long wavelengths, the solid line denotes the temperature of MC3D, the dot-dashed line is that of MCTRANSF, the dash-dot-dot-dotted line is that of RADICAL, the dotted line is that of RADMC, and the dashed line is that of STEINRAY. The lower panel shows its difference. RADICAL is chosen as the reference solution. The solid line denotes the difference of MC3D, the dot-dashed line is that of MCTRANSF, the dotted line is that of RADMC, and the dashed line is that of STEINRAY. Adapted from Pascucci et al. (2004).

and large deviations are expected. Fig. 3.4 and 3.5 show the difference of temperature for radial cut at  $\theta = 2.5^\circ$  and vertical cut at  $r = 2$  AU, respectively. The temperature structure for the optically thin regime at long wavelengths is also plotted in Fig. 3.4 (diamonds). In this regime, the temperature can be approximated as  $T(r) \propto r^{-2/(4+\beta)}$ , where  $\beta$  is the index of the dust absorption coefficient at low frequencies ( $\kappa_\nu^{abs} \propto \nu^\beta$ ). For the dust used here,  $\beta = 2$ . The upper panel of Fig. 3.4 shows that temperature of the outer part of disk is approximated as optically thin at long wavelengths (as expected)

The temperature in the inner region deviates from this approximation since optical depth in this region is high and short wavelengths are important. The upper panel of Fig. 3.5 shows that there is the turnover of disk from optically thick to thin around  $19^\circ$ . Both the temperature structure of the numerical approach and semi-analytical approach suddenly drop at this turnover point. Note that semi-analytical solution represented by diamonds in Fig. 3.5 is derived from Eq. (3.49). The temperature produced in the numerical simulation is always higher than that of semi-analytical case. This is because re-emission of dust due to absorption is not negligible at the inner part of the disk and because the re-emission increases the scattering effect at outer part of the disk. Consequently, the numerical temperature is higher than the analytical one.

The lower panels of Fig. 3.4 and 3.5 show the difference in temperature, where RADICAL is chosen as the reference solution. The difference in the radial temperature is less than 5% from 1.2 AU to 200 AU. The difference in the vertical temperature is less than 2.5% from  $40^\circ$  to  $10^\circ$ .

We now summarize the SED for four different optical depth cases and three disk inclinations,  $i = 12.5^\circ$  (face-on),  $i = 42.5^\circ$ , and  $i = 77.5^\circ$  (edge-on). We focus on the percentage of difference since the difference of SED for each codes is too small to distinguish with each other. For the most optically thin case, the results produced by all codes are compared with the analytical solution (see Fig. 3.3) as well as with each other, where RADICAL is the reference solution (See Fig 3.6). The lower panel of Fig. 3.3 shows that the difference between all codes is always less than 8%, but there are large deviations around 0.3 and  $40\mu m$ . The SED calculated by all codes in the region  $0.2 - 0.7\mu m$  is higher and in the region  $10 - 200\mu m$  is lower than that of

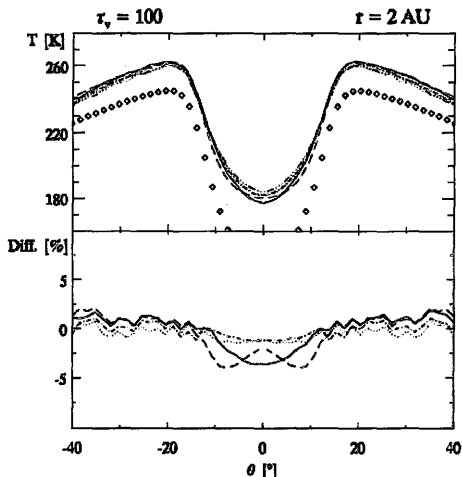


Figure 3.5: Vertical temperature and its difference for the most optical thick case ( $\tau_v = 100$ ). The upper panel shows that the vertical temperature at  $r = 2$  AU. The lower panel shows its difference. The definition of all lines is the same as Fig. 3.4 except for the diamonds. In this case, the diamonds are calculated by Eq. (3.49). The reference solution is that of RADICAL. Adapted from Pascucci et al. (2004).

the semi-analytical calculation. This is because the scattering efficiency factor of the dust (silicate) used in this benchmark test is high around  $0.2 - 0.7 \mu m$ . On the other hand, the analytical solution includes only the scattering term in the extinction (See Eq. (3.47)). That's why the semi-analytical approach predicts the lower emission around  $0.3 \mu m$ . At the same time, the scattered photons produce lower emission around  $40 \mu m$ . Thus, the difference between SED computed by all codes and the semi-analytical solution is due to the dust properties. Fig. 3.6 shows the difference between all codes, where RADICAL is taken as the reference code. The agreements are better than 2% for all three inclination angles except for MCREANSF.

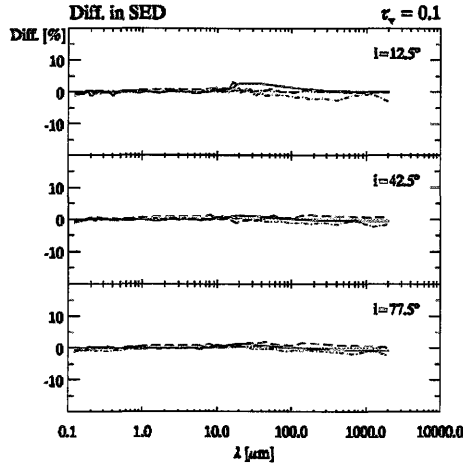


Figure 3.6: Percentage of difference in the SED between codes for optical depth ( $\tau_v = 0.1$ ). The upper panel shows the difference at the inclination  $i = 12.5^\circ$  (face-on). The middle panel shows that at  $i = 42.5^\circ$ . The lower panel shows that at  $i = 77.5^\circ$ . The reference solution is that of RADICAL. For all panels, the definition of all lines is the same as Fig. 3.4. Adapted from Pascucci et al. (2004)

The deviation is expected to be large as the optical depth is increased since it's difficult to solve the RT equation. Pascucci et al. (2004) found that the difference at  $i = 12.5^\circ$  and  $i = 42.5^\circ$  is always smaller than that at  $i = 77.5^\circ$ . For the optical depth  $\tau_v = 1$ , the deviation is less than 9% although the difference at edge-on is larger than those at the other two cases. For the optical depths  $\tau_v = 10$  and 100, the deviation at  $i = 12.5^\circ$  and  $42.5^\circ$  is less than 10% (See Fig. 3.7). For the almost edge-on disk, the shorter wavelength region (around  $0.2\mu m$  and  $10\mu m$ ) presents some difficulties for all codes. In the region around  $0.2\mu m$ , the scattering is dominant and it's very sensitive

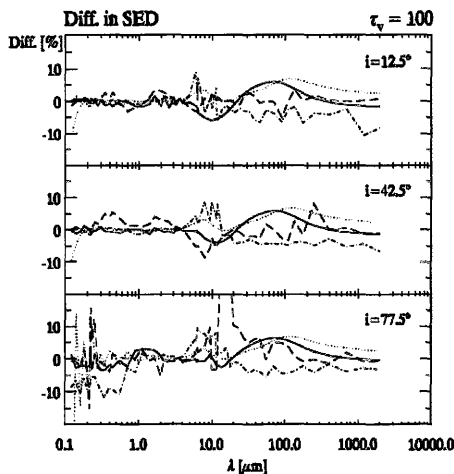


Figure 3.7: Percentage of difference in the SED between codes for optical depth ( $\tau_v = 100$ ). The upper panel shows the difference at the inclination  $i = 12.5^\circ$  (face-on). The middle panel shows that at  $i = 42.5^\circ$ . The lower panel shows that at  $i = 77.5^\circ$ . The reference solution is that of RADICAL. For all panels, the definition of all lines is the same as Fig. 3.4. Adapted from Pascucci et al. (2004)

to resolution. This also causes deviations in the IR regime. Eventually, the overall agreement for all codes is better than 10%.

Thus, RADMC proves to be a very reliable 2D RT code for arbitrary inclination and optical depth.

### 3.3.2 Results of our benchmark tests for modified RADMC

Our test of the code written in cylindrical coordinates follows Pascucci et al. (2004) again. We use the same resolution in the code and same disk configuration (See table 3.1 and 3.2). We compare results by modified RADMC only with the original RADMC for all cases ( $\tau_v = 0.1 - 100$ ) since we know

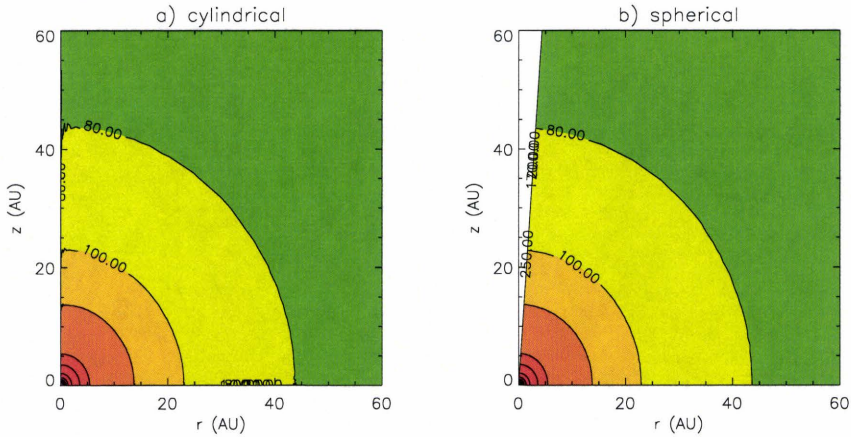


Figure 3.8: Two dimensional temperature distribution for the most optical thin case ( $\tau_v = 0.1$ ) produced by the modified and original RADMC on the plot a) and b), respectively. The color and contour denotes the temperature in Kelvin. The temperature is decreased from red to green.

that the original RADMC is a reliable RT code. In this case, we considered only the temperature behavior because another ray-tracing code is used to produce SEDs in RADMC.

For the most optically thin case ( $\tau_v = 0.1$ ), we plot the two dimensional temperature distribution in order to make sure that it has a spherical shape, as predicted by the analytical solution. Fig. 3.8 a) and b) shows the temperature structure produced by the modified and original RADMC, respectively. Both plots clearly show the spherical shape of temperature and are almost identical. Fig. 3.9 a) shows the difference between them as a function of disk radius and its difference at  $\theta = 2.5^\circ$  on the upper and lower panel, respectively. The difference is calculated by Eq. (3.52), and the solution of the original RADMC is chosen as the reference. For the upper panel of a), temperature produced

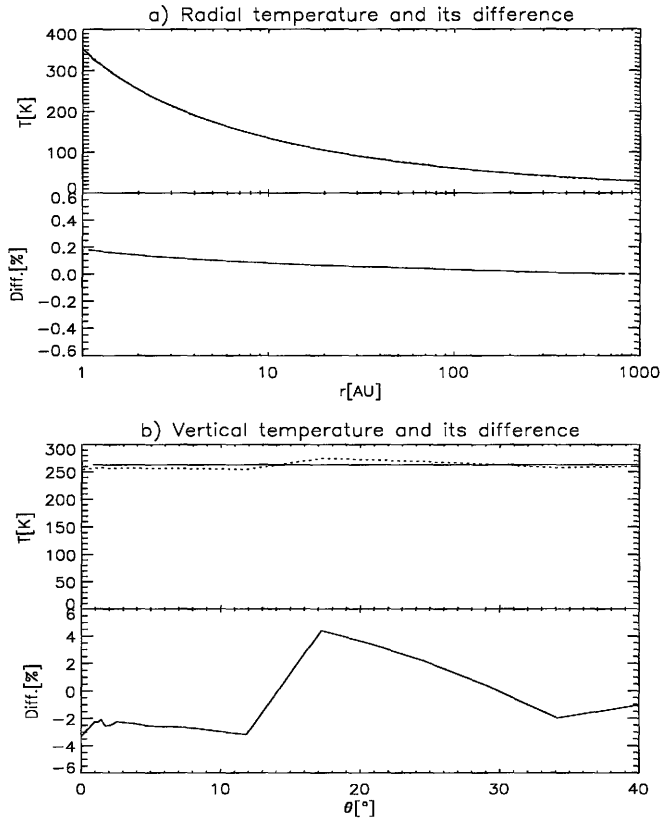


Figure 3.9: Radial temperature and its difference and vertical temperature and its difference for the most optical thin case ( $\tau_v = 0.1$ ) at  $\theta = 2.5^\circ$  on panel a) and at  $r = 2$  AU on panel b), respectively. For the upper panel on both plots a) and b), the solid line denotes the temperature produced by the original RADMC, and the dotted line is for the modified RADMC. For the lower panel, the difference between them is shown. The reference solution is produced by the original RADMC.

by the original RADMC is denoted by the solid line, and that of the modified RADMC is by the dotted line although its difference is too small to distinguish. For the lower panel, the difference between them is less than 0.2% although the largest difference occurs at the inner part. Fig. 3.9 b) shows the difference

between them for vertical temperature and its difference at  $r = 2$  AU on the upper and lower panel, respectively. The definition of lines on the upper panel of b) is the same as 3.9 a). As shown in the lower panel, the difference with them is less than 5%.

For the case of the optical depths of  $\tau_o = 1, 10,$  and  $100,$  the behavior of the radial and vertical difference between cylindrical and spherical cases are similar although the temperature behavior itself is different for each optical depth. The largest difference for the radial temperature is less than 0.2% at the inner part, and that for the vertical temperature is less than 5%. This proves that our modification is properly implemented in RADMC and that the modified RADMC is as reliable a 2D RT code as the original RADMC.

### 3.3.3 Results of our convergence tests of dust size distribution & disk temperature

The size distribution of dust is very important in order to calculate the disk temperature, as reviewed in § 2.2.2. Although it's desirable to take into account all sizes of grains, numerical limitations prevent us from doing this. Also, another complexity arises from the fact that the disk scale height for each grain size is different due to dust settling that is the outcome of the grain growth. Thus, a practical approach is to pick several grain sizes. If the temperature structure of the disk is convergent for a finite number of grain sizes, we can conclude this sampling is enough to represent the effect of the full dust size distribution. In this subsection, we show that our sampling results in convergence for disks around very low mass star (VLMS) such as M dwarfs, and disks around classical T Tauri star (CTTS). Our procedure is to start

with two sizes of dust, and then add another size of dust one by one, until the temperature structure of the disk converges.

Our models for dust compositions and distribution and for disks around VLMS and CTTS are the following. For the dust composition, we use the model of Pollack et al. (1994), as shown in Table 3.3. For the dust distribution, we use the MRN distribution (Mathis et al., 1977) although it's discretized for the reason mentioned above. Thus, Eq. (2.22) is modified below;

$$n(a) = n_0 \sum_{a_i=a_{min}}^{a_{max}} a^p \delta(a_i - a), \quad (3.53)$$

where  $n_0$  is a constant independent of grain size  $a$ ,  $\delta(a)$  is the Dirac's delta function,  $a_i$  is the grain size we pick up,  $a_{min}$  is the minimum size of dust, and  $a_{max}$  is the maximum size of dust. We set  $a_{min} = 0.01\mu m$  and  $a_{max} = 1000\mu m$  (Chi-ang et al., 2001). In order to calculate the opacity of each dust grain, we use the Mie theory in which real and imaginary refractive indices of dust and parameters such as the abundance, density, and grain size of dust are used. We take the laboratory data of refractive indices and density of each composition from the web site; [http://www.mpia.de/homes/henning/Dust\\_opacities/Opacities/opacities.html](http://www.mpia.de/homes/henning/Dust_opacities/Opacities/opacities.html). Additional grain sizes are added into the domain from  $0.01\mu m$  to  $1000\mu m$  in equally spaced logarithmic intervals. The data on grain sizes of dust that we used is summarized in Table 3.4.

The total mass of dust  $M_{dust}$  is

$$M_{dust} = \sum_{a_i} \int da \frac{4}{3} \pi \rho_i n(a), \quad (3.54)$$

Table 3.3: The dust composition and abundance in our model

Composition	Abundance	Density [ $g/cm^3$ ]
Olivine	2.6	3.49
Orthopyroxene	0.8	3.4
Iron	0.1	7.87
Troilite	0.8	4.83
Organics	4.1	1.5
Waterice	5.6	0.92

where  $\rho_i$  is the density of grain size  $a_i$ . In this calculation, dust is assumed to be spherical. Moreover, we assume  $\rho_i = \rho_0$  to be independent of grain size and to be calculated using Table 3.3. Thus,  $M_{dust}$  is

$$M_{dust} = \frac{4}{3}\pi n_0 \rho_0 \sum_{a_i} a_i^{3+p}. \quad (3.55)$$

The mass ratio of a grain size  $a_i$  is

$$r_{mass} = \frac{m_i}{M_{dust}} = \frac{a_i^{3+p}}{\sum_i a_i^{3+p}}, \quad (3.56)$$

where  $m_i$  is the total dust mass of grain size  $a_i$ . We set  $p = -2.5$ . This is because  $m_i$  must be a increasing function of  $a$ , and because D'Alessio et al. (2001) showed that the difference between mass absorption coefficient with  $p = -2.5$  and  $p = -3.5$  is not significant. The mass ratio of each grain sizes of dust we used is listed in Table 3.4.

For disk models, we assume that vertical hydrostatic equilibrium is satisfied (e.g. D'Alessio et al., 1998; Dullemond & Dominik, 2004b)

$$\frac{\partial P}{\partial z} = -\rho \frac{GM_*}{R^3} z, \quad (3.57)$$

Table 3.4: Summary of grain sizes and mass ratio of dust used in VLMS and CTTS

4 grain sizes		5 grain sizes		6 grain sizes		7 grain sizes	
$a_i$ [ $\mu\text{m}$ ]	$r_{mass}$						
0.01	0.0031	0.01	0.0028	0.01	0.0022	0.01	0.0020
0.46	0.0095	0.17	0.0087	0.1	0.0068	0.086	0.0050
21.5	0.0303	3.16	0.0276	1	0.0216	0.46	0.0132
1000	0.9571	56.2	0.0873	10	0.0684	3.16	0.0347
		1000	0.8735	100	0.2164	21.5	0.0905
				1000	0.6844	146.8	0.2367
						10000	0.6177

$a_i$  is the grain size of dust, and  $r_{mass}$  is mass ratio (See Eq. (3.56)). Note that grain sizes are chosen so that the grain size domain from 0.01 to 1000  $\mu\text{m}$  is logarithmically equal spaced.

where  $P$  is gas pressure,  $M_*$  is the stellar mass,  $R = \sqrt{r^2 + z^2}$ , and  $r = \sqrt{x^2 + y^2}$ . Under the thin approximation ( $R \simeq r$ ) and the assumption that  $\Sigma = \Sigma_0 r^q$ , the integration of Eq. (3.57) becomes

$$\rho = \frac{\Sigma}{\sqrt{2\pi}h} \exp\left(-\frac{z^2}{2h^2}\right), \quad (3.58)$$

where  $c = P/\rho$  and  $h = c/\Omega_{Kep} = h_0(r/r_0)^\beta$  are used. Parameters for disks around VLMS and CTTS are summarized at Table 3.5 (CG97; Scholz et al., 2007). Note that we use either  $M_d$  or  $\Sigma_0$  in order to calculate the density distribution.

For disks around VLMS, we found that five sizes of dust is enough to represent the temperature distribution in the disk. Fig 3.10 a), b), and c) shows the density and temperature in the disk for four, five and six sizes of dust grains, respectively. In these plots, the color represents the density (density scale is shown in color bar above each figure and density unit is  $g/cm^3$ )

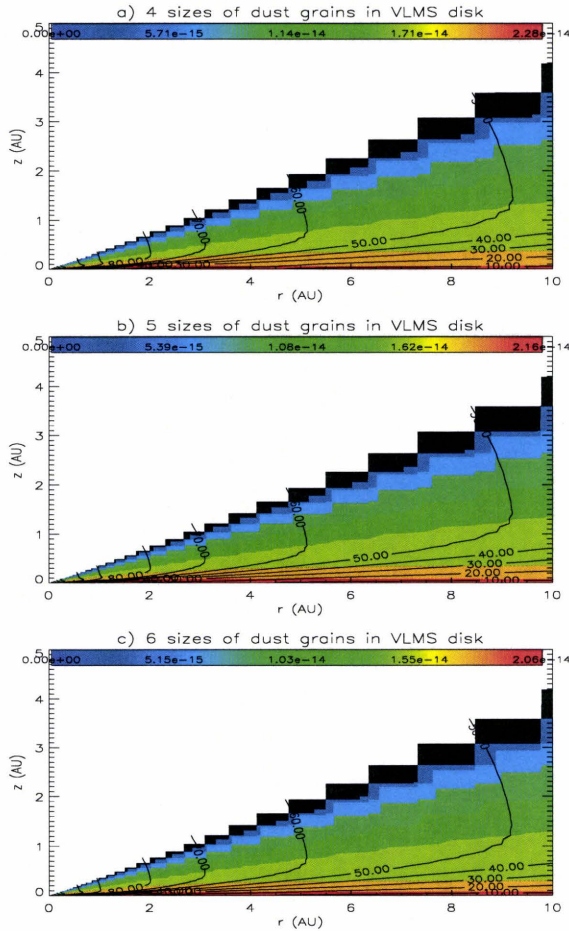


Figure 3.10: The density and temperature plots of the disk around VLMS. The color denotes the density (density scale is shown in color bar above each figure and density unit is  $g/cm^3$ ) and the contours are for the temperature in Kelvin. a) four sizes of dust grains, b) five sizes of dust grains, and c) six sizes of dust grains are included.

) and the contours track the temperature. Comparing them, we conclude that the five sizes of dust grains are clearly sufficient to treat disk temperature to excellent accuracy.

Table 3.5: Summary of parameters used in VLMS and CTTS

Symbol	Meaning	Value of VLMS	Value of CTTS
$M_*$	Stellar mass	$0.1M_\odot$	$0.5M_\odot$
$R_*$	Stellar radius	$0.4R_\odot$	$2R_\odot$
$T_*$	Stellar effective temperature	$2850K$	$4000K$
$R_{out}$	Outer disk radius	100 AU	200 AU
$R_{in}$	Inner disk radius	$6R_*$	0.02 AU
$r_o$	Characteristic disk radius	$R_*$	1 AU
$h_o$	Characteristic disk height	$0.02r_o$	$0.04r_o$
$M_d^1$	The total disk mass	$4.5 \times 10^{-4}M_\odot$	-
$\Sigma_0$	Characteristic surface density	-	$1000[g/cm^3]$
$q$	the power of surface density	-1	-1.5
$\beta$	the power of scale height	1.1	1.1
	gas-to-dust ratio	100	100

<sup>1</sup>  $M_d$  means the sum of gas and dust

In order to analyze these models quantitatively, we plot the radial temperature distribution and its difference between different number of dust grains at  $z = 0.2$  AU in Fig 3.11 a). For the upper panel, the dotted line denotes the temperature for four sizes, the solid line is for five sizes of grains, and the dashed line is for six sizes. For the lower panel, the solid line represents the difference between four and five sizes of grains, and the dotted line is for that between six and five sizes of grains, where the difference is calculated by Eq. (3.52), and the reference solution is that for the case that five sizes are included. The maximum difference is about 15%. Interestingly, the temperature in the outer part of the disk is slightly increased by including more grain sizes. Fig 3.11 b) shows the vertical temperature and its difference between different number of dust grains at  $r = 8$  AU. For both panels, the definition of lines is the same as that of Fig. 3.11 a). The maximum difference is about

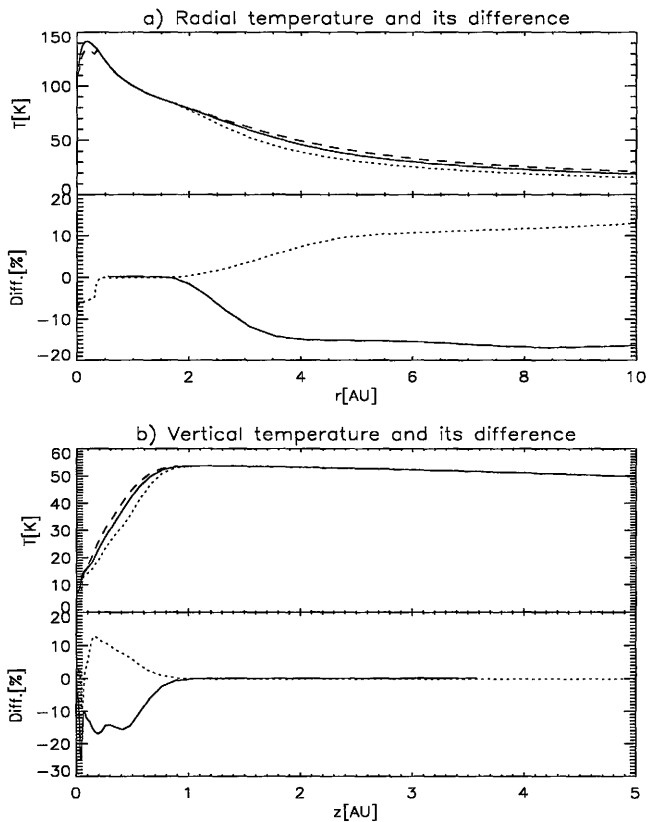


Figure 3.11: Radial temperature and its difference and vertical temperature and its difference for the disk around VLMS at  $z = 0.2$  AU on panel a) and at  $r = 8$  AU on panel b), respectively. For the upper panel on both plots a) and b), the dotted line denotes the temperature for four sizes of dust, the solid line is for five sizes of dust grains, and the dashed line is for six sizes of dust. For the lower panel, the difference between four and five sizes of grains is represented by the solid line, and that between five and six sizes of grains is by the dotted line. The reference solution is that for five sizes.

25%. Both plots show that the difference is reduced to less than 15% as more grain sizes are considered. Thus, we conclude that the five sizes of dust grains are sufficient to model the disk temperature.

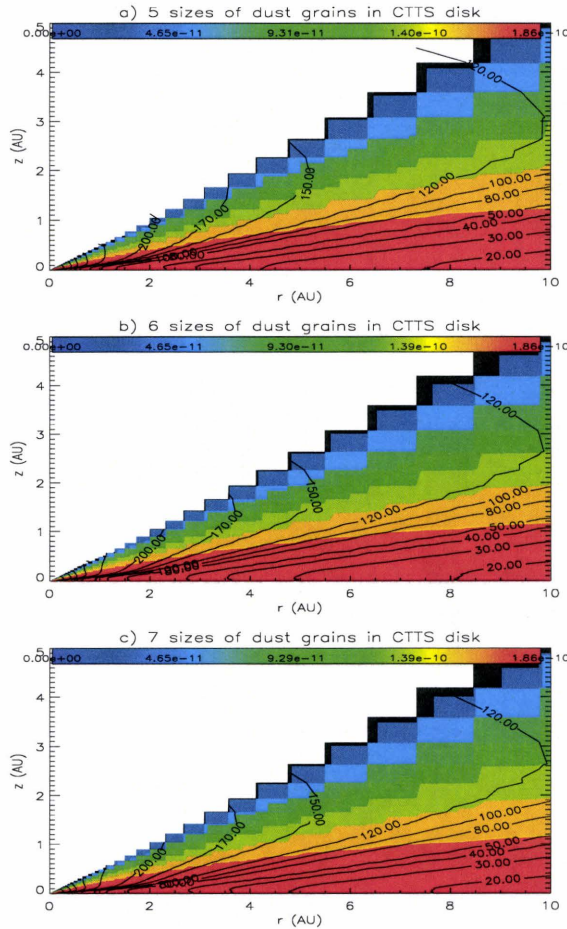


Figure 3.12: The density and temperature plot of the disk around CTTS. The color denotes the density (density scale is shown in color bar above each figure and density unit is  $g/cm^3$ ) and the contours are for temperature in Kelvin. a) five sizes of dust grains, b) six sizes of dust grains, and c) seven sizes of dust grains are included.

For disks around CTTS, we find that six sizes of dust are enough to represent temperature in the disk. Fig 3.12 a), b) and c) shows the density and temperature in the disk for five, six and seven sizes of dust grains, respectively.

In these plots, the color again represents the density (density scale is shown in color bar above each figure and density unit is  $g/cm^3$ ) and the contours track temperature. Comparing them, we conclude that the six sizes of dust grains is sufficient to accurately compute the disk temperature distribution.

We again plot the radial temperature and its difference between different number of dust grains at  $z = 0.2$  AU in Fig 3.13 a). For the upper panel, the dotted line denotes the temperature for five sizes, the solid line is for six sizes of grains, and the dashed line is for seven sizes. For the lower panel, the solid line represents the difference between five and six sizes of grains, and the dotted line is for that between six and seven sizes of grains, where the difference is calculated by Eq. (3.52), and the reference solution is that for the case that six sizes are included. The maximum difference is less than 30%. Again, the temperature around  $r = 2$  AU is increased with the total number of grain sizes. Fig 3.13 b) shows the vertical temperature and its difference between different number of dust grains at  $r = 8$  AU. For both panels, the definition of lines is the same as that of Fig. 3.13 a). The maximum difference is about 15%. For both plots, the maximum difference arises at the transition region in which the temperature contour changes from curved, and sphere-like line to straight lines. This implies that the optical depth at these point changes from thin to thick since for the optical thin case, the temperature contour has a spherical shape. In other words, the self-shadowing effect beyond these regions is important. Thus, the difference becomes the maximum at these region since these regions are determined by dust properties. We conclude that six sizes of dust grains are sufficient to model the disk temperature.

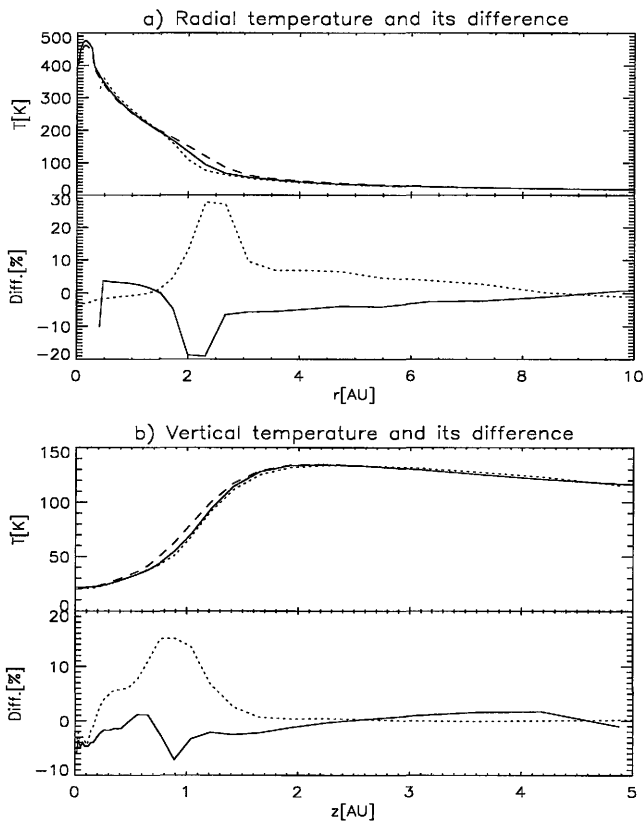


Figure 3.13: Radial temperature and its difference and vertical temperature and its difference for the disk around CTTS at  $z = 0.2$  AU on panel a) and  $r = 8$  AU on panel b), respectively. For the upper panel on both plots a) and b), the dotted line denotes the temperature for five sizes of dust, the solid line is for six sizes of dust grains, and the dashed line is for seven sizes of dust. For the lower panel, the difference between five and six sizes of grains is represented by solid line, and that between six and seven sizes of grains is by dotted line. The reference solution is that for six sizes.

### 3.4 Results of our convergence tests for the Lindblad torque calculation

The torque calculations require that we perform a convergence study since the tidal torque is very sensitive to physical quantities such as disk density and

temperature. As reviewed in § 2.1.1 and 2.1.2, torques at both the Lindblad and corotation resonances are effectively determined in a region whose distance from a planet is about a disk scale height  $h$ . On the other hand, the disk structure defined by temperature and density is determined by the whole disk region which is the order of a few hundred AU. Thus, we are required to use a proper grid system in order to estimate the tidal torque and the resultant migration rate and time. In this section, we undertake a convergence study for the Lindblad torque that is the dominant torque for the migration of relatively low mass planets.

One of the easiest ways to calculate torques accurately is to use finer grids over the whole disk region. We could not take this approach, however, because the finer the grid is, the longer the computational time of RADMC becomes. This can cause one run to require more than a month to compute a single disk model. We overcame this difficulty by using a finer scale grid for the region within several disk scale heights of the planet. For the region beyond, a coarser logarithmically spaced grid is employed. This is discussed in § 3.4.4. Also, we cut down the disk size in order to reduce the computational time. We can take this approach if the density and temperature of the smaller disk is identical with those of a larger disk. This is mentioned in § 3.4.1. In § 3.4.2, we discuss our methodology and disk models. In § 3.4.3, we summarize the analytical formula we use. In § 3.4, we focus on disks around VLMS. We mention the value of parameters, otherwise, we use parameters for the VLMS listed in Table 3.5.

### 3.4.1 Results of test: the reduction of disk size

We cut down the disk size from 100 AU to 10 AU in order to reduce the computational time. This corresponds to the replacement of  $R_{out} = 100$  AU with 10 AU. At the same time,  $M_d$  is adjusted consistently. More specially,  $M_d$  is decreased by ten in this case. This disk reduction is harmless for temperature calculation of disk around VLMS. This is because photons are emitted from the central star and basically propagate from the inner to the outer region. In other words, the backward emission of dust due to scattering and re-emission is relatively small so that the density and temperature of smaller disk is almost identical with those of larger disk.

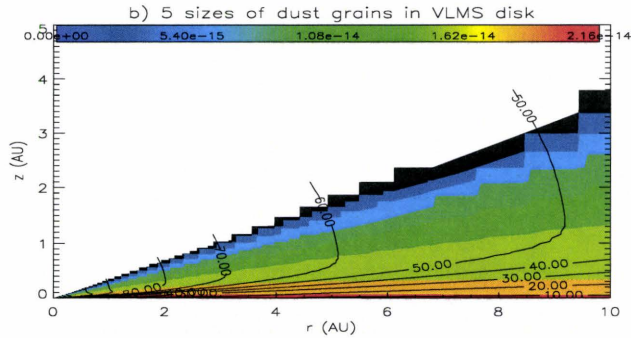


Figure 3.14: The density and temperature plot of the small disk around VLMS (10 AU). The color denotes the density (density scale is shown in color bar above each figure and density unit is  $g/cm^3$ ) and the contours are for temperature in Kelvin. Compare with Fig 3.10 b)

Fig. 3.14 shows the density and temperature of this small disk whose whole size is 10 AU. Compared with Fig. 3.10 b), the behavior of temperature is very similar to that of full disk although temperature of a small disk is slightly lower than that of a large disk.

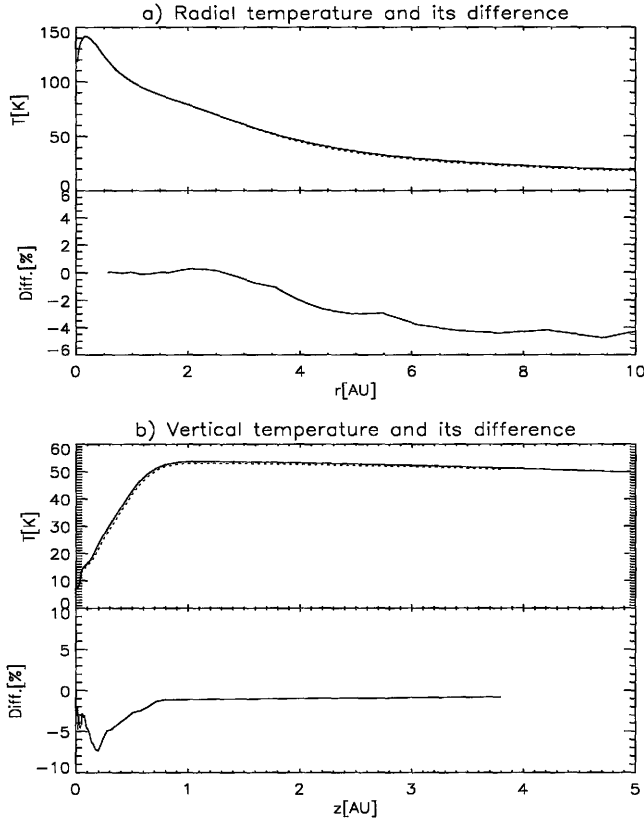


Figure 3.15: Radial temperature and its difference and vertical temperature and its difference for the disk around VLMS at  $z = 0.2$  AU on panel a) and  $r = 8$  AU on panel b). For the upper panel on both plots a) and b), the solid line denotes temperature for a large disk ( $R_{out} = 100$  AU), and the dotted line is for a small disk ( $R_{out} = 10$  AU). For the lower panel, the difference between large and small disks is shown. The reference solution is that for a large disk.

In order to investigate the difference quantitatively, the radial and vertical temperature and its difference are shown in Fig. 3.15 a) and b), respectively. The difference is calculated by Eq. (3.52), and the reference solution is that for a large disk. For the upper panel of both figures, the solid line denotes

temperature for a large disk and the dotted line is a small disk on the upper panel. The difference between large and small disks is plotted on the lower panel. The maximum difference for the radial temperature at  $z = 0.2$  is about 5% and that for vertical temperature at  $r = 8$  AU is about 8%.

Thus, the reduction of the disk size does not produce a large effect on the temperature although the backward emission of dust due to scattering and re-emission is not completely negligible.

### 3.4.2 Methodology & Disk model

We first discuss our methodology to calculate the tidal torque in radiatively heated disks by the star. Our prime aim is to estimate accurately the resonant positions which depend only on the disk temperature. This enables us to calculate the torque accurately. In order to calculate the disk temperature by means of Monte Carlo methods, we start with an initial disk density model. We set up the initial disk model by assuming vertical hydrostatic equilibrium with scale height modeling as power-law. We then calculate the resulting disk temperature that arises by exposing this initial disk to irradiation by the central star. The scale height that results is now different from the initial one. The next step is to calculate the new density structure by using the new disk temperature structure. By iterating this calculation, we self-consistently calculate the temperature and density structure to arbitrary accuracy.

Although this temperature and density structure, which are derived self-consistently, provide us with an accurate torque, this is a very time-consuming calculation. Thus, we found that we could stop our calculations after the first iteration. In other words, we use the new temperature which is calculated

from the initial disk model. For the density distribution, we use the initial disk model. This works because the difference of resultant torque between the initial density setup and the new density structure (calculated by the new temperature) is not large, as we will show below. Another reason why we use the initial disk model for the density in this thesis is that torque calculations are time-consuming. Also in the literature where the torque in the radiatively heated disk is considered, the density of the initial disk model has been usually used (e.g. Menou & Goodman, 2004, JS05) although for the temperature, the new one is used. In our future journal publication, we will use the new density structure in order to calculate the torque. We have checked that our conclusion is physically very similar even if we use the initial rather than new density structure. In following calculations, we use the new temperature structure, and the density structure of the initial disk model unless otherwise stated.

We adopt the disk models of JS03 and JS04 as our initial disk model. The effect of the gravitational force of the planets on the density distribution is taken into account properly in those models. By adding the planet's gravity into the equation for hydrostatic equilibrium, Eq. (3.57) is modified below;

$$\frac{\partial P}{\partial z} = -\rho \frac{GM_*}{R^3} z - \rho \frac{GM_p}{R_p^3} z, \quad (3.59)$$

where  $R_p = \sqrt{(r - r_p)^2 + z^2}$  and  $r = \sqrt{x^2 + y^2}$ . By integrating this equation, and using  $dc_s/dz = 0$  (since the initial disk model is assumed isothermal), the density is

$$\rho = \rho_0 \exp \left( -\frac{z^2}{2h^2} + \frac{\mu}{h^2} \left[ \frac{r}{\sqrt{(r - r_p)^2 + z^2}} - \frac{r}{|r - r_p|} \right] \right), \quad (3.60)$$

where  $\mu = M_p/M_*$  and the normalization constant  $\rho_0$  is chosen so that the density at  $z = 0$  corresponds to the unperturbed density (See Eq. (3.58)).

In this model, the density deviation due to the gravity of the planet will also cause a density redistribution in the radial direction. Our calculations show that the radial pressure gradient perturbation due to a planet is only 10% relative to the gravitational force at the Hill radius. Well inside the Hill radius, however, this can rise to 150% effect ie -the planet puts the gas into non-Keplerian motion. This is not unexpected since the planet's gravity must dominate within this region, but it may lead to interesting dynamical effects. In calculating the tidal torque, we use the new temperature structure, which varies in the vertical direction.

Our disk parameters are listed in Table 3.5 in § 3.3.3 with the replacement of  $R_{out} = 100$  AU with 10 AU.

### 3.4.3 Torque calculations

For our torque calculations, we adopted the approach proposed by Ward (1988) and Artymowicz (1993a) as well as JS05. The main difference with JS05 is that we consider the torque density (rather than the torque) for each layer. The Lindblad torque density of a layer at disk scale height  $z$  is

$$\frac{d}{dz} \left( \frac{dT^L}{dr}(r, z) \right) = \text{sgn}(r - r_p) \frac{2\mu^2 \rho r_p^4 \Omega_p^4}{r(1 + 4\xi^2)\kappa^2} m^4 \psi^2, \quad (3.61)$$

where

$$\psi = \frac{\pi}{2} \left[ -\varepsilon \frac{\alpha}{m} \frac{db_{1/2}^m(\alpha_r, \zeta)}{d\alpha_r} + 2\sqrt{1 + \xi^2} b_{1/2}^m(\alpha_r, \zeta) \right], \quad (3.62)$$

and

$$b_{1/2}^m(\alpha_r, \zeta) = \frac{2}{\pi} \int_0^\pi \frac{\cos m\theta d\theta}{\sqrt{1 - 2\alpha_r \cos \theta + \alpha_r^2 + \zeta^2}}. \quad (3.63)$$

Thus, the main difference with the 2D torque density is the replacement of  $\Sigma$  with  $\rho$  and the modification of forcing function and the Laplace coefficient,

which are dependent on  $\zeta = z/r$  (See Eq. (2.11), (2.12), and (2.3)). The torque density is normalized by

$$\Gamma_0 = \rho\mu a^4 \Omega_p^4. \quad (3.64)$$

The total torque is calculated by

$$T^L = \int_{-\infty}^{\infty} dz \int_0^{\infty} dr \frac{d}{dz} \left( \frac{dT^L}{dr}(r, z) \right). \quad (3.65)$$

The migration time is estimated by

$$T_{mag} = \frac{M_p \sqrt{GM_* r_p}}{T^L}. \quad (3.66)$$

#### 3.4.4 Results of tests of the torque at Lindblad resonances

As reviewed in § 2.1.1, the dominant contribution to the torque at Lindblad resonances arises from contributions at a distance  $h$  from a planet (See Fig. 2.2). Thus, the grid immediately around the planet is highly resolved, whereas the other region is coarsely resolved. As already discussed, our finer grid uses an equally spaced mesh and the coarse grid uses a logarithmically spaced mesh. In order to show convergence, we reduced the radial width of the region around the planet from  $10h$  to  $6h$  and  $4h$ , in each of which 65 grids are assigned. As a whole, 150 grids are aligned over 10 AU of the disk. For the vertical direction, logarithmic grids are used so that the total number grids is also 150. This is because the region above and below of the planet, which is important for torque calculations, is highly resolved by using the logarithmic grid.

We also devised a scheme to re-calculate only the density after temperature calculations are completed. In this approach, temperature is first calculated

based on the density distribution of the disk by using the grid mentioned above. The density structure of the disk is then re-calculated by using the grid which is several times finer. This treatment enables us to reduce the computational time by a factor of ten or so. This approach is useful only if temperature behavior is not so sensitive to the grid system. Although we did not perform runs by using a finer grid than that mentioned above, we can show that the grid mentioned above is fine enough to calculate temperature.

We also interpolated our results for the density and the resultant temperature within the Hill radius (JS05). This is because in linear theory, the region within the Hill radius is considered to be infinitesimally small, and as reviewed in § 2.1.2, the contribution of this region to torque is very large (D'Angelo et al., 2002). We used parameters for VLMS listed in Table 3.5 with the replacement of  $R_{out} = 100$  AU with 10 AU.

We found that the migration time is convergent when  $6h$  is resolved by 65 grids and the density is re-calculated by planet-centered grids that are six times finer than  $150 \times 150$  grids. Fig 3.16 shows the migration time of  $1 M_{\oplus}$  planet in the disk around VLMS for each grid system. The dot-dashed line represents the migration rate in which  $10h$  is resolved by 65 grids, the solid line is for the migration rate in which  $6h$  is resolved by 65 grids, the dashed line is for the migration rate in which  $4h$  is resolved by 65 grids. In each case, the density is re-calculated by six times finer grid. Obviously, it shows convergence.

We also wanted to make sure that the grid used by the re-calculation of density, after the temperature calculation is valid. The migration time in which  $6h$  is resolved by 65 grids and the density is re-calculated in a grid that

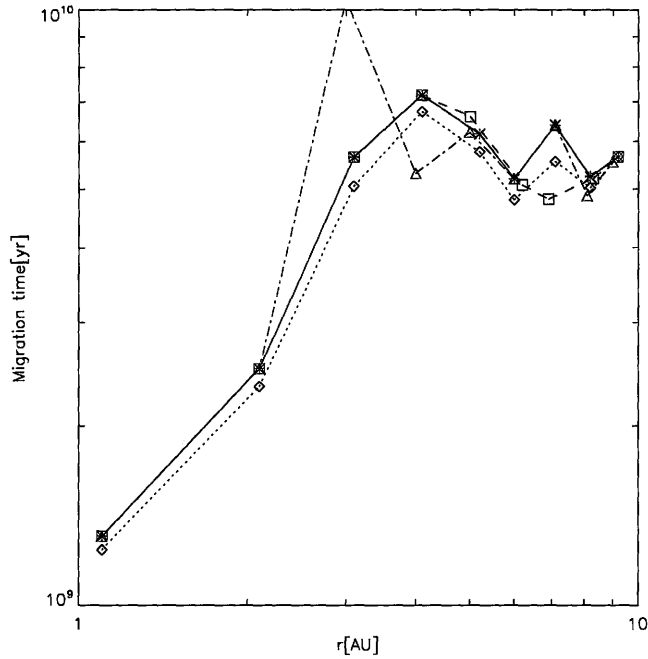


Figure 3.16: The Migration time of a  $1 M_{\oplus}$  planet in the disk around VLMS. The dot-dashed line denotes the migration rate in which  $10h$  is resolved by 65 grids and the density is re-calculated by six times finer grid. The solid line is for the migration rate in which  $6h$  is resolved by 65 grids and the density is re-calculated by six times finer grid. The dashed line is for the migration rate in which  $4h$  is resolved by 65 grids and the density is re-calculated by six times finer grid. The dotted line denotes the migration rate in which  $6h$  is resolved by 65 grids and the density is re-calculated by nine times finer grid.

is nine times finer. This is shown by the dotted line in the same figure. This also shows convergence. Henceforth, we will use 65 grids that are distributed over  $6h$  around the planet, wherein the density is re-calculated by a grid that is six times finer than the grids used in temperature calculations.

Now we discuss the effect of using the new density structure to calculate the tidal torque and migration time. After the first step, we know the new tem-

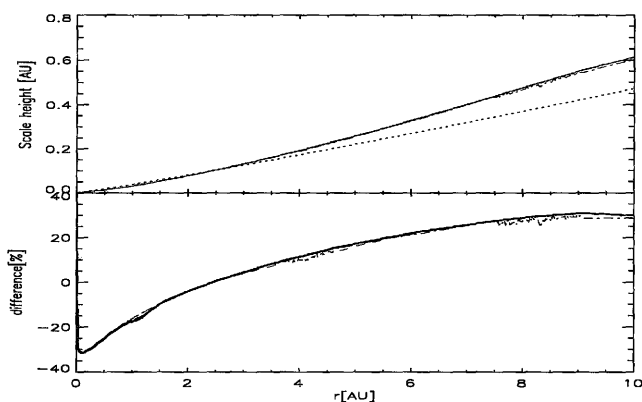


Figure 3.17: The scale height and its difference for a  $1 M_{\oplus}$  planet at the various orbital radii. The dotted line denotes the scale height of the initial temperature in the upper panel. For both panels, the black solid line denotes the case of 2 AU, the blue dashed line is for 4 AU, and the red dot-dashed line is for 8 AU. For the lower panel, the scale height of the initial temperature is chosen as the reference solution.

perature structure in disks so that we can calculate the new density structure. In order to do so, we use the new scale height. The dominant contribution to the torque arises from the mid-plane to the distance of scale height, as shown in Fig. 4.9 to 4.12. It's sufficient to consider the modification of density due to the new temperature from the mid-plane to the distance of scale height. Thus, we use the new scale height derived by the new temperature in order to calculate the new density structure.

Fig. 3.17 shows the scale height and its difference for a  $1 M_{\oplus}$  planet at the various orbital radii. The dotted line denotes the scale height of the initial temperature in the upper panel. For both panels, the black solid line denotes the case of 2 AU, the blue dashed line is for 4 AU, and the red dot-dashed line is for 8 AU. For the lower panel, the scale height of the initial temperature is

chosen as the reference solution and the difference is calculated by Eq.(3.52). As shown in the upper panel, the new scale height is increased as a function of radius compared with the initial one. In the lower panel, the difference between the initial and new scale height is shown. Although about 30% difference is not small, this effect on migration is not large, as shown later.

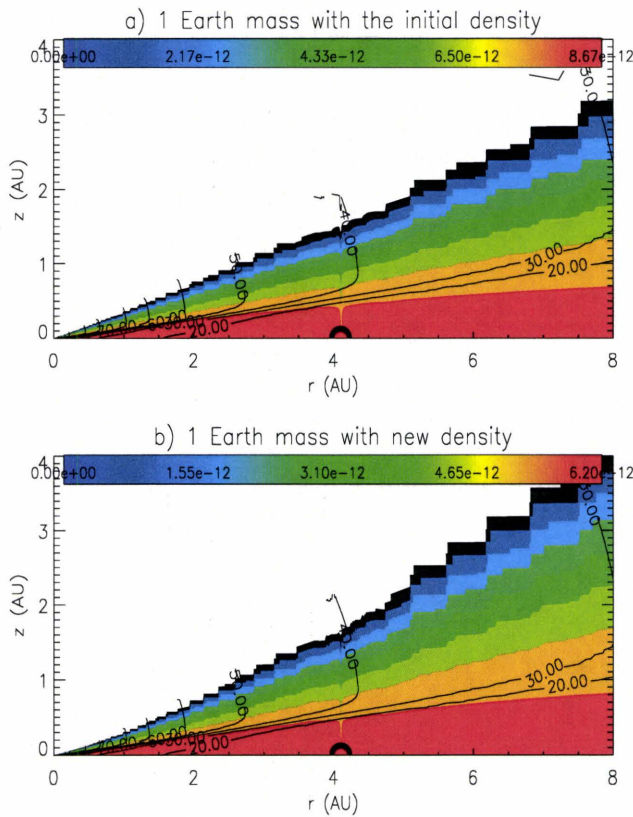


Figure 3.18: The density and temperature structure of VLMS disk with  $1M_{\oplus}$  at 4.1 AU. Fig. a) and b) is for the case of the initial density and new density structure, respectively. The color denotes the density (density scale is shown in color bar above each figure and density unit is  $g/cm^3$ ) and the contours denote the temperature. The Hill radius of this planet is plotted by thick solid line.

We also present the density and temperature structure with a  $1M_{\oplus}$  planet in Fig. 3.18. Plot a) shows the initial density and new temperature. Plot b) shows the new density and temperature. The new, higher scale height pushes the density up to higher scale heights. Thus, the difference between plot a) and b) of Fig. 3.18 arises from the usage of different scale height.

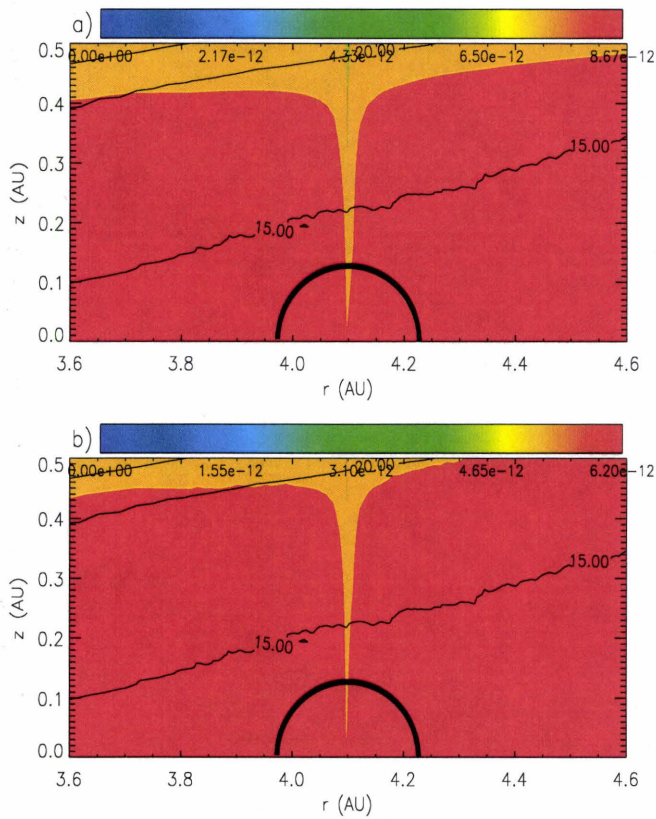


Figure 3.19: The density and temperature structure of VLMS disk with  $1M_{\oplus}$  planet at 4.1 AU. Fig. a) and b) is for the case of the initial density and new density structure, respectively. The color denotes the density (density scale is shown in color bar above each figure and density unit is  $g/cm^3$ ) and the contour denotes the temperature. The Hill radius of this planet is plotted by thick solid line.

Fig. 3.19 shows the zoomed-in version of Fig. 3.18. It shows the difference of density distribution again due to different scale heights for these two case.

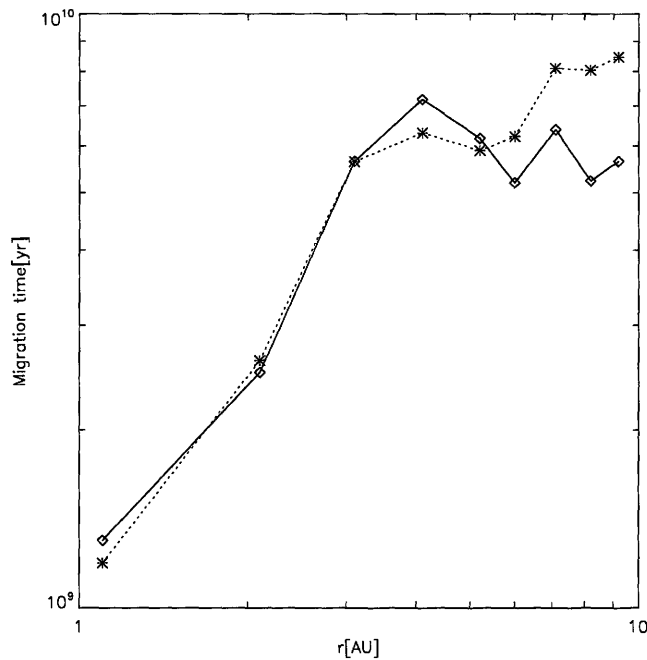


Figure 3.20: The Migration time of a  $1 M_{\oplus}$  planets in the disk around VLMS. The solid line denotes the migration time calculated by the initial density and the new temperature. The dotted line is for case of by using the new density and temperature.

Now we consider the effect on migration. Fig. 3.20 shows the migration time of a  $1 M_{\oplus}$  planet in a disk around VLMS. The solid line denotes the migration time calculated from the initial density and the new temperature. The dotted line is for case of by using the new density and temperature. For the small orbital radii ( $< 5$  AU), the difference is less than 15% and is almost negligible. On the other hand, for large orbital radii ( $> 5$  AU), the

difference becomes large. This is because the higher scale height reduces the vertical average of the torque so that the torque becomes weaker. Thus, the migration time with the new density structure is longer than the one with the initial one. Although the new scale height changes the migration time, especially for large orbital radii, the migration time for small orbital radii ( $< 5$  AU) becomes more important when we compare to the disk lifetime. Also, the large difference for large orbital radii does not affect our conclusion, which is mentioned later. Thus, in this thesis, our approach gives a reasonable calculation of the migration effects when the initial density profile is used together with the new temperature. From here, we use the initial density and new temperature structure in order to calculate the tidal torque.

## Chapter 4

# Results: The effect of the dust settling on planetary migration

We present our results on the effect of the dust settling on planetary migration in this chapter. The detailed reason is mentioned in § 2.2.3. We, especially focus on planets in disks around VLMS. Disk models and torque calculations that we use were discussed in § 3.4.2 and 3.4.3. In § 4.1, we discuss models of dust settling and disk parameters, our results are shown in § 4.2, and the discussion is in § 4.3.

### 4.1 Models of dust settling & disk parameters

Our disk parameters are listed in Table 3.5 in § 3.3.3 with the replacement of  $R_{out} = 100$  AU with 10 AU. Also, we increase  $M_d$  by a factor of ten as suggested by the literature on planet migration (e.g. Kokubo & Ida, 1998; Alibert et al., 2005).

Disk models and torque calculations that we use were discussed in § 3.4.2 and 3.4.3.

For the dust settling, we use the model of Dubrulle et al. (1995). In our setup, the friction time,  $\tau_f$  (see Eq. (2.23)) becomes, using Eq. (3.58) at  $z = 0$ ,

$$\tau_f = \frac{\sqrt{2\pi\rho_s a}}{\Omega_{Kep}\Sigma}. \quad (4.1)$$

Thus, the scale height of the dust is expressed as Eq. (2.25) with

$$\bar{H} = \left(\frac{1}{1+\gamma}\right)^{1/4} \sqrt{\frac{\alpha\Sigma}{\sqrt{2\pi\rho_s a}}}. \quad (4.2)$$

We set  $\gamma = 3$ ,  $\alpha = 0.01$ , and  $\rho_s = 3.9[g/cm^3]$ .

## 4.2 Results

We calculated the density and temperature in a disk around a VLMS with a planet. Fig. 4.1, 4.2, 4.3, and 4.4 a) and b) show the results for 0.1, 1, 5, and  $10M_\oplus$  planets in disks without and with dust settling, respectively. One of the basic features of these plots is that the temperature of the upper layer is higher than that of the lower one. The transition region is defined by the collection of contours of various temperatures. The upper layer corresponds to the superheated layer of CG97. In other words, our numerical calculation are consistent with analytical ones of CG97.

The other common feature of our calculations is the temperature behavior as the dust settles. The density of the mid-plane increases. This, in turn, changes the optical depth in the mid-plane which becomes higher. At the same time, the density in the upper layer decreases because of dust settling. This causes the optical depth in the upper layer to decrease. Thus, photons emitted from the central star find it easier to penetrate the upper layer, and harder through the mid-plane as dust settles. Thus, the temperature in the

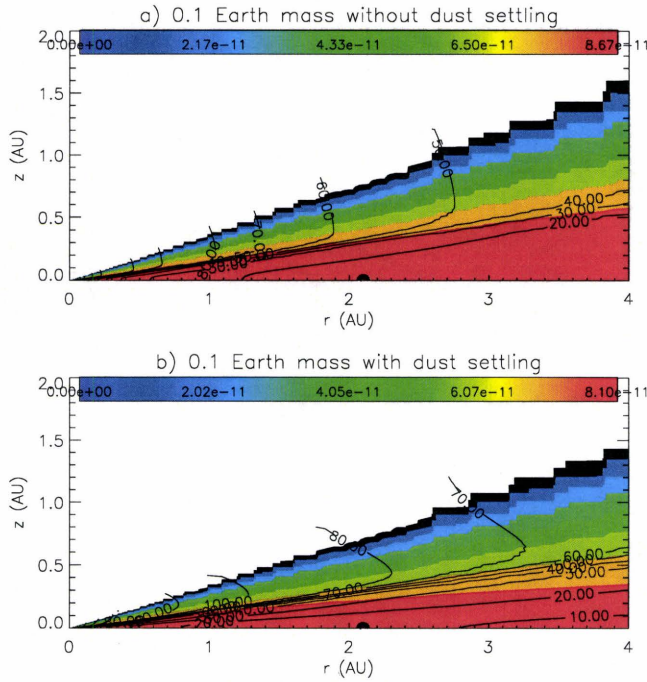


Figure 4.1: The density and temperature structure of VLMS disk with  $0.1 M_{\oplus}$  at 2.1 AU. Fig. a) and b) without and with dust settling, respectively. The color denotes the density (density scale is shown in color bar above each figure and density unit is  $g/cm^3$ ) and the contours are for temperature in Kelvin. The redder the color, the higher is the density. The thick solid line denotes the Hill radius of the planet.

mid-plane in the presence of dust settling, is lower than that without dust settling. For the upper layer, the situation is the opposite.

Our models also include the effect of the gravitational force of the planet (following JS05). The planetary field reduces the density above the planet, as reviewed in § 2.2.3 (also see Eq. (3.60)).

In order to examine this, we show the results of disks around the planet of  $0.1, 1, 5,$  and  $10 M_{\oplus}$  in disks without and with dust settling in Fig. 4.5, 4.6,

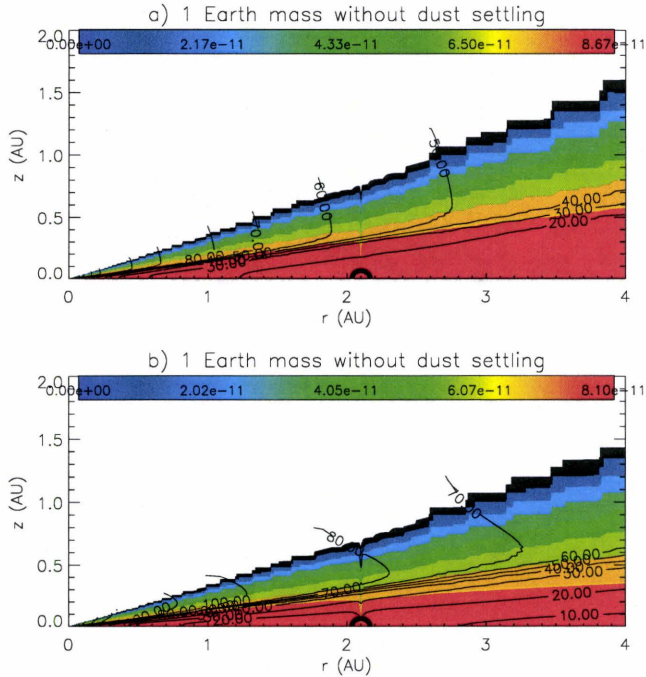


Figure 4.2: The density and temperature structure of VLMS disk with  $1M_{\oplus}$  at 2.1 AU. Fig. a) and b) is without and with dust settling, respectively. The definition of lines and colors is the same as Fig. 4.1

4.7, and 4.8 a) and b), respectively. One of the most important results of this work is that the effect of dust settling is enhanced with the increase of the planetary mass, as shown in plots a) of these figures. In particular, we see that the  $0.1 - 1M_{\oplus}$  planets have virtually no effect on disk structure. However the temperature and density behavior are very strongly affected in the  $5 - 10M_{\oplus}$  cases. In these figures we see the effect of the resultant shadowing (in front of the planet) and illumination (behind the planet) as the planetary mass increases. This effect is very small compared with JS04 since they considered CTTS systems. We combine both of these effects in our calculation. Plots b)

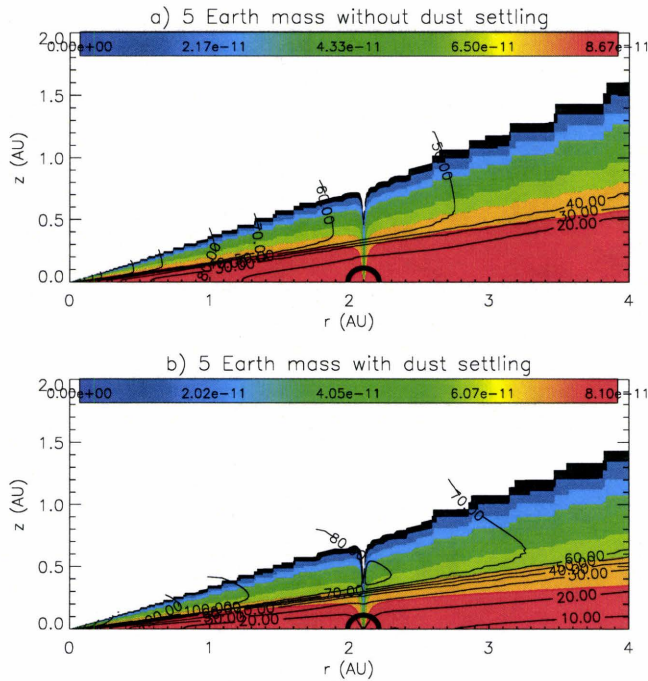


Figure 4.3: The density and temperature structure of VLMS disk with  $5M_{\oplus}$  at 2.1 AU. Fig. a) and b) is without and with dust settling, respectively. The definition of lines and colors is the same as Fig. 4.1

of these figures shows this combined effect. Comparing plots b) with a), the dust settling enhances the effect of gravity in the disk's temperature behavior. This is because dust settling also moves dust towards the mid-plane. Both of these effects affect the resonant conditions so that the resulting Lindblad torque is either stronger or weaker.

In order to quantitatively investigate the density and temperature behavior for each planetary mass, we plot them in Fig 4.9, 4.10, 4.11, and 4.12. For each panel, the solid line represents a quantity without dust settling, and the dotted line is for the case of dust settling. For the density and temperature

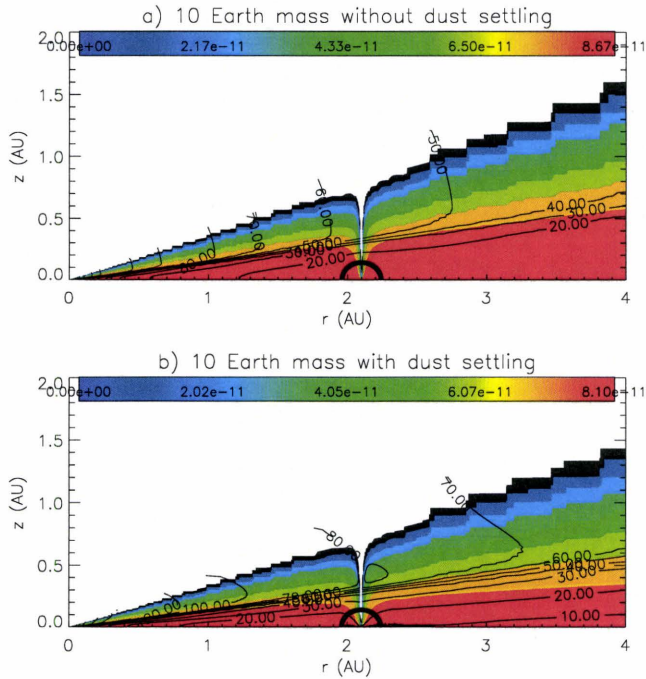


Figure 4.4: The density and temperature structure of VLMS disk with  $10M_{\oplus}$  at 2.1 AU. Fig. a) and b) is without and with dust settling, respectively. The definition of lines and colors is the same as Fig. 4.1

panels, the thin black line denotes these quantities at  $r_p - r_H$ , and the thick red line is for these quantities at  $r_p + r_H$ , where  $r_p$  and  $r_H$  is the planetary and Hill radius, respectively. At these positions, the Lindblad torque takes its maximum or minimum value. For every plot of the density, the basic behavior is the same. The density difference at the two positions, however, increases as the planetary mass increases. This is because the density in the vicinity of the planet is determined by the gravitational force of the planet, as shown in Fig 4.5 to 4.8. The density at  $r_p - r_H$  is always higher than that at  $r_p + r_H$

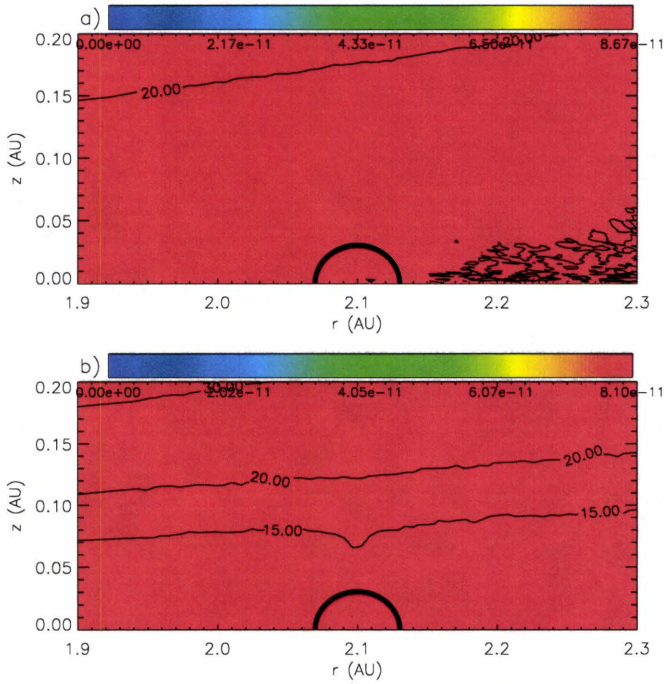


Figure 4.5: The density and temperature structure of VLMS disk with  $0.1 M_{\oplus}$  at 2.1 AU. Fig. a) and b) is without and with dust settling, respectively. The color denotes the density (density scale is shown in color bar above each figure and density unit is  $g/cm^3$ ) and the contours are for the temperature in Kelvin: the redder the color, the higher is the density. The thick solid line denotes the Hill radius of the planet.

because the surface density is a decreasing function of radius. They also show that the material is accumulated at the mid-plane as dust settles.

For the temperature behavior, the common trend is that the temperature in the mid-plane with dust settling is lower than that without dust settling, and for the upper layer the situation is the opposite, as mentioned above. There are two important features of the results that scale with increasing planetary mass. As the mass of the planet is increased, the temperature difference is

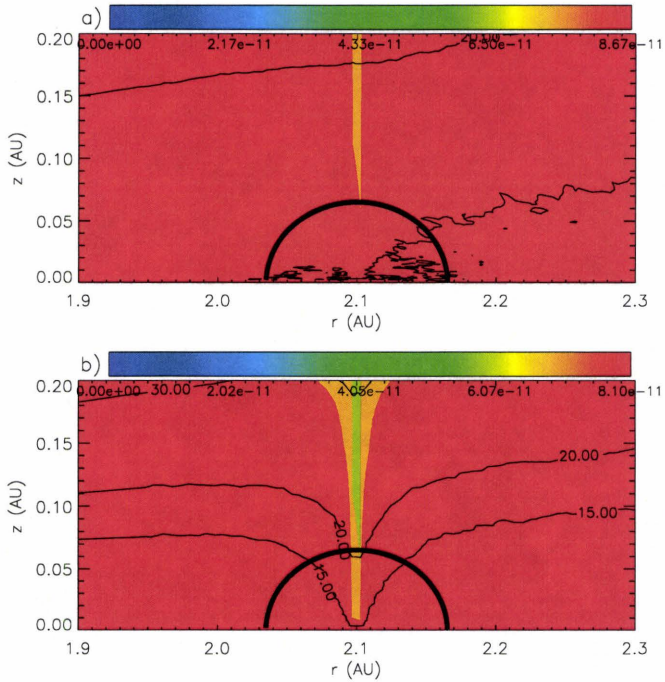


Figure 4.6: The density and temperature structure of VLMS disk with  $1M_{\oplus}$  at 2.1 AU. Fig. a) and b) is without and with dust settling, respectively. The definition of lines and colors is the same as Fig. 4.5

increased. This arises from the density difference mentioned above. The other is that the temperature itself decreases with planetary mass. This arises from the gravity of the planet. The more massive the planet is, the more material is accumulated in the mid-plane. In other words, the addition of the effect of planetary gravity into the condition for hydrostatic equilibrium mimics the effects of dust settling.

We can, at last, calculate the normalized torque and total torque. The top and second panel of Fig 4.9, 4.10, 4.11, and 4.12 show the normalized torque and torque, respectively. Again, the solid line represents these quantities with-

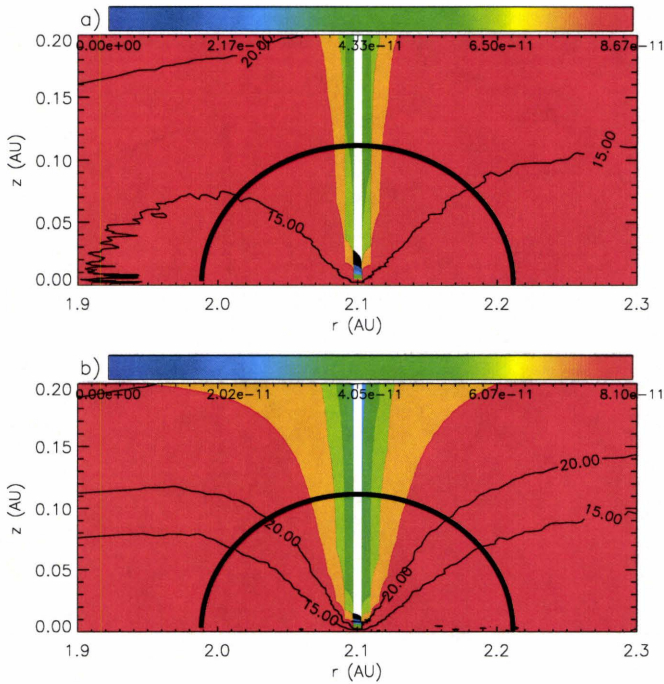


Figure 4.7: The density and temperature structure of VLMS disk with  $5M_{\oplus}$  at 2.1 AU. Fig. a) and b) is without and with dust settling, respectively. The definition of lines and colors is the same as Fig. 4.5

out dust settling, and the dotted line is for the case of dust settling. Note that it's very hard to disentangle the effect of the density and temperature on the torque even if the normalized torque is considered, because the temperature in our calculation is mass-weighted and different grains with different scale height have different temperatures. Also shown in the temperature plots in each of these figures, the vertical dashed line indicates the position of new disk scale height in the case of no dust settling. These lie between 0.07 and 0.08 AU.

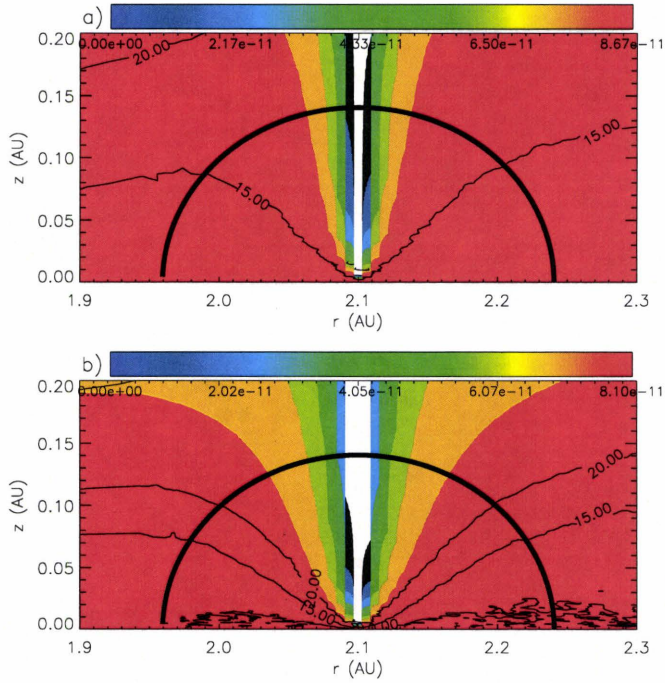


Figure 4.8: The density and temperature structure of VLMS disk with  $10M_{\oplus}$  at 2.1 AU. Fig. a) and b) is without and with dust settling, respectively. The definition of lines and colors is the same as Fig. 4.5

The panel showing the normalized torque indicates that the difference between them with and without dust settling is reduced with the planetary mass. This is because as the planetary mass increases, the temperature itself becomes lower. Since the torque is proportional to the inverse of the temperature, this results in increasing the normalized torque. Thus, the normalized torque tells us that the difference between dust settling and not is minimized for more massive planets. In other words, the addition of the gravity of the planet causes similar effect to that of dust settling.

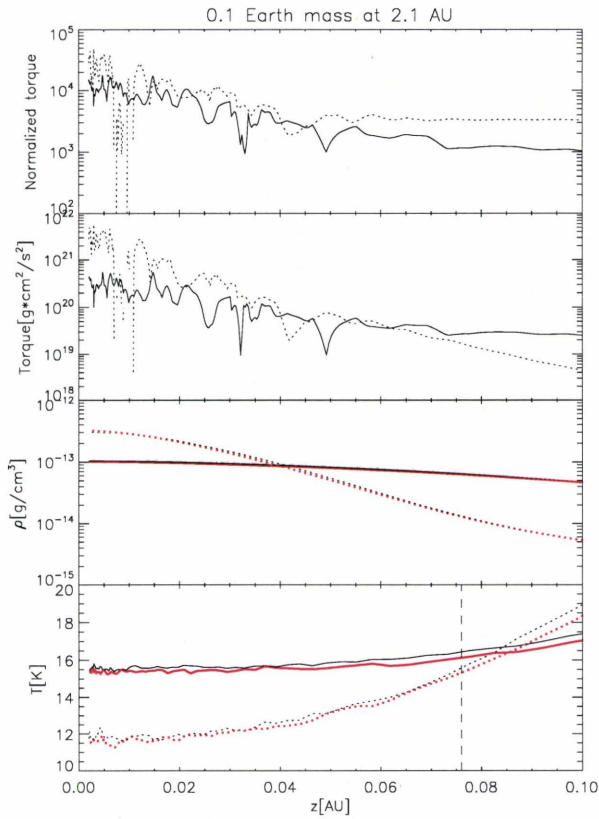


Figure 4.9: The vertical structure of normalized torque, torque, density, and temperature of VLMS disk with  $0.1M_{\oplus}$  at 2.1 AU. For every panel, the solid line denotes quantity without dust settling, and the dotted line is for dust settling. For the density and temperature panels, the thin black line denotes these quantities at  $r_p - r_H$ , and the thick red line is for these quantities at  $r_p + r_H$ , where  $r_p$  and  $r_H$  is the planetary and Hill radius, respectively. The vertical dashed line denotes the new scale height in the case of no dust settling.

Planetary migration is determined once the torque is known. It is shown in the second panel of each figure. The behavior of the torque is determined by the combination of density and temperature effects shown in the bottom panels. Since the torque is approximately proportional to the density and

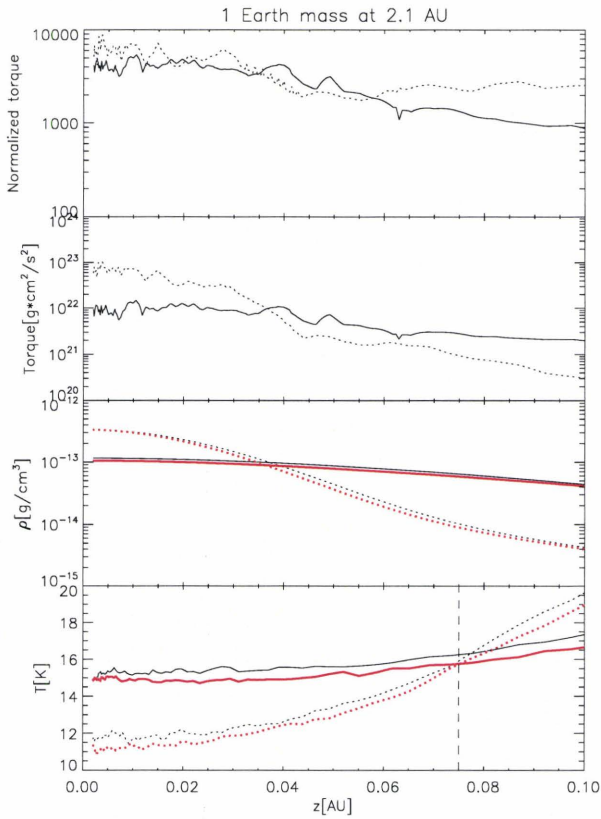


Figure 4.10: The vertical structure of normalized torque, torque, density, and temperature of VLMS disk with  $1M_{\oplus}$  at 2.1 AU. The definition of each line is the same as Fig. 4.9.

varies as the inverse of the temperature, the torque without dust settling for the upper layer of the disk is stronger than that with dust settling. For the inner layer, the situation is the opposite. Thus, even if there is no difference of the normalized torque with and without dust settling, the difference of the torque becomes non-zero. These tidal torques cause planets to migrate inward for both cases (since the torque exerted on the disk by the planet is always

positive). Also the torque at the mid-plane takes the maximum value since the density is highest and the temperature is the lowest.

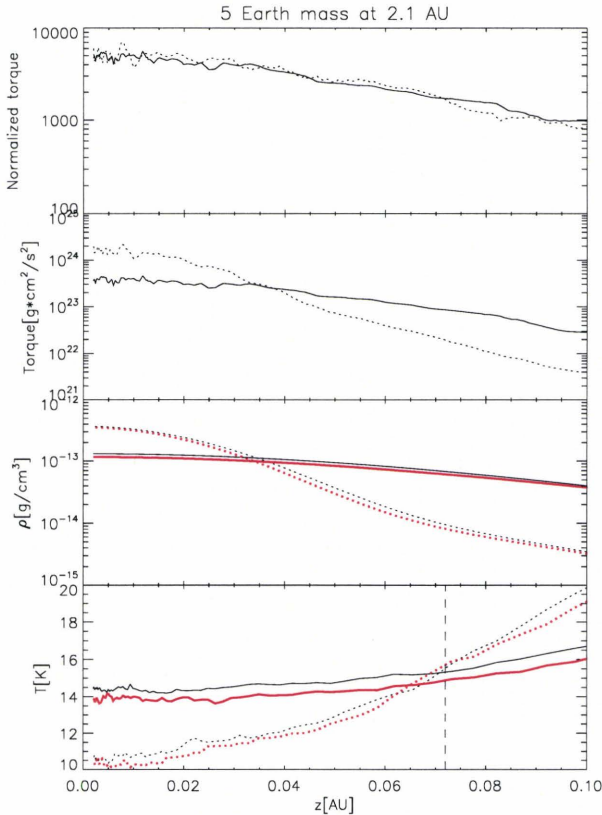


Figure 4.11: The vertical structure of normalized torque, torque, density, and temperature of VLMS disk with  $5M_{\oplus}$  at 2.1 AU. The definition of each line is the same as Fig. 4.9.

Note that the normalized torque and torque for a very low mass planet near the mid-plane is quite spiky because the density perturbation due to the planet is very small. Although one suspects that this spiky shape could cause some numerical error, we undertook a convergence study and showed that

our resolution is clearly sufficient. Also D'Angelo et al. (2002) found similar behavior for the torque. They used a nested grid technique, which allowed them to resolve the region of the vicinity in the planet very well. Their grid also guarantees that torque calculations are convergent.

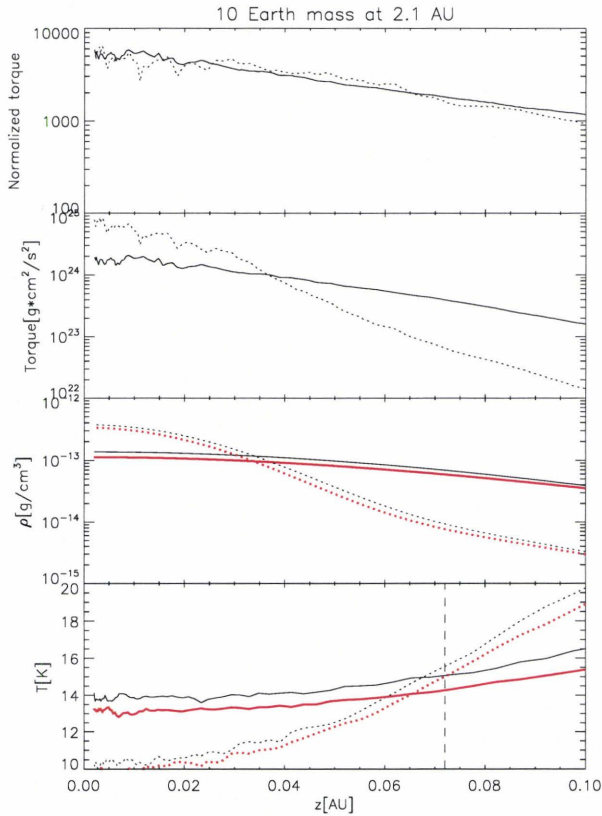


Figure 4.12: The vertical structure of normalized torque, torque, density, and temperature of VLMS disk with  $10M_{\oplus}$  at 2.1 AU. The definition of each line is the same as Fig. 4.9.

We have finally reached the basic point of the entire thesis. The migration time as a function of orbital radius is shown in Fig. 4.13. The thin black lines

represent the case without dust settling. The thick red lines are for the case of dust settling. The solid line represents  $0.1M_{\oplus}$  mass of the planet, the dotted line is for  $1M_{\oplus}$ , the dashed line is for  $5M_{\oplus}$ , the dot-dashed line is for  $10M_{\oplus}$ . Our main result is that the migration time is reduced with dust settling. This is because the torque at the mid-plane in the case of dust settling is larger than that without dust settling, as shown in Fig. 4.9 to 4.12. For lower mass planets ( $0.1 - 1M_{\oplus}$ ), migration does not cause any problem since the migration time is longer than disk lifetime, which is about  $10^{7-8}$  years. On the other hand, for massive planets ( $5 - 10M_{\oplus}$ ), the shorter migration times more strongly affect the fate of the planets, although the migration time is still comparable to the disk lifetime. Our calculations show that relatively massive planets in VLMS disks can migrate inward, but all planets are saved from plunging into their host stars because their migration times are comparable to the disk lifetimes. This finding is consistent with the existence of a super Earth ( $\sim 5.5M_{\oplus}$ ) at 2.6 AU around M dwarf discovered by Beaulieu et al. (2006). Thus we can conclude that the low mass planetary system in VLMS survives migration without the need for safe guards such as dead zones. However, the migration timescale for CTTS disks is two orders of magnitude shorter than the disk lifetime (e.g. TTW02).

Fig 4.14 shows the migration time as a function of planetary mass. The thin black lines represent the case without dust settling. The thick red lines are for the case with dust settling. The solid line represents planets at 2 AU, and the dotted line is for 5 AU. As mentioned above, the difference between the two cases becomes smaller as the planetary mass is increased. We summarize the ratio of the migration time at 5 AU between the two cases in Table 4.1.

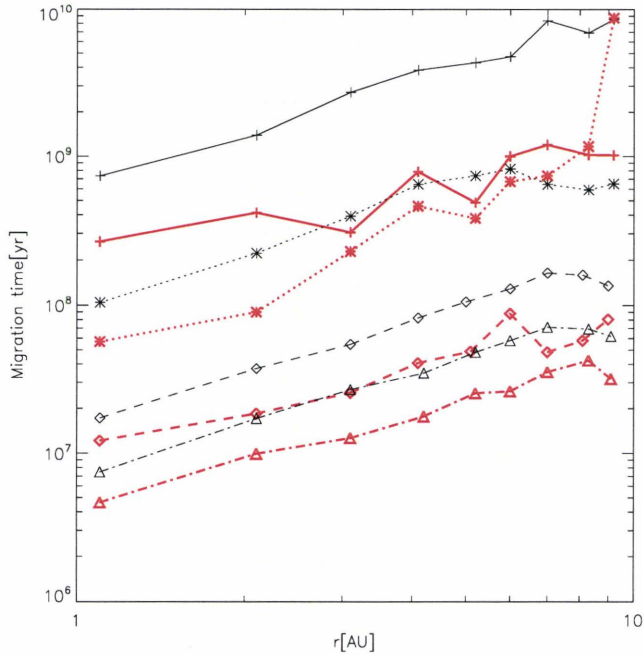


Figure 4.13: The migration time as a function of the planetary position. The thin black lines denote the case without dust settling. The thick red lines are for the case of dust settling. The solid line denotes  $0.1M_{\oplus}$  mass of the planet, the dotted line is for  $1M_{\oplus}$ , the dashed line is for  $5M_{\oplus}$ , the dot-dashed line is for  $10M_{\oplus}$ .

For more massive planets than  $1M_{\oplus}$ , the migration time with dust settling is reduced by a factor of two. Dust settling is inescapable when planets form. For lower mass planets, the ratio of the migration time without dust settling to the case of dust settling is larger. This is because the lower gravity of planets does not wash out the effect of dust settling. This radial mobility may help to form the core of planets efficiently.

Table 4.1: Summary of the ratio of migration time between with and without dust settling

$M_p[M_\oplus]$	0.1	1	5	10
ratio <sup>1</sup>	8.8	1.9	2.1	1.9

<sup>1</sup> ratio = the migration time without dust settling / the migration time with dust settling

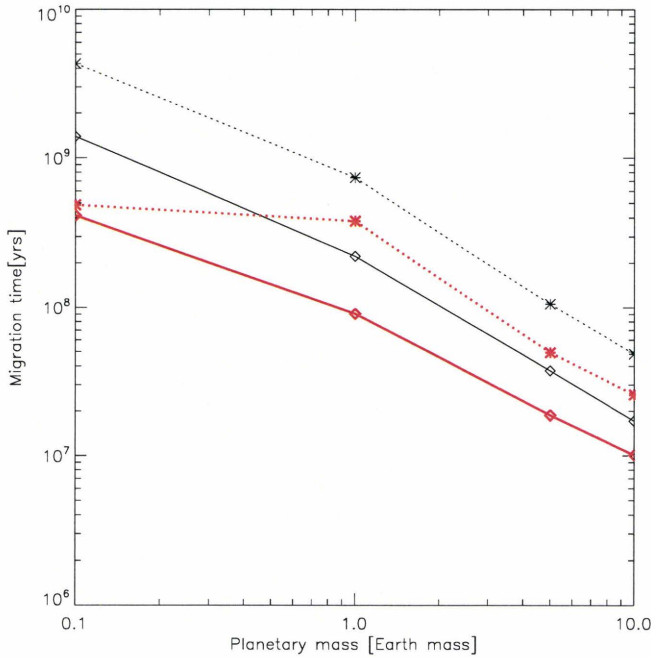


Figure 4.14: The migration time as a function of the planetary mass. The thin black lines denote the case without dust settling. The thick red lines are for the case of dust settling. The solid line denotes planets at 2 AU, and the dotted line is for 5 AU.

### 4.3 Discussion

In our calculations, we have neglected viscous heating of the disk. This effect is known to dominate disk heating, as compared with radiation heating,

within 2 AU. Although we assume disks to be passive (following CG97), this effect seems to cause very interesting effects on the migration. If we include viscous heating into our calculations, the temperature difference between the two cases (dust settling or not) would be smaller inside 2 AU since the mid-plane is heated up by the viscous heating. This implies that the torque with dust settling becomes smaller inside 2 AU although we think the torque with dust settling in the mid-plane is still larger than that without dust settling because the density effect is not affected by the viscous heating. In other words, the viscous heating plays a role in slowing down the migration. Thus, our results are qualitatively the same with viscous heating, although the migration time becomes slightly longer.

Another important feature of disks are dead zones (DZs). In DZs, the ionization rate is small, which results in the decoupling of gas from the magnetic field. MRI turbulence is therefore very weak there. This causes viscous heating to be negligible in the DZs. Moreover, dust settling becomes stronger in a DZ (See Eq. (4.2)). This results in faster migration times. Thus, we can say that our calculations also pertain to planets in DZs. DZs probably play a role in speeding up the migration from this point of view.

Since DZs are determined by the ionization of the gas, their sizes are dependent on stellar and disk parameters. If planets migrate from outside of DZs in disks with dust settling, they can be stopped, as shown by Matsumura et al. (2007). This logic is still valid for disks with dust settling.

In addition to the effect of disks mentioned so far, the accretion of gas onto the planets also causes an interesting effect on migration. As planets accrete the surrounding gas and dust, they are heated up. The radiation of

this energy into the surrounding disk causes its temperature to be increased. If the temperature is increased by this accretion process of the planets, the migration is slowed down since this effect is similar to viscous heating. If planets are in DZs, the migration speed is determined by the balance between the effect of DZs and the accretion heating. Moreover, this accretion heating may play a role in shrinking DZs since the radiation by the planets causes gas to be ionized. If planets migrate from outside of DZs, the stopping effects of DZs are weakened. This is partly because the accretion heating increases the temperature in the DZs, and partly because this heating may enable the DZs to be better ionized.

## Chapter 5

### Conclusions

Planet formation and migration are strongly coupled to disk evolution. Although planetary migration was proposed to explain Hot Jupiters, the rapid loss of such planets is one of the biggest problems for the theory. We investigated this problem by focusing on radiatively heated disks. This is because the Lindblad torque, the driving force of the migration, is very sensitive to the temperature structure of disks. More specifically, the resonant positions are controlled by gas pressure, the so-called torque cut-off. Furthermore, dust, which is the dominant absorber of the stellar radiation, settles into the mid-plane because of the grain growth. Obviously, this causes the density structure of dust to be modified drastically, resulting in a change of the resonant positions.

We addressed this problem by using a versatile 2D radiative transfer code, called RADMC, for the calculation of the temperature and density. This code uses the Monte Carlo method and the paths of photon are usually followed in spherical coordinates. For the torque calculations, we adapted the analytical formula derived to a cylindrical coordinate system. In order to calculate the torque accurately, we transformed RADMC algorithms from spherical to cylindrical coordinates. Although the original RADMC is a highly tested, reliable

code, this modification required us to test it again. In chapter 3, we presented the results of our intensive tests. Our methods proved to be highly accurate and converged well.

In order to calculate the density and temperature of disks which are irradiated by the stellar radiation, the composition and size distribution of dust is required. For the dust composition, we used the model of Pollack et al. (1994), and for the size distribution, we used the so-called MRN distribution (Mathis et al., 1977). Dust settling results in the situation that different grain sizes of dust have different scale heights. This raises a difficulty in calculating the density distribution. Therefore, we used the discretized MRN distribution. In chapter 3, we conducted a convergence study for this.

As reviewed in chapter 2, the torque calculation is very sensitive to the density and temperature in the vicinity of the planet. This required us to conduct an intensive convergence study about the grid system we used. We demonstrated convergence by various considerations, as discussed in chapter 3.

Finally, we calculated the torque and migration time, especially for disks around VLMS such as M dwarfs. In order to estimate the migration time more accurately, we treated the density and temperature by taking into account the gravity of the planet (JS03 and JS04). The gravitational force of the planet compresses the density around the planet, producing in a high density region around the planet and resultant shadowing (in front of the planet) and illumination (behind the planet) regions. Furthermore, disk evolution with time is considered. We found that dust settling decreases the migration time by a factor of two for relatively massive planets ( $> 5M_{\oplus}$ ). For lower mass

planets, the migration time is reduced by a factor of eight. This is because both the dust settling and the planetary gravity cause the density around the planet to be increased, thereby decreasing the temperature around the planet. Since the tidal torque is proportional to the density and varies inversely with the temperature, the migration time is decreased. As the planetary mass is increased, the effect of dust settling is washed out. Therefore, the more massive a planet is, the shorter the migration time is.

The migration timescale we found for VLMS is longer than or comparable to the disk life time. This is independent of dust settling. This enables us to conclude that the time mismatch found for CTTS does not arise for VLMS, and is consistent with the discovery of the super Earth by Beaulieu et al. (2006). This suggests that planets found in VLMS systems may still lie near their region of formation - a point that may have considerable observational consequences. The problem of rapid migration in CTTS systems must evidently be solved some special mechanism -such as DZs or the tidal interaction between stars and very close planets.

Future work on this question will focus on fully dynamical treatments of radiatively heated and evolving disks with planets.

## Bibliography

- Adams, F., Lada, C., & Shu, F. 1987, *ApJ*, 312, 788
- Alibert, Y., Mordasini, C., Benz, W., & Winisdoerffer, C. 2005, *A&A*, 434, 343
- Artymowicz, P. 1993a, *ApJ*, 419, 166
- . 1993b, *ApJ*, 419, 155
- Auer, L., & Mihalas, D. 1969, *ApJ*, 158, 641
- Balbus, S., & Hawley, J. 1991a, *ApJ*, 376, 214
- . 1991b, *ApJ*, 376, 223
- Bate, M., Lubow, S., Ogilvie, G., & Miller, K. 2003, *MNRAS*, 341, 213
- Beaulieu, J., Bennett, D., Fouqué, P., Williams, A., Dominik, M., Jørgensen, U., Kubas, D., Cassan, A., Coutures, C., Greenhill, J., Hill, K., Menzies, J., Sackett, P., Albrow, M., Brilliant, S., Caldwell, J., Calitz, J., Cook, K., Corrales, E., Desort, M., Dieters, S., Dominis, D., Donatowicz, J., Hoffman, M., Kane, S., Marquette, J., Martin, R., Meintjes, P., Pollard, K., Sahu, K., Vinter, C., Wambsganss, J., Woller, K., Horne, K., Steele, I., Bramich, D., Burgdorf, M., Snodgrass, C., Bode, M., Udalski, A., and M Kubiak, M. S., Wieckowski, T., Pietrzyński, G., Soszyński, I., Szewczyk, O., Wyrzykowski, L., Paczyński, B., Abe, F., Bond, I., Britton, T., Gilmore, A., Hearnshaw, J., Itow, Y., Kamiya, K., Kilmartin, P., Korpela, A., Masuda, K., Mstsubara, Y., Motomura, M., Muraki, Y., Nakakura, S., Okada, C., Ohnishi, K., Rattenbury, N., Sako, T., Sato, S., Sasaki, M., Sekiguchi, T., Sullivan, D., Tristram, P., York, P., & Yoshida, T. 2006, *Nature*, 439, 437
- Bennett, D., Bond, I., Udalski, A., Sumi, T., Fukui, A., Furusawa, K., Hearnshaw, J., Holderness, S., Itow, Y., Kamiya, K., Korpela, A., Kilmartin, P., Lin, W., Ling, C., Matsubara, K. M. Y., Miyake, N., Muraki, Y., Nagaya, M., Okumura, T., Ohnishi, K., Perrott, Y., Rattenbury, N., Sako, T., Saito, T., Sato, S., Skuijan, L., Sullivan, D., Sweatman, W., Tristram, P., Yock, P., Kubiak, M., Szymanski, M., Pietrzynski, G., Soszynski, I., Szewczyk, O., Wyrzykowski, L., Ulaczyk, K., Batista, V., Beaulieu, J., Brilliant, S., Cassean, A., Fouque, P., Kervella, P., Kubas, D., & Marquette, J. 2008, preprint (astro-ph/arXiv:0806.0025v1)
- Bjorkman, J., & Wood, K. 2001, *ApJ*, 554, 615
- Bonfils, X., Mayor, M., Delfosse, X., Forveille, T., Gillon, M., Perrier, C., Udry, S., Bouchy, F., Lovis, C., Pepe, F., Queloz, D., Santos, N., & Bertaux, J. 2007, *A&A*, 474, 293

- Chiang, E., & Goldreich, P. 1997, *ApJ*, 490, 368  
— 1999, *ApJ*, 519, 279
- Chiang, E., Joungh, M., Creech-Eakman, M., Qi, C., Kessler, J., Blake, G., & van Dishoeck, E. 2001, *ApJ*, 547, 1077
- D'Alessio, P., Calvet, N., & Hartmann, L. 2001, *ApJ*, 553, 321
- D'Alessio, P., Calvet, N., Hartmann, L., Franco-Hern'andez, R., & Ser' in, H. 2006, *ApJ*, 638, 314
- D'Alessio, P., Calvet, N., Hartmann, L., Lizano, S., & Cantó, J. 1999, *ApJ*, 527, 893
- D'Alessio, P., Cantó, J., Calvet, N., & Lizano, S. 1998, *ApJ*, 500, 411
- D'Angelo, G., Henning, T., & Kley, W. 2002, *A&A*, 385, 647
- D'Angelo, G., Kley, W., & Henning, T. 2003, *ApJ*, 586, 540
- Demory, B., Gillon, M., Barman, T., Bonfils, X., Mayor, M., Mazeh, T., Queloz, D., Udry, S., Bouchy, F., Delfosse, X., Forveille, T., Pepe, F. M. F., & Perrier, C. 2007, *A&A*, 475, 1125
- Di Stefano, R., & Night, C. 2008, preprint (astro-ph/arXiv:0801.1510v1)
- Draine, B., & Lee, H. 1984, *ApJ*, 285, 89
- Draine, B., & Li, A. 2007, *ApJ*, 657, 810
- Dubrulle, B., Morfill, G., & Sterzik, M. 1995, *Icarus*, 114, 237
- Dullemond, C., & Dominik, C. 2004a, *A&A*, 421, 1075  
— 2004b, *A&A*, 417, 159
- Dullemond, C., & Turolla, R. 2000, *A&A*, 360, 1187
- Dullemond, C., van Zadelhoff, G., & Natta, A. 2002, *A&A*, 389, 464
- Dullemond, C. P., Hollenbach, D., Kamp, I., & D'Alessio, P. 2007, *Protostars and Planets V*, 555
- Endl, M., Cochran, W., Wittenmyer, R., & Boss, A. 2008, *ApJ*, 673, 1165
- Fortney, J. 2008, preprint (astro-ph/arXiv:0801.4943v1)
- Fromang, S., & Papaloizou, J. 2006, *A&A*, 452, 751
- Fromang, S., Terquem, C., & Nelson, R. 2005, *MNRAS*, 363, 943
- Gammie, C. 1996, *ApJ*, 457, 355

- Goldreich, P., & Tremaine, S. 1979, *ApJ*, 233, 857  
— 1980, *ApJ*, 241, 425
- Hubeny, I., & Lanz, T. 1992, *A&A*, 262, 501
- Jang-Condell, H., & Sasselov, D. 2003, *ApJ*, 593, 1116  
— 2004, *ApJ*, 608, 497  
— 2005, *ApJ*, 619, 1123
- Kenyon, S., & Hartmann, L. 1987, *ApJ*, 323, 714
- Klahr, H., & Kley, W. 2006, *A&A*, 445, 747
- Kley, W., D'Angelo, G., & Henning, T. 2001, *ApJ*, 547, 457
- Kokubo, E., & Ida, S. 1998, *Icarus*, 131, 171
- Korycansky, D., & Pollack, J. 1993, *Icarus*, 102, 150
- Li, A., & Draine, B. 2001, *ApJ*, 554, 778
- Liu, L., Zhang, L., & Tan, H. 2006, *JQSRT*, 97, 446
- Lopez, B., Mékarnia, D., & Lefèvre, J. 1995, *A&A*, 296, 752
- Lubow, S., & Ogilvie, G. 1998, *ApJ*, 504, 983
- Lucy, L. 1999, *A&A*, 345, 211
- Lynden-Bell, D., & Pringle, J. 1974, *MNRAS*, 168, 603
- Masset, F. 2001, *ApJ*, 5558, 453  
— 2002, *A&A*, 387, 605
- Masset, F., & Papaloizou, J. 2003, *ApJ*, 588, 494
- Mathis, J., Rumpl, W., & Nordsieck, K. 1977, *ApJ*, 217, 425
- Matsumura, S., Pudritz, R., & Thommes, E. 2007, *ApJ*, 660, 1609
- Mayor, M., & Queloz, D. 1995, *Nature*, 378, 355
- Melo, C., Santos, N., Gieren, W., Pietrzynski, G., Ruiz, M., Sousa, S., Bouchy, F., Lovis, C., Mayor, M., Pepe, F., Queloz, D., da Silva, R., & Udry, S. 2007, *A&A*, 467, 721
- Menou, K., & Goodman, J. 2004, *ApJ*, 606, 520
- Miyoshi, K., Takeuchi, T., Tanaka, H., & Ida, S. 1999, *ApJ*, 516, 451
- Muto, T., Machida, M., & Inutsuka, S. 2008, *ApJ*, 679, 813

- Nelson, R., & Papaloizou, J. 2003, MNRAS, 339, 993  
— 2004, MNRAS, 350, 849
- Nelson, R., Papaloizou, J., Masset, F., & Kley, W. 2000, MNRAS, 318, 18
- Niccolini, G., & Alcolea, J. 2006, A&A, 456, 1
- Oishi, J., Mac Low, M., & Menou, K. 2007, ApJ, 670, 805
- Paardekooper, S., & Mellema, G. 2006, A&A, 459, L17
- Pascucci, I., Wolf, S., Steinacker, J., Henning, C. D. T., Niccolini, G., Woitke, P., & Lopez, B. 2004, A&A, 417, 793
- Pollack, J., Hollenbach, D., Beckwith, S., Simonelli, D., Roush, T., & Fong, W. 1994, ApJ, 421, 615
- Rivera, E., Lissauer, J., Butler, P., Marcy, G., Vogt, S., Fischer, D., Brown, T., Laughlin, G., & Gregory W Henry. 2005, ApJ, 634, 625
- Scholz, A., Jayawardhana, R., Wood, K., Meeus, G., Stelzer, B., Walker, C., & O'Sullivan, M. 2007, ApJ, 660, 1517
- Schräpler, R., & Henning, T. 2004, ApJ, 614, 960
- Shakura, N., & Sunyaev, R. 1973, A&A, 24, 337
- Steinacker, J., Henning, T., Bacmann, A., & Semenov, D. 2003, A&A, 401, 405
- Steinacker, J., Thamm, E., & Maier, U. 1996, JQSRT, 56, 97
- Stone, J., Mihalas, D., & Norman, M. 1992, ApJS, 80, 819
- Tanaka, H., Takeuchi, T., & Ward, W. 2002, ApJ, 565, 1257
- Terquem, C. 2003, MNRAS, 341, 1157
- Udry, S., Bonfils, X., Delfosse, X., Forveille, T., Mayor, M., Perrier, C., Bouchy, F., Lovis, C., Pepe, F., Queloz, D., & Bertaux, J. 2007a, A&A, 469, L43
- Udry, S., Fischer, D., & Queloz, D. 2007b, Protostars and Planets V, 685
- Van Noort, M., Hubeny, I., & Lanz, T. 2002, ApJ, 568, 1066
- Ward, W. 1988, Icarus, 73, 330  
— 1991, in Luner and Planetary Institute Conference Abstract, 1463  
— 1997, Icarus, 126, 261
- Weidenschilling, S. 1977, MNRAS, 180, 57

Whitney, B., & Hartmann, L. 1992, *ApJ*, 395, 529

Wolf, S., Fischer, O., & Pfau, W. 1998, *A&A*, 340, 103

Wood, K., Lada, C., Bjorkman, J., Kenyon, S., Whitney, B., & Wolff, M. 2002, *ApJ*, 567, 1183

